INTERACTION OF EXCITONS IN TWO-DIMENSIONAL POTENTIALS

by

Zoltán Vörös

B.S., Loránd Eötvös University, 2002

M.S., University of Pittsburgh, 2004

Submitted to the Graduate Faculty of

the Department of Physics and Astronomy in partial fulfillment

of the requirements for the degree of

Doctor of Philosophy

University of Pittsburgh

2008

UNIVERSITY OF PITTSBURGH

DEPARTMENT OF PHYSICS AND ASTRONOMY

This dissertation was presented

by

Zoltán Vörös

It was defended on

June 6th 2008

and approved by

David Snoke, Associate Professor, Dept. of Physics and Astronomy

Robert Devaty, Associate Professor, Dept. of Physics and Astronomy

Jeremy Levy, Associate Professor, Dept. of Physics and Astronomy

Vincent Liu, Associate Professor, Dept. of Physics and Astronomy

David Waldeck, Professor, Dept. of Chemistry

Dissertation Director: David Snoke, Associate Professor, Dept. of Physics and Astronomy

INTERACTION OF EXCITONS IN TWO-DIMENSIONAL POTENTIALS

Zoltán Vörös, PhD

University of Pittsburgh, 2008

In the present thesis we discuss experimental work related to the Bose-Einstein condensation (BEC) of bound electron-hole pairs (excitons) in GaAs coupled quantum wells. Coupled quantum wells were chosen because in these structures the lifetime of excitons can be extended to the μs range. In the experiments, by measuring their diffusion, we have proved that excitons can move freely in two dimensions, and we have proved that they can reach thermal equilibrium during their lifetime in a confining stress potential in the plane of the quantum wells. Having an equilibrium ensemble of these quasi-particles enabled us to measure their interaction potential in a controlled environment. We also introduce a simple theoretical model that accounts for the experimental findings on interaction. In the final chapter we discuss a new phenomenon at high stress, and evaluate its possible relation to excitonic BEC.

Keywords: quantum well exciton, exciton mobility, excitonic BEC, exciton trapping.

TABLE OF CONTENTS

LIST OF FIGURES

PREFACE

This thesis bears my name as the author, but the work described in it is the result of the concerted efforts of many people.

First of all, I would like to express my gratitude to my thesis advisor, Prof. David Snoke, whose support was indispensable throughout my graduate studies. He motivated me in a number of ways, always finding and posing a problem harder than the previous one. His insightful comments and suggestions were an essential aid in completing this work. Here I would also like to mention the many lengthy discussions with Prof. Albert Heberle, both about elementary or advanced physics problems and experimental techniques.

During the years, I have had the opportunity to work with a great number of people. I would like to thank my fellow graduate students, Ryan Balili, Garrett Burke, Sava Denev, Vincent Hartwell, Yingmei Liu, and Nicholas Sinclair, who all challenged me to clear the experimental or theoretical hurdles facing us, to critically think about the questions at hand. I am especially grateful to Vincent, who always lent me a listening ear and gave guidance when I came across theoretical or numerical difficulties. His contribution to these aspects of the thesis cannot be overrated.

Jonathan Withers and Koji Masuda helped me with the technical aspects of experiments, for which I am also grateful.

I am especially indebted to our collaborators at Lucent Technologies, Bell Labs, to Loren Pfeiffer and Kenneth West, who produced all samples used in the studies, and to Gang Chen and Ronen Rapaport, with whom I had the opportunity to work on the experiments described in Chapter 4 in this dissertation.

I also would like to thank the members of my graduate committee for their careful reading of the thesis. While it is still far from perfect, their suggestions and corrections were essential

in improving it.

And last, but not least, I would like to express my gratitude to my family, and in particular, to my wife, Anna, who stood by me through these wonderful, but sometimes difficult years.

This work has been financially supported by the Department of Energy and the University of Pittsburgh through a one-year Andrew Mellon pre-doctoral fellowship.

1.0 INTRODUCTION

The motivation behind this work stems from the general phenomenon of Bose-Einstein condensation (BEC). There are various bosonic entities that could undergo this intriguing phase transition, such as superfluid He [1] and alkali atoms [2, 3]. More recently, BEC has been reported in a semiconductor system, microcavity polaritons [4, 5, 6, 7]. The present thesis is a summary of the experimental work that we have done on another bosonic semiconductor system, that of quantum well excitons.

On the following pages, first we discuss BEC in general, with emphasis on two-dimensional systems, then introduce the system that we studied and give the details of the experimental techniques that we used. In Chapter 2 we demonstrate that the particles under study behave as a free gas, fulfilling the first requirement for BEC. In Chapter 3 we demonstrate how the temperature of excitons can be measured in an artificial potential created by inhomogeneous stress. The next chapter introduces a different trapping principle, that of electrostatic confinement. Since, according to the results of Chapter 3, excitons reach equilibrium in stress traps, we can investigate their interaction under equilibrium conditions. The results, and the a simple theory accounting for the experimental findings is given in Chapter 5. In the following chapter we investigate a new phenomenon, the reduction of luminescence intensity in deep stress traps, which can potentially be related to excitonic BEC. The findings in this chapter are scrutinized from the point of view of condensation. We close the thesis with a short outlook and in the appendix we discuss various numerical models describing exciton diffusion and the effect of exciton-exciton interaction on BEC.

1.1 EXCITONS AS CANDIDATES FOR BOSE-EINSTEIN CONDENSATION

Excitonic BEC in quantum wells is a recurring claim in the literature, but a thorough demonstration of the fulfillment of the four major requirements of this phase transition is still missing. These requirements are general and apply to any bosonic system, and can be summarized as follows.

1. First we need free particles which are not localized. It might happen that at low temperatures particles become trapped in local minima in a disordered potential, and they do not behave as a gas at all.
2. Second, in the case of quasi-particles, like excitons, the lifetime must be long compared to the equilibration time. Atoms also evaporate from magneto-optical traps, but the timescale of this process is of the order of seconds, compared to the equilibration time of tenths of seconds [2, 3].
3. Third, a suitable macroscopic trapping potential must be created.
4. Finally, it must be shown that thermal particles can sample this trapping potential during their lifetime, and that they reach equilibrium not only locally, but globally. The system evolves into the equilibrium distribution through drift and diffusion.

The first two points are trivial, but the third one needs further explanation. (The fourth is simply linked to the existence of a suitable trapping potential and adequate diffusion.)

In an ensemble of noninteracting particles, BEC sets in when the number of bosons reaches some threshold value, given by the number of particles that the *excited* states can support, i.e.,

$$N_{cr} = \int \frac{D(E)\,dE}{e^{\beta(E-\mu)} - 1} \ . \tag{1.1}$$

In order for the distribution function to be defined, $\mu < 0$, i.e., the chemical potential is lower than the ground state.

In 3D, neglecting the spin degeneracy, for particles of mass m and of system volume V, the density of states is

$$D(E) = \frac{V}{2\pi^2}\frac{\sqrt{2}m^{3/2}}{\hbar^3}\sqrt{E} \ , \tag{1.2}$$

thus the integral at $\mu \to 0$ leads to

$$N_{cr} = \zeta(3/2) \left(\frac{2\pi m k_B T}{\hbar^2} \right)^{3/2} , \tag{1.3}$$

where ζ is the Riemann zeta function.

In 2D, however, the density of states is a constant, and more importantly, does not tend to zero as $E \to 0$,

$$D(E) = \frac{Am}{2\pi\hbar^2} , \tag{1.4}$$

meaning that the integral does not have an upper bound for any $\mu < 0$, i.e., the excited states can support an arbitrarily large number of particles, thus the macroscopic occupation of the ground state cannot be expected. Another way of saying this is that the the condensate is unstable against thermal fluctuations.

By breaking the translational symmetry of the system, the effect of thermal fluctuations can be reduced. In the d-dimensional case, assuming a harmonic trapping potential of the form $V(r) = \frac{1}{2}\alpha r^2 = \frac{1}{2} m\omega^2 r^2$, the energy eigenvalues are given by $E_n = n\hbar\omega$. The degeneracy of each energy level is approximately $n^{(d-1)}$; thus the critical number of particles in the excited states can be obtained by setting the chemical potential to zero, i.e.,

$$N_{cr} = \sum_n \frac{1}{e^{\beta\varepsilon_n} - 1} \approx \int_0^\infty \frac{x^{d-1}\, dx}{e^{\beta\hbar\omega x} - 1} = \left(\frac{k_B T}{\hbar\omega} \right)^d \int_0^\infty \frac{y^{d-1}\, dy}{e^y - 1} = \left(\frac{k_B T}{\hbar\omega} \right)^d \zeta(d) \tag{1.5}$$

where we do not have the divergence that we encountered before [8]. The critical number should additionally be multiplied by the degeneracy factors related to the inner structure of particles. In the case of indirect quantum well excitons, it is equal to 4, as discussed below. If the number of particles is higher than that given in Eq. (1.5), the extra ones must go into the ground state.

One point that we should make here is that Eq. (1.5) simply links the critical temperature to the critical particle number, but does not stipulate which one is the "variable". In atomic experiments, usually the particle number is held constant and the temperature is lowered. In our case, we keep the temperature constant, and change the particle number, simply by changing the power of the laser beam that creates the excitons. When doing this, we implicitely assume that the exciton temperature does not depend on the laser power.

We also point out that the critical temperature at a fixed particle number and fixed potential is inversely proportional to the square of the particle mass. This readily explains the interest and one of the advantages of using excitons instead of atoms: the mass of an exciton is at least 10^5 times smaller than that of a typical alkali atom; thus, keeping all other conditions the same, the critical temperature is expected to be 10^2 higher.

We note here that in the case of strong repulsion, as in the case of coupled quantum well excitons, the interaction between particles renormalizes the trapping potential, in extreme cases even washing it out; thus, the estimate given above is rather crude, and warrants refinement. We will return to this problem in Chapter 5.

It is also important to note that in the presence of a trap, the condensation happens in real space, i.e., the ground state of the system is spatially localized. This has led several authors to make predictions as to how the condensate should manifest itself in the luminescence spectrum and spatial pattern [9, 10, 11, 12, 13].

As for verifying that DQW excitons fulfill the requirements listed above, we will discuss measurements on their diffusion, thus gaining insight into the relevant scattering processes and proving that these particles are indeed free. We can then compare the deduced scattering times to their lifetime, and check whether they can undergo a number of collisions during their lifetime. We have also determined the exciton temperature by measuring their distribution function in a trap. The presence of the trap makes it also possible to measure their interaction in a well-controlled and nearly equilibrium situation.

While the main motivation was to produce Bose-condensed excitons, the results of this work should have applications in other problems involving double quantum well excitons. Understanding the exciton-exciton interaction is important in non-linear optics, e.g. in AC Stark effect [14]. If one regards an exciton as an agent of energy transport, taking one photon from the point of its creation to the point of its decay, and this transport can be tailored in such a way as to define the point of creation and the point of decay, exciton transport could find important applications in optical signal processing, such as all-optical multiplexing, optical logic operations [15], or small-aperture "waveguides" [16]. This latter scenario would make use of the reduced wavelength of an exciton compared to that of light.

1.2 BASIC EXCITON PROPERTIES

1.2.1 Excitons in bulk material

The ground state of an undoped semiconductor is a completely filled valence and a completely empty conduction band. Of course, there are many bands in a semiconductor, but only a few are relevant at a particular energy scale, namely, the ones that can be connected by particular - in our case, optical - excitations. The elementary excitation of such a system occurs when, by some proper mechanism, e.g., the absorption of a photon, an electron is lifted from the valence band into the conduction band. The empty state left behind in the valence band is called a *hole*, with a positive charge. The consequence of the hole's positive charge is a mutual attraction between the valence band hole and the conduction band electron, which then bind, as in the case of a hydrogen atom. This bound particle is called the *exciton*, and its energy can be calculated as in the case of the hydrogen atom, with two modifications. The first is that the electron-hole pair must be created, i.e., a valence band electron must be given an energy equal to the band gap, and second, the Coulomb interaction is changed due to the presence of the underlying crystal. In the case of *Wannier* excitons, i.e., when the Bohr radius of the particles is much bigger than the lattice constant, the change in the Coulomb interaction can be taken into account by introducing an effective dielectric constant ϵ. Then, assuming isotropic and parabolic bands, the total energy of the exciton becomes

$$E_{ex} = E_{gap} - \frac{e^2}{2a_{ex}\epsilon\epsilon_0 n^2} + \frac{\hbar^2 k^2}{2(m_e + m_h)} \ , \tag{1.6}$$

where n is the principal quantum number, and the excitonic Bohr radius is given as

$$a_{ex} = \frac{\hbar^2 \epsilon\epsilon_0}{e^2 m_r} \tag{1.7}$$

with the reduced mass $m_r = \dfrac{m_e m_h}{m_e + m_h}$. Since we will be concerned with excitons in GaAs, taking the value of the zero frequency dielectric constant $\epsilon \approx 13$, and the reduced mass $m_r \approx 0.2\ m_0$ [18], where m_0 is the vacuum electron mass, we arrive at the conclusion that the exciton radius is on the order of $a_{ex} \approx 120$ Å. This size is much larger than the lattice constant $a_{\mathrm{GaAs}} \approx 5.65$ Å; thus, we are justified in introducing the effective dielectric

constant [17, 18, 19]. The exciton binding energy is given by the excitonic Rydberg energy $Ry_{ex} = \dfrac{e^2}{2a_{ex}\epsilon\epsilon_0} \approx 8$ meV for GaAs.

The motion of the excitons can be confined to two dimensions in two dimensional quantum wells. When the bulk exciton radius becomes comparable to the width of the quantum well, the relations above will be modified. Due to the fact that the electron and hole are closer to each other, the binding energy increases rapidly as the well width, L, is reduced, and can be approximated by the relation $Ry^{\alpha}_{ex} = Ry^{3D}_{ex}/[1+(\alpha-3)/2]^2$, where $\alpha = 3-e^{-L/2a^{3D}_{ex}}$ is the effective dimension of the system [20]. As a consequence, the Bohr radius is reduced. For a truly 2D exciton, the binding energy is four times the bulk value, while the Bohr radius is reduced by a factor of 2 [14]. Hrivnák showed that for a wide range of practical values of the thickness, the Bohr radius assumes the approximate functional dependence $a^{2D}_{ex} = (a^{3D\,2}_{ex} L)^{1/3}$ [21], though it obviously fails for $L \to 0$.

1.2.2 The band structure of GaAs

In order to understand the properties of an exciton, we need to study the underlying band structure and symmetries of the system. GaAs crystallizes in a zinc-blende structure in a face-centered cubic lattice, in which each atom of one type has four nearest neighbors of the other type located at the vertices of a tetrahedron. As a result of this configuration, GaAs possesses T_d point group symmetry [18, 22, 23], as shown in Fig. 1

At the Γ point, the valence band of bulk GaAs is made up of p-like atomic states, which means, that taking the spin into account, the Γ point is six-fold degenerate. The atomic states themselves possess Γ_5 symmetry in T_d. At the Γ point, the full symmetry of the valence band holes is obtained by multiplying Γ_5 by the irreducible representation of the spin, i.e.,

$$\Gamma_h = \Gamma_5 \otimes \Gamma_{1/2} = \Gamma_7 \oplus \Gamma_8 \ . \tag{1.8}$$

The physical process corresponding to this splitting is the spin-orbit interaction, and results in the two-fold degenerate Γ_7 *split-off*, and the four-fold degenerate Γ_8 band. In GaAs, the spin-orbit splitting energy is about 340 meV, slightly changing with temperature [18].

The Γ_8 band is made up of two heavy holes ($J_z = \pm 3/2$)and the two light holes

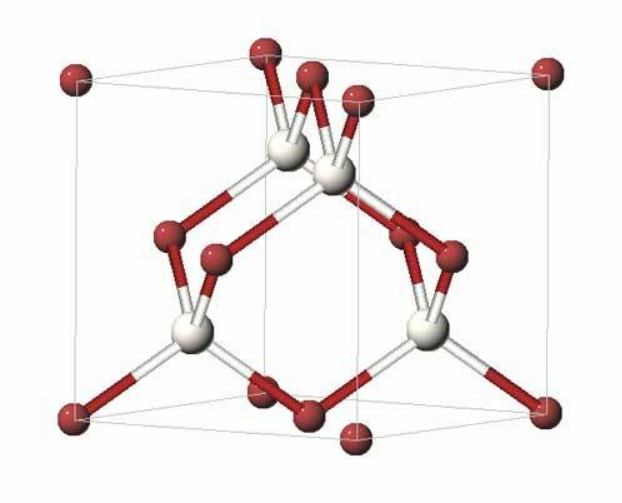

Figure 1: The crystal structure of GaAs.

($J_z = \pm 1/2$), with effective masses m_{hh},m_{lh}. The designation *heavy* and *light* is somewhat inaccurate, for the effective masses of the holes depend on the direction of their momentum, and in GaAs, the light hole is heavier than the heavy hole in the [001] direction, while in directions perpendicular to it, the opposite is the case. The hole bands are said to be *warped*. This is described by the Luttinger-Kohn Hamiltonian

$$\begin{aligned} H &= \frac{\hbar^2}{2m_0}\left[(\gamma_1 + 5\gamma_2/2)k^2 - 2\gamma_2(k_x^2 J_x^2 + k_y^2 J_y^2 + k_z^2 J_z^2)\right. \\ &\quad \left. -4\gamma_3\{(k_x k_y + k_y k_x)(J_x J_y + J_y J_x) + c.p.\}\right] , \end{aligned} \tag{1.9}$$

where $\gamma_1 \approx 7, \gamma_2 \approx 2, \gamma_3 \approx 3$ are the Luttinger parameters [18, 14], and *c.p.* stands for cyclic permutation. This Hamiltonian has the two degenerate eigenvalues

$$E = \frac{\hbar^2}{2m_0}\left[\gamma_1 k^2 \pm \sqrt{4\gamma_2 k^4 + 12(\gamma_3^2 - \gamma_2^2)(k_x^2 k_y^2 + k_x^2 k_z^2 + k_y^2 k_z^2)}\right] \tag{1.10}$$

Thus, in the [001] direction, the light and heavy hole masses are given by [24]

$$m_{lh} = \frac{m_0}{\gamma_1 + 2\gamma_2} \approx 0.09\ m_0 \tag{1.11}$$

$$m_{hh} = \frac{m_0}{\gamma_1 - 2\gamma_2} \approx 0.3\ m_0\ , \tag{1.12}$$

while in the [100] or [010] directions (in the plane perpendicular to [001]),

$$m_{lh} = \frac{m_0}{\gamma_1 - \gamma_2} \approx 0.2\ m_0 \tag{1.13}$$

$$m_{hh} = \frac{m_0}{\gamma_1 + \gamma_2} \approx 0.12\ m_0\ . \tag{1.14}$$

In the cubic symmetry, the [100], [010], and [001] axes are equivalent, but the quantization direction, [001] breaks this symmetry, because the x and y component of the angular momentum can be 0, but the z component is always non-zero. This leads to different masses along z and the $x - y$ plane. Although the [100] and [010] directions are equivalent, the effective mass of the hole is different in the [110], [$1\bar{1}0$], [$\bar{1}10$], and [$\bar{1}\bar{1}0$] directions, which lie in the same plane. It is then common practice to introduce an average hole mass for the plane, taking these differences into account [25]. Then, in the plane, the average heavy hole mass is about 0.2 m_0, and the light hole mass is about 0.15 m_0.

1.2.3 Excitons in quantum wells

Quantum wells are formed when a layer of semiconductor of type A is sandwiched between two layers of semiconductor of type B. If these two types are chosen properly, the spatial profile of the minimum of the conduction band and of the valence band will form a well for electrons and holes in the direction perpendicular to the layers, i.e., in the growth direction. Depending on whether the conduction band minima and valence band maxima are located in the same or different materials, Type I and Type II can be distinguished, as shown in Fig. 2.

The presence of confinement in one direction has fundamental consequences for the energy spectrum of the electrons and holes. In particular, in AlGaAs/GaAs quantum wells, if the growth direction is along the [001] crystal axis, the T_d symmetry of the bulk material is lowered to D_{2d}. In the reduced symmetry, the original Γ_8 band is split into two, with Γ_7 (heavy hole) and Γ_6 (light hole) symmetries [22]. The physical process producing the splitting is the difference in the confinement energies of the two types of holes. Assuming

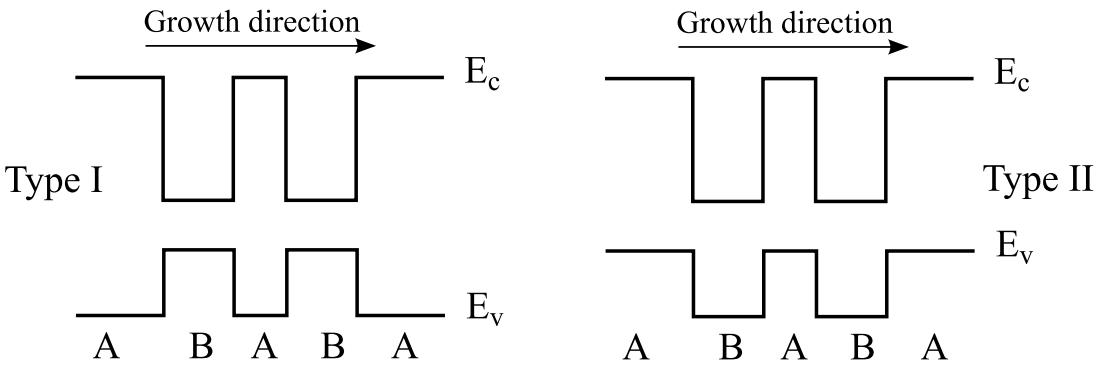

Figure 2: One dimensional potential, $V(z)$, of the valence and conduction bands in Type I (left) and Type II (right) double quantum wells.

infinite barriers and a quantum well thickness L, the confinement energy for the n-th confined state is given as

$$E_{cf} = \frac{n^2\hbar^2\pi^2}{2mL^2} \ . \tag{1.15}$$

Thus the heavy and light hole bands become separated, since their confinement energy is inversely proportional to the effective hole mass. (Here we have to take the hole mass relevant to the confinement direction.) This is shown in Fig. 3

Obviously, the energetic separation of these two bands is determined by the well width, but for a typical value $L = 100$ Å and [001] direction, it is approximately 40 meV; therefore, we can neglect the light hole band at temperatures lower than about 500 K. We will be concerned with this temperature range, and therefore consider only excitons from the heavy hole valence band and the electrons from the conduction band.

Having obtained the electronic (Γ_6) and the relevant hole (Γ_7) bands, we can construct the exciton wave function by taking the direct product of these states. Since the heavy hole band has a total spin of 3/2, while the conduction band possesses a spin of 1/2, the resulting excitons states will form a pair of doublets, according to the decomposition in D_{2d} symmetry

$$\Gamma_6 \otimes \Gamma_7 = \Gamma_3 \oplus \Gamma_4 \oplus 2\Gamma_5 \ . \tag{1.16}$$

The Γ_5 state is an optically active (bright) doublet, if the polarization of the electric field is in the plane of the quantum wells, while Γ_3 and Γ_4 are optically inactive (dark) [26, 27]. The physical process responsible for the splitting of the four states is electron-hole exchange. The magnitude of the splitting is around 100 μeV in three dimensions. In two dimensions, the splitting is between 10 and 20 μeV for Type I single quantum wells [29], and is greatly reduced due to the small overlap of the electron and hole wavefunctions in Type II quantum wells. Van Kesteren et al. determined the splitting in Type II GaAs/AlAs quantum wells of various thicknesses by measuring the quantum beat frequency between adjacent levels, and found that, in a wide range, the splitting can be approximated as $E_{sp} \approx 110 \cdot e^{-d/7.5}$, where the thickness, d, is measured in Å, while the energy is measured in μeV [28]. Similar measurements for double quantum wells are still missing in the literature, but based on their results and the small overlap of the electron and hole wavefunctions, the splitting is certainly only a couple of μeV at most. Incidently, the bright excitons lie higher in energy, which led Combescot et al. [30] to argue that since the ground state of the system is dark, so would be the excitonic BEC, and this might be one reason why it has not yet been directly observed, though several groups have presented evidence in favor of bright exciton condensation [31, 32, 33, 34].

1.3 EXPERIMENTAL CONSIDERATIONS

1.3.1 Optical components and data acquisition

The main parts of our experimental setup are shown in Fig. 4. All experiments were conducted in a Janis Vari-Temp cryostat in the low temperature regime, between 1.4 K and about 30 K. The lower side of the range was limited by the pumping power of the available vacuum pumps, while the higher limit is given by the finite binding energy of excitons. At the lowest temperatures the sample was immersed in reduced vapor pressure He liquid, while at higher temperatures it was in He vapor.

In almost all experiments, we were interested in the dynamical behavior of the system;

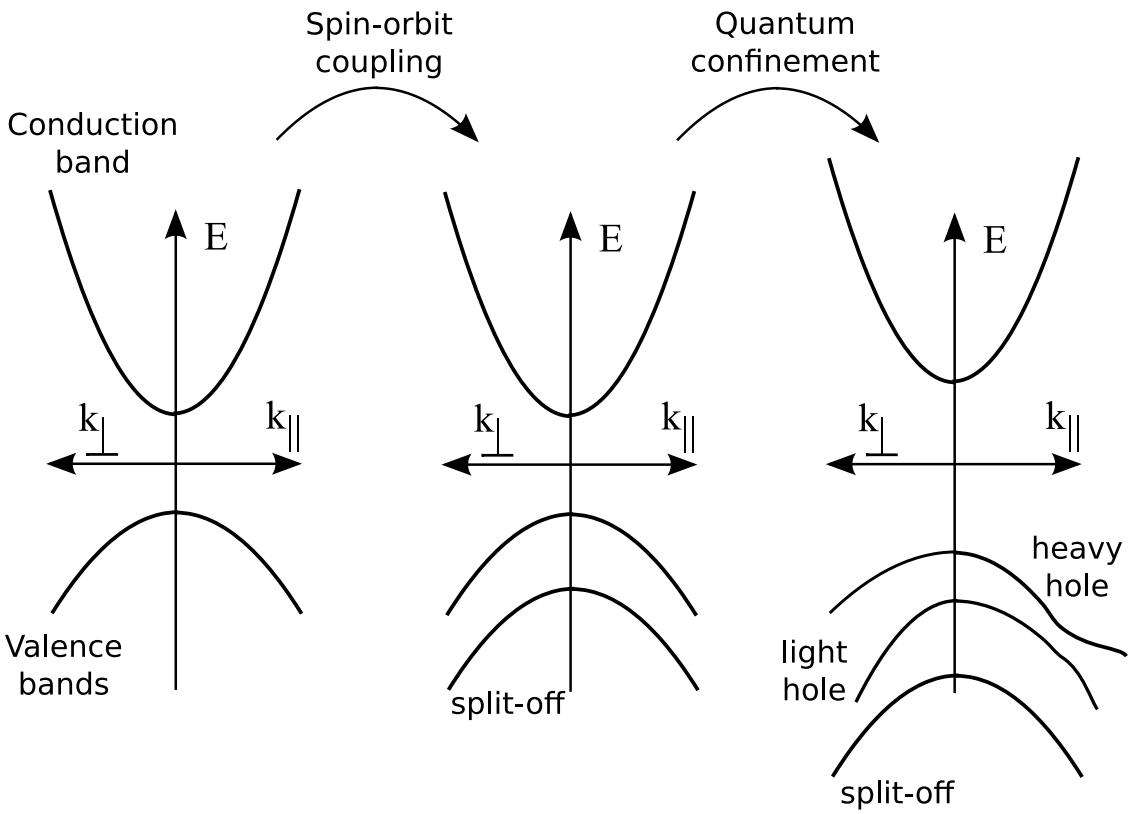

Figure 3: The evolution of the band structure of GaAs at the Γ point as the symmetry of the system is lowered. $k_\perp$ is in the direction perpendicular to the planes, while $k_\parallel$ is in the planes.

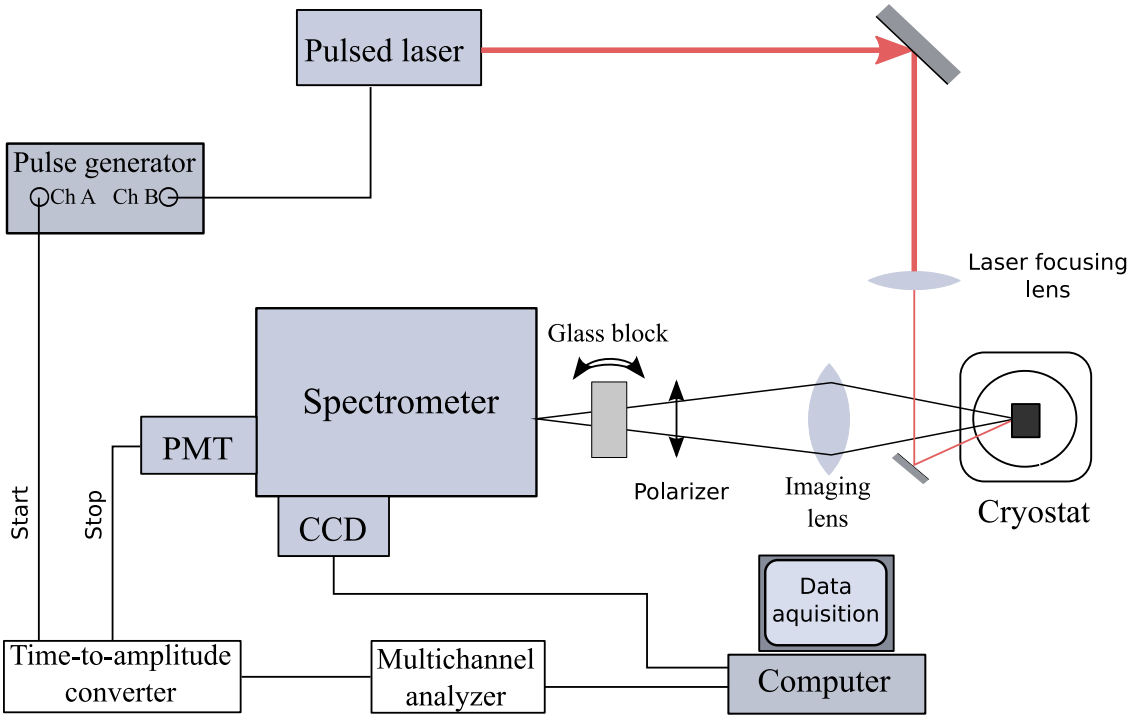

Figure 4: The experimental setup.

thus we used pulsed laser sources mostly. These were mode-locked Titanium-Saphire laser, a cavity-dumped dye laser pumped by a frequency-doubled Nd:YAG laser, or a semiconductor diode laser. The laser pulse frequencies relevant to the experiments were of the order of a couple of hundred kHz, i.e., successive pulses were separated in time by a couple of μs. While the lasers are pulsed, all of them have some background light emission, and since the background light is on all the time, this can contribute a considerable portion to the total power. Typically, about 10% of the total power is emitted as a continuous wave background, and the remaining 90% constitutes the pulses.

In most experiments, we tuned the laser light to the resonant energy of the quantum wells. Excitation at energies higher than the single-well absorption line would produce excess heat in the exciton ensemble, for excitons would be created with large kinetic energy. In the case of the Titanium-Saphire and dye lasers, tuning was achieved by rotating an intracavity birefringent crystal, thus changing the transmission peak of the cavity, while the diode laser could be tuned by changing its operating temperature.

The exciton luminescence was projected onto an Acton SpectraPro 2500i imaging spectrometer, which preserves the spatial information along one axis, while it disperses light along a perpendicular axis, as shown in Fig. 5. Time resolution was obtained either by time-correlated photon counting with a Hamamatsu photomultiplier tube (PMT) or by a time-gated image intensified LaVision NanoStar CCD camera, with the lasers supplying a trigger signal, defining the reference point of time. The time resolution of the PMT is about 30 ps, while that of the CCD is 5 ns.

Extracting the spatial information from a measurement with the CCD is obvious, for the detector is a plane. Our system provided a spatial resolution of about 3.3 μm per pixel. Doing the same with the PMT is not so trivial, for the PMT is a single point device. In order to acquire spatial information, we applied a small pinhole of size 50-100 μm on the entrance slit of the spectrometer, thus masking the projected image and collecting light from particular points only. Since the magnification of the imaging objective was about 4, a pinhole of this size allows a spatial resolution of about 13 μm. By rotating the small glass block in front of the spectrometer, we could choose the point of interest and scan across the surface of the samples. This method is similar to that described in detail in the work of

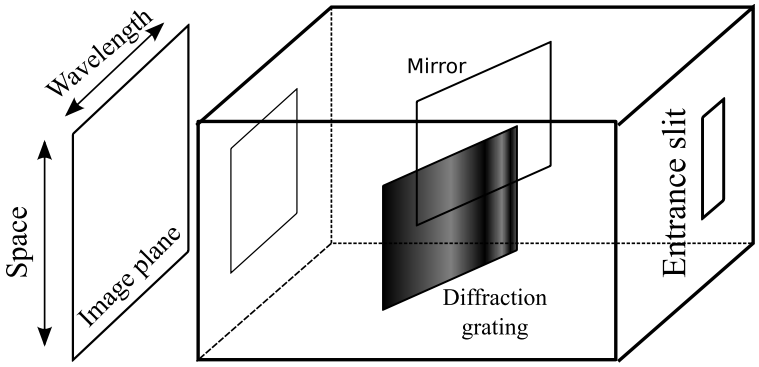

Figure 5: Imaging spectrometer.

Gilliland et al. [35].

1.3.2 Sample preparation

In the experiments, we used double quantum well samples, shown in Fig. 6, which have many advantages over single quantum wells. As discussed below, the average exciton lifetime in these structures can be as long as tens of μs, while the binding energy is not reduced significantly. The exciton energy can conveniently be tuned by changing the bias potential. Finally, the repulsive force between particles prevents the formation of excitonic molecules. The double quantum well samples were grown by means of molecular beam epitaxy (MBE) on n-doped GaAs [001] substrates with p-type capping layer by Loren Pfeiffer and Kenneth West of Bell Labs. The quantum wells themselves were not doped.

The doping of the layers was to provide a diode-type structure, which was typically biased in the reverse direction. The reason for this is that any current flowing through the sample brings high energy carriers into the system, which would then impart their kinetic energy to excitons through collisions. Moreover, the presence of free carriers screens the Coulomb interaction, reducing excitonic lifetimes and binding energies, and finally, the increased collision rate reduces the diffusion. In order to do away with these unwanted effects, the outer barriers also included superlattices built up of 20 successive layers of AlAs/AlGaAs,

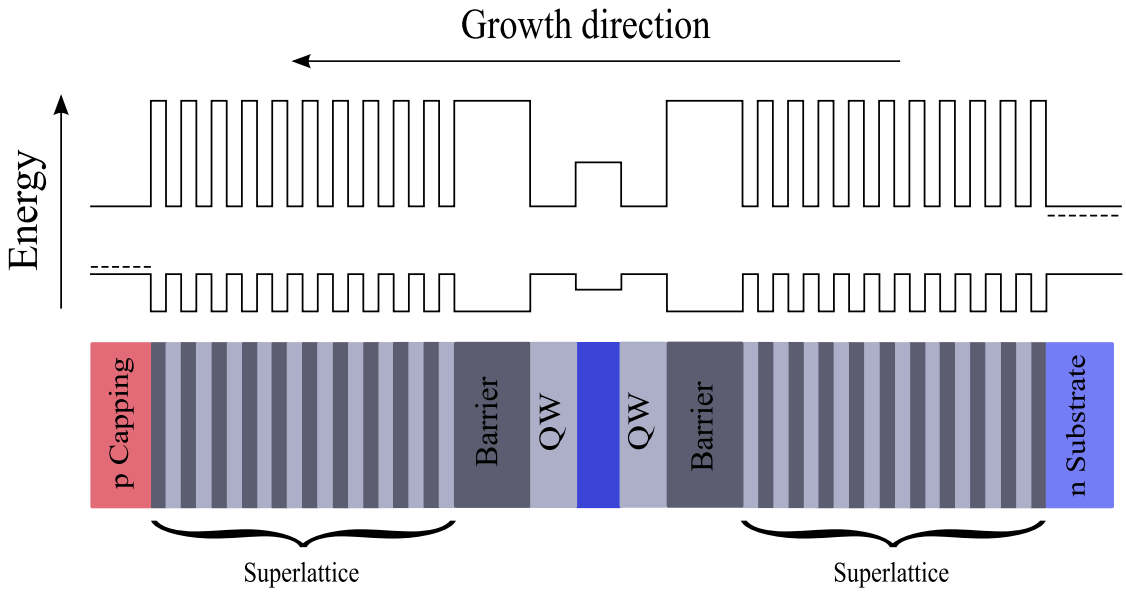

Figure 6: The coupled quantum wells and the corresponding band structure. The superlattice is made up of alternating AlAs/AlGaAs layers of thickness 60 Å.

similar to, e.g., Ref. [36]. The superlattices act as traps for the charge carriers, but are transparent to the light resonant with the exciton energy. This reduced the dark current passing through the double quantum wells to below 1 μA/cm^2.

The GaAs quantum wells have thicknesses between 80 and 140 Å, and are always separated by a $Al_{0.3}Ga_{0.7}As$ barrier of thickness 40 Å. A typical sample and the resulting band structure is shown in Fig. 6.

As described in Chapter 3, one trapping method is to apply inhomogeneous stress on the samples. This requires preparation of relatively thin (100-150 μm) wafers, because standard GaAs wafers are 500 μm thick. In order to reduce the thickness, we polished the wafers to the desired size in a bromine-methanol solution.

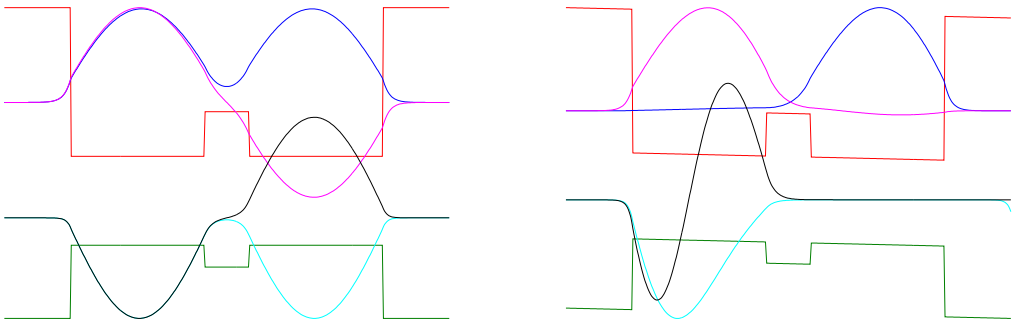

Figure 7: The band structure and the lowest-lying wavefunctions of the coupled quantum wells. a) zero applied electric field. b) nonzero applied field.

1.4 FURTHER CONSIDERATIONS ON EXCITON PROPERTIES

In this section we briefly overview several exciton properties relevant to our experiments, such as the energy and lifetime dependence on applied field and the lifetime as a function of temperature.

1.4.1 Quantum confined Stark effect

When voltage is applied perpendicular to the wells (along the growth direction), the bands tilt and the electrons and holes separate, leading to the appearance of spatially "indirect" excitons. This is shown in Fig. 7. At the arrival of the laser pulse, electrons are excited in both quantum wells; however, only the lowest lying indirect exciton level is favorable energetically. Therefore, electrons move to the right, while holes move to the left. This tunneling of electrons and holes happens in about 1 ns [37].

The tilting of the bands also results in the so-called quantum confined Stark effect, which is the shift of the energy of the indirect exciton [38]. From the simple geometrical picture one would expect the energy of the indirect exciton to shift linearly with the external field. However, this is true only for high fields, because the underlying electron and hole

wavefunctions also change, thus changing the corresponding eigenenergies.

In zero field, we have two electron and two hole wavefunctions in the lowest quantum well bands: one is symmetric while the other one is antisymmetric. Out of these four states, four exciton states can be created, depending on which electron is paired with which hole. The exciton Hamiltonian is given by

$$H_{ex} = H_e^0 + H_h^0 + H_{2D} + U + E_{gap} \ , \tag{1.17}$$

where E_{gap} is the gap energy, H^0 is the single-particle electron or hole Hamiltonian of the form [40]

$$H_{e,h}^0 = -\frac{\hbar^2}{2}\frac{\partial}{\partial z}\frac{1}{m_{e,h}}\frac{\partial}{\partial z} + V(z) - qFz \ , \tag{1.18}$$

with m being the respective mass, $V(z)$ the confining potential and F the external electric field. H^0 accounts for the motion along z only, thus

$$H_{2D} = -\frac{\hbar^2}{2(m_e + m_h)}\left[\frac{\partial^2}{\partial x^2} + \frac{\partial^2}{\partial y^2}\right] \ . \tag{1.19}$$

Finally, U is the Coulomb potential between the two particles,

$$U = \frac{e^2}{(x^2 + y^2 + (z_e - z_h)^2)\epsilon\epsilon_0} \ . \tag{1.20}$$

While solving the full Schrödinger equation in one step is hard, we can separate the various parts and build a variational solution from them. The eigenfunctions of H_e^0 and H_h^0 can easily be obtained through numerical means, once the band structure and the external field are given. Starting with $\varphi_e(z_e)$ and $\varphi_h(z_h)$ as the lowest energy eigenfunctions of the single particle Hamiltonian, the variational wavefunction is taken as

$$\Psi_{ij} = N_{ij}\varphi_e^i(z_e)\varphi_h^j(z_h)\exp\left[-\frac{\sqrt{x^2 + y^2 + \alpha_{ij}(z_e - z_h)^2}}{R_{ij}}\right] \ , \tag{1.21}$$

where α_{ij} and R_{ij} are variational parameters and N_{ij} is a normalization constant. The indices i, j specify which wavefunctions we used for building the variational function, i.e., i and j refer to whether the underlying electron and hole wavefunction are symmetric or antisymmetric [39, 40, 41].

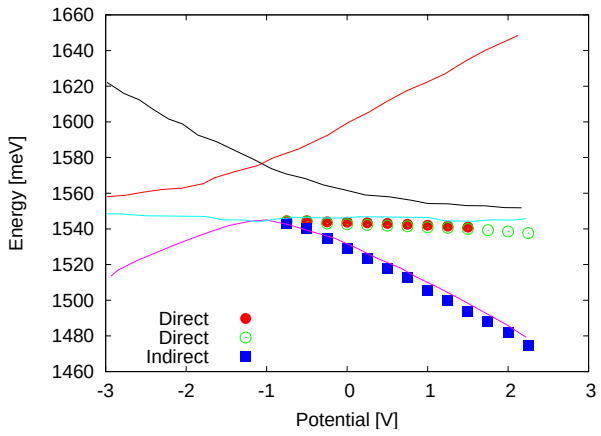

Figure 8: Measured energy of the three lowest lying exciton states as a function of the applied external field. The lines show all four states as given by the theory discussed in the text.

Solving for the variational parameters gives the eigenenergies. Fig. 8 shows the energies of the four lowest lying exciton states in a 120-Å-thick double quantum well as a function of the applied potential. We also show the measured energies for the same structure. However, since the laser excitation was energetically located between the highest-lying level and the other three, only those three lower lying levels are excited and can be detected in the luminescence. The applied potential is not zero at zero energy shift, because of the presence of the built-in electric field in the *p*-*i*-*n* structure.

The presence of the quantum confined Stark effect has a very important application in trapping excitons. At first sight it might seem counter-intuitive to assume that excitons, being charge neutral, can be trapped by electric field. However, as Fig. 8 shows, the exciton energies depend on the value of the *local* electric field; namely, the highest field corresponds to the lowest energy. Thus, producing a non-uniform electric field with a well-defined maximum leads to an energy minimum. This has been utilized in various configurations [15, 42, 43, 44, 45, 46] to trap excitons, and we will come back to this point in Chapter 4.

1.4.2 Lifetime of quantum well excitons

1.4.2.1 The role of the overlap integral As we can see in Fig. 7, as the external electric field is increased, the electron-hole wavefunction overlap also changes. This, in turn, determines the lifetime of excitons, because in order for the exciton to radiatively decay, the electron must find a hole, and the probability of this happening is simply the overlap integral. With the knowledge of the wavefunctions, we can calculate the oscillator strength of the various pairs of states. The overlap integral of the electron and the hole is given by

$$f_{ij} = \int_{-\infty}^{\infty} \Psi_{ij}(x_e = x_h, y_e = y_h, z_e = z, z_h = z)\, dxdydz = N_{ij} \int_{-\infty}^{\infty} \varphi_i(z)\varphi_j(z)\, dz \ . \quad (1.22)$$

Fig. 9 shows the lifetime of the the lowest lying exciton state in a 120-Å wide quantum well structure as a function of the electric fields. The solid line is proportional to the inverse of the overlap integral. The difference of a multiplicative factor between the theory and the measurement is due to the fact that the theory does not state anything about the intrinsic exciton lifetime, it only predicts by how much the lifetime changes as the overlap integral changes.

Szymańska and Littlewood [47] calculated the oscillator strength based on a plane-wave expansion, and obtained very similar results. We also note here that the dependence of the lifetime on the electric field can find a practical application as a "photon storage" device; photons can be stored in the indirect exciton states (high electric potential), and they can be released by pulling the electric potential to ground. However, it should be pointed out that this device does not preserve the polarization of photons, because the two bright and two dark exciton states come to thermal equilibrium in a matter of a couple of hunder ps. An experimental demonstration can be found in the work of Winbow et al. [48].

1.4.2.2 Photon emission on the light cone The external electric field is not the only factor affecting the lifetime of excitons: when an exciton is destroyed, a photon is created. Since momentum conservation perpendicular to the plane is relaxed, in addition to energy, in-plane momentum must also be conserved, i.e., only particles in a small fraction of the phase space, the so-called radiative zone, can decay by radiation.

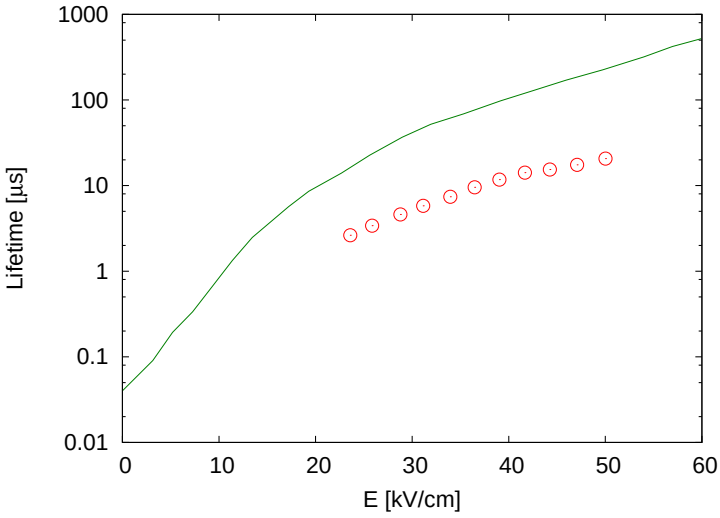

Figure 9: Measured lifetime of the lowest lying exciton state (points) as a function of the applied external field, defined by the potential difference between the capping layer and the substrate divided by their distance. The solid line is inverse of the oscillator strength given by Eq. 1.22.

Given that in quantum wells, excitons are confined to move in a plane, the exciton energy is

$$E_{\text{ex}} = E_{\text{gap}} + E_{cf} - E_b + \frac{\hbar^2 k_\parallel^2}{2m_{ex}} \ , \tag{1.23}$$

where $\hbar k_\parallel$ is the in-plane momentum, and E_b is the binding energy. The photon's energy in vacuum, i.e., after leaving the crystal, is

$$E_{ph} = \hbar c k = \hbar c \sqrt{k_\perp^2 + k_\parallel^2} \ , \tag{1.24}$$

where $\hbar k_\perp$ is the out-of-plane momentum. There are many values of $k_\perp$ satisfying this condition, since denoting $E_0 = E_{\text{gap}} + E_{cf} - E_b$ and solving $E_{\text{ex}} = E_{ph}$ for $k_\perp$ yields

$$k_\perp = \sqrt{\left(\frac{1}{\hbar c}\right)^2 \left(E_0 + \frac{\hbar^2 k_\parallel^2}{2m_{ex}}\right)^2 - k_\parallel^2} \ , \tag{1.25}$$

which has a real root, whenever

$$\frac{1}{\hbar c}\left(E_0 + \frac{\hbar^2 k_\parallel^2}{2m_{ex}}\right) > k_\parallel \ , \tag{1.26}$$

i.e., if

$$k_\parallel < k_\parallel^* = \frac{c m_{ex} - \sqrt{c^2 m_{ex}^2 - 2E_0 m_{ex}}}{\hbar} \approx 7.6 \cdot 10^4 \text{ cm}^{-1} \tag{1.27}$$

or

$$k_\parallel > k_\parallel^* = \frac{c m_{ex} + \sqrt{c^2 m_{ex}^2 - 2E_0 m_{ex}}}{\hbar} \approx 10^{10} \text{ cm}^{-1} \ . \tag{1.28}$$

The numerical estimates were obtained using $0.2\, m_0$ for the exciton mass, and the gap energy $E_{\text{gap}} = 1.5$ eV for E_0. We can easily see that the second inequality would require $k_\parallel$ to be beyond the Brillouin zone, estimated by $\pi / a_{GaAs} \approx 5.5 \cdot 10^7$ cm^{-1}.

Thus, all excitons up to the energy $\Delta E = \hbar^2 k_\parallel^{*2} / 2m \approx 18\ \mu$eV can participate in photon emission. The number of these excitons can be obtained from

$$n_{rc}(T) = \int_0^{\Delta E} D(E) f(E)\, dE \ , \tag{1.29}$$

where $D(E)$ is the density of states. Assuming a Boltzmannian distribution for the occupation, the total particle number is

$$n_{tot} = N_0 \int_0^\infty D(E) f(E)\, dE \ . \tag{1.30}$$

Now, in 2D, the density of states is constant; thus, for the fraction of optically active particles, we get

$$\frac{n_{rc}(T)}{n_{tot}} = \frac{N_0 \int_0^{\Delta E} D(E) e^{-E/k_B T}\, dE}{N_0 \int_0^\infty D(E) e^{-E/k_B T}\, dE} = 1 - e^{-\Delta E/k_B T} \ . \tag{1.31}$$

When $\Delta E < k_B T$, we can expand the exponential and retain the linear term only, i.e.,

$$\frac{n_{rc}(T)}{n_{tot}} = 1 - e^{-\Delta E/k_B T} \approx \frac{\Delta E}{k_B T} \ . \tag{1.32}$$

From this, the rate of change of the exciton population is

$$\frac{\partial n_{tot}}{\partial t} = -\frac{n_{rc}(T)}{\tau_{\text{int}}} = -\frac{n_{tot} \Delta E}{\tau_{\text{int}} k_B T} \ , \tag{1.33}$$

where τ_{int} is the intrinsic lifetime of excitons. Therefore, the effective lifetime is

$$\tau_{rad} = \tau_{\text{int}} k_B T / \Delta E \ , \tag{1.34}$$

linear in temperature.

Feldmann et al. [49, 50] noted that phonon broadening of the exciton dispersion also plays a role in the lifetime. In practice, the exciton energies are smeared out, due to the fact that the homogeneous linewidth is not zero at finite temperatures. This also leads to a relaxation of the energy conservation condition, as shown in Fig. 10.

The linewidth of the excitons is given by

$$\Delta(T) = \alpha_0 + \beta T \ , \tag{1.35}$$

where α_0 is the temperature independent contribution, and $\beta \approx 10 \mu$eV/K [49]. As shown in the figure, now an ensemble of excitons can interact with photons. The calculation leading to

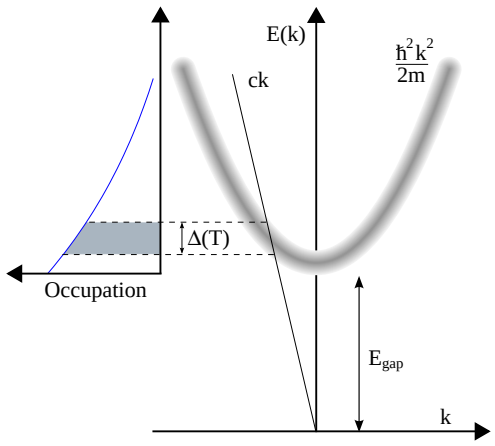

Figure 10: The dispersion relation of the exciton and the photon. Also shown is the segment of the exciton distribution that fulfills the condition of momentum conservation. The horizontal axis is the in-plane momentum.

the change in lifetime is very similar to what we presented above, and also gives a dependence linear in temperature.

The lifetime as a function of temperature is shown in Fig. 11. From the figure we see that Eq. (1.34) holds only at high temperatures, when $k_B T > \Delta(T)$, and in the lower-temperature range the lifetime deviates from the linear relation. However, we should point out that the reason for this might be that the exciton temperature is not equal to the bath temperature. We will discuss this problem at length in Chapter 3.

1.5 UPPER LIMITS ON THE EXCITON DENSITY

1.5.1 Fermionic versus bosonic nature

Since excitons are composite bosons, made up of two fermions, the question naturally arises, to what degree can these particles be treated as bosons, and what consequences it has if they cannot.

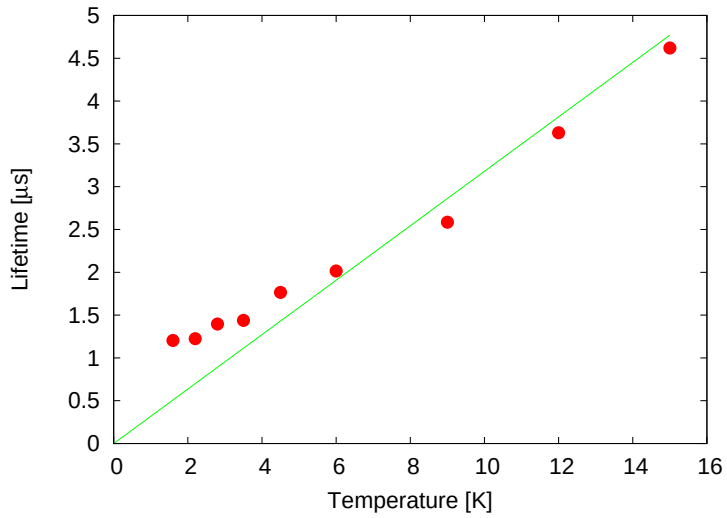

Figure 11: Measured lifetime of excitons in a 100-Å double quantum well structure as a function of temperature (red dots). Also shown is the linear relation predicted by Eq. (1.34) (straight line). The bias voltage was 0.8 V for all points.

A naïve estimate can be obtained, if we stipulate that the mean inter-particle distance is larger than the exciton Bohr radius, i.e, for the two dimensional case,

$$N a_{ex}^2 / A \leq 1 \ . \tag{1.36}$$

If this condition is not satisfied, phase space filling occurs, and the hydrogen-like wavefunction is no longer a proper description of the exciton.

However, in a recent paper, Combescot argues that this estimate is far too crude [51]. The argument is as follows.

For zero total momentum excitons, the creation operator is

$$B^\dagger = \sum_{\vec{k}} \phi_{\vec{k}} a_{\vec{k}}^\dagger b_{-\vec{k}}^\dagger \ , \tag{1.37}$$

where $\phi_{\vec{k}}$ is the Fourier transform of the ground state wave function, and $a_{\vec{k}}^\dagger$ and $b_{-\vec{k}}^\dagger$ are the electron and hole creation operators. One then takes the expectation value

$$\langle \Psi_N | 1 - [B, B^\dagger] | \Psi_N \rangle \tag{1.38}$$

on the Ψ_N N-exciton state. For perfect bosons this expectation value should be zero, for the commutator in that case is equal to 1. The expectation value can be obtained as

$$\langle \Psi_N | 1 - [B, B^\dagger] | \Psi_N \rangle = 2 \left(1 - \frac{F_{N+1}}{F_N} \right) \ , \tag{1.39}$$

where the dimensionless number F_N is given by

$$F_N = 1 - \frac{N(N-1)}{2} \sum_{\vec{k}} |\phi_{\vec{k}}|^4 \tag{1.40}$$

Using the approximate wave function

$$|\phi_{\vec{k}}|^2 = \frac{2\pi a_{ex}^2}{A} \frac{1}{(1 + k^2 a_{ex}^2/4)^3} \ , \tag{1.41}$$

F_N can be calculated, and the condition for the deviation of the bosonic commutator to be much less than 1 becomes

$$5N a_{ex}^2 / A \ll 1 \ . \tag{1.42}$$

Taking the 2D exciton Bohr radius $a_{ex} = 60$ Å [52], this implies

$$n \ll 2 \cdot 10^{11} \mathrm{cm}^{-2} \ . \tag{1.43}$$

1.5.2 Interaction

In Eq. (1.5) we obtained the critical exciton number in a simplified, non-interacting model. Excitons will be weakly interacting if the energy associated with the interaction, is small compared to their kinetic energy [16], i.e., if

$$nU \leq \frac{\hbar^2/a_{ex}^2}{2m_{ex}} \ , \tag{1.44}$$

where n is the 2D density of particles, and U is the interaction potential for hard-core bosons [53, 54],

$$U = \frac{2\pi\hbar^2}{m_{ex}} \frac{1}{\ln(1/na_s^2)} \ , \tag{1.45}$$

where a_s is the s-wave scattering length. For a hard-core potential, $a_s = a_{ex}$ [53], thus, when $na_s^2 \ll 1$, the condition above becomes

$$\exp(-4\pi a_s^2 n) > a_s^2 n \ , \tag{1.46}$$

therefore, using $\exp(-4\pi a_s^2 n) \approx 1 - 4\pi a_s^2 n$,

$$n \leq \frac{1}{a_s^2(1+4\pi)} \ , \tag{1.47}$$

which is a more stringent requirement than the one in Eq. (1.43).

In principle, similar to the hydrogen molecule, biexcitons could form, if the interaction between excitons is attractive. However, for indirect excitons in double quantum wells, the interaction is entirely repulsive. We have seen that the electrons and hole are in different layers, which means that the indirect excitons are small dipoles aligned parallel to each other. Therefore, their interaction is always repulsive, which would not support a bound state. The argument based on the dipole repulsion breaks down at very small quantum well separations. As Lozovik and Berman pointed out, when the barrier between the two quantum wells is less than about 10% of the 3D Bohr radius, the interaction can be attractive [55], and a new bound state, the biexciton, can form.

We also point out that strong exciton-exciton interaction does not necessarily mean that BEC cannot occur for these particles. Superconductivity is an example of Bose-Einstein condensation in a strongly interacting system.

1.5.3 Mott transition

Even if all electrons and holes paired up and formed excitons, at finite temperature excitons would continuously dissociate and produce free charge carriers. However, free carriers screen the Coulomb interaction, thus reducing the binding energy, and increasing the dissociation rate. If the density of free carriers is high enough at the first instant, this becomes a runaway process, and an electron-hole plasma will be left behind. This is called the *ionization catastrophe*.

Snoke [56], and Crawford and Snoke [57] calculated the ionization threshold, taking the two-dimensional screening length [58, 59]

$$l_{sc} = \frac{2\epsilon k_B T}{e^2 n} \ . \tag{1.48}$$

The screening length determines the excitonic Rydberg through the relation

$$Ry(l) = \begin{cases} Ry(0)\left(1 - \frac{2}{1+\sqrt{2l_{sc}/a_{ex}}}\right) \ , & l_{sc}/a_{ex} > \frac{1}{2} \\ 0 \ , & l_{sc}/a_{ex} \leq \frac{1}{2} \end{cases} \tag{1.49}$$

where a_{ex} is the two-dimensional exciton Bohr radius. The number of excitons $n_{ex} = n - n_e$, where n is the total pair density, and n_e is the number of electrons. These three numbers satisfy the balance equation

$$n_e^2 + n_e\left(\frac{n_Q}{e^{\mathrm{Ry}(n_e,T)/k_BT} - 1}\right) - \frac{n n_Q}{e^{\mathrm{Ry}(n_e,T)/k_BT} - 1} = 0 \ , \tag{1.50}$$

where n_Q is a normalization constant, the effective density of states. This equation can then be solved for n_e at any given n. Aouani et al. [61] derived a similar dependence, but they took only the approximate form of the distribution function.

Fig. 12 shows the fraction of free carriers n_e as a function of the pair density with Ry = 4 meV, and at T = 15 K. The exciton radius is 120 Å. As we can see from the figure, for low densities, the fraction of free carriers is dropping as the density is increased, but at a well-defined density it increases very rapidly till it reaches 1. The conclusion is that the we cannot expect the exciton density to grow indefinitely as we increase the pump power.

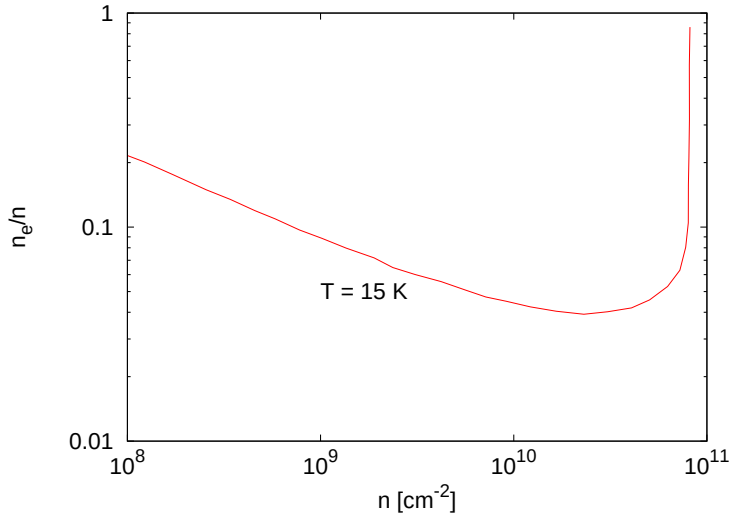

Figure 12: The fraction of free carriers as a function of the pair density for two-dimensional excitons. The temperature is 15 K. From [56].

2.0 DIFFUSION OF EXCITONS IN A PLANE

The motion of particles, and especially, the dependence of the characteristics of the motion on various experimental parameters, tells much about the relevant scattering processes. As such, diffusion measurements are fundamental in understanding how an ensemble of particles interacts with its environment.

Excitons move in semiconductors and semiconductor structures, transporting energy from one point to another. While it seems to be a trivial problem to measure the diffusion directly, the literature mentions mainly indirect measurements. Typical experiments with excitons in quantum wells do not observe motion of excitons over macroscopic distances, because the excitons have short lifetime due to close spatial wavefunction overlap and low diffusion constant due to disorder scattering. Over the years, researchers have come up with various ideas as to how to alleviate the difficulties associated with the small dimensions. Using high numerical aperture microscope objectives for tight-focus excitation and detection, Zhao et al. measured exciton diffusion of the order of several μm, over a time span of several hundred ps to a couple of ns [62, 63, 64, 65].

Hegarty et al. [66, 67], and Oberhauser et al. [68] used a transient grating method, in which a spatially modulated exciton population was created by two short laser pulses entering the sample at slightly different angles. This spatial modulation acted as a diffraction grating for a weak probe beam. As excitons begin to diffuse, the transient grating becomes washed out, thus monitoring the diffraction intensity as a function of time made it possible to deduce the diffusion coefficient.

Hillmer et al. [24, 69] used an opaque mask with two micrometer-sized holes to define the excitation and detection spots, and measured the time-of-flight of excitons to determine the diffusion coefficient. Similar measurements have been conducted by Heller et al. [70],

and Bacher et al. [71].

As we pointed out before, in coupled quantum well systems, the exciton lifetime, τ, can be as high as tens of μs as opposed to a couple of ns in a single quantum well; thus, taking a typical diffusion constant $D = 10$ cm^2/s, an average exciton moves $\langle r \rangle = \sqrt{D\tau} \approx 100$ μm from its place of creation. This is only the diffusion length, however, and if we reckon that the excitons strongly repel each other, excitons can easily move as far as a couple hundred μm. Thus, excitonic motion can no longer be regarded as a microscopic displacement, and the measurement of the diffusivity of the excitons and their effective mobility readily lend themselves to time-resolved optical imaging.

Electron and exciton transport properties in quantum wells have been the subject of a number of studies [72, 73]. In the next section we consider the scattering mechanisms relevant to exciton diffusion, and after that we discuss experiments which indicate that at low temperatures only one of them, interface roughness scattering, is important.

2.1 THEORETICAL PRELIMINARIES

Classically, diffusion is characterized by a diffusion constant, which is linked to the microscopic parameters through

$$D = \tau_{sc} \frac{k_B T}{m} \ , \tag{2.1}$$

where τ_{sc} is the relevant scattering time. Therefore, we have to identify the possible scattering processes. In semiconductors, each of these processes displays a specific dependence on several parameters.

Basu [74, 75, 76, 77, 78] calculated the scattering times for all relevant processes, assuming that the exciton wavefunction can be described by a variational ansatz as in Eq. (1.21), and using the various scattering potentials in Fermi's golden rule for the transition rates. As in Eq. (1.21), the variational parameter is denoted by α_{ij}, thus, depending on the particular dependence on α_{ij}, different exciton states will have different scattering times. However, at these low energies, we will only be concerned with indirect excitons with α_{11} in the notation

of Chapter 1. In all cases, the quantum well width is denoted by L, while the temperature by T.

Given the initial and final states, the transition rate can be obtained from Fermi's golden rule as

$$W(i,f) = \frac{2\pi}{\hbar}|\langle f|U|i\rangle|^2\delta(E_i - E_f) \ , \tag{2.2}$$

where U is the scattering potential.

As far as scattering is concerned, the exciton states are described by their in-plane center-of-mass momentum, which we denote by $\vec{K}$. (Here we implicitly assume that the inner structure of the particles does not change during the collision, i.e., the scattering energies are small compared to the binding energy.) This exciton state can be written as a superposition of those electron-hole pairs which differ by $\vec{K}$ in momentum [79], i.e.,

$$|\vec{K}\rangle = \sum_{\vec{k}} f(\vec{k}, \vec{k}-\vec{K}, \vec{K}) a^{\dagger}_{c,\vec{k}} a_{v,\vec{k}-\vec{K}}|vac\rangle \ . \tag{2.3}$$

Here $a^{\dagger}_{c,\vec{k}}$ creates an electron with wave vector $\vec{k}$ in the conduction band, while $a_{v,\vec{k}-\vec{K}}$ creates a hole with wave vector $\vec{k}-\vec{K}$ in the valence band. The prefactor $f(\vec{k}, \vec{k}-\vec{K}, \vec{K})$ is related to the real-space envelope function via its Fourier transform,

$$f(\vec{k}, \vec{k}-\vec{K}, \vec{K}) = \frac{1}{A}\int dxdy \int dz_e \int dz_h F(r, z_e, z_h) e^{i(\vec{K}m_e/M - \vec{k})\cdot\vec{r}} \ , \tag{2.4}$$

where $\vec{r}$ is the relative coordinate of the electron and the hole, A is the surface area, and $M = m_e + m_h$.

In principle, we could use the envelope function of a numerical solution. However, analytical results can be obtained if we assume that the confining potential is infinitely high, and the external electric field is zero, i.e., the electron and hole wavefunctions are simply sines and cosines. The electric field does not change the solution considerably. We restrict the discussion to the ground state of the exciton,

$$F(r, z_e, z_h) = Be^{-\alpha_{11}r/2}\cos\left(\frac{\pi z_e}{L}\right)\cos\left(\frac{\pi z_h}{L}\right) \ , \tag{2.5}$$

where B is a normalization constant, and r is the distance for the center of mass. Here we also neglect the relative motion of the electron and hole along the growth direction, z. From

now on, we simply take the various scattering potentials and calculate the matrix elements in Eq. (2.2).

The relevant scattering processes are listed as follows:

1. In the case of interface roughness scattering, fluctuations in the well width, $\Delta(\vec{r})$, lead to a local change of the electron and hole energies

$$\delta E(\vec{r}) = \frac{\partial E}{\partial L}\Delta(\vec{r}) = \frac{\partial}{\partial L}\Delta(\vec{r})\frac{\pi^2\hbar^2}{m_{e,h}L^2} = -\frac{\pi^2\hbar^2}{m_{e,h}L^3}\Delta(\vec{r}) \ , \tag{2.6}$$

which then acts as the scattering potential. Again, this expression is valid for infinite barrier height, and the character of the width dependence significantly changes for very thin quantum wells, where the confinement energy is comparable to the barrier potential [80]. The fluctuations are characterized by two quantities, their height, $\Delta(\vec{r})$, which we can expect to be on the order of one monolayer, and their lateral correlation length, λ, determined by the spatial correlation as

$$\langle\Delta(\vec{r})\Delta(\vec{r}')\rangle = \Delta^2 e^{-|\vec{r}-\vec{r}'|^2/\lambda^2} \ . \tag{2.7}$$

Although this correlation function does not have an established physical ground, it has the advantage that its Fourier transform can easily be calculated [81].
Since the growth process is the same from sample to sample, we can take λ to be constant. Then the matrix element in Eq. (2.2) becomes

$$|\langle\vec{K}'|\delta E(r)|\vec{K}\rangle|^2 = \frac{\alpha_{11}^6\hbar^4\pi^5\Delta^2\lambda^2}{L^6}\exp(-\lambda^2q^2/4)(\gamma_c/m_e - \gamma_v/m_h)^2 \ , \tag{2.8}$$

where $q = |\vec{K}| = |\vec{K}'|$, Θ is the angle between $\vec{K}$ and $\vec{K}'$, and

$$\gamma_{c,v} = (\alpha_{11}^2 + 4\alpha_{c,v}^2K^2\sin^2(\Theta/2))^{-3/2} \ , \tag{2.9}$$

The factor $1-\cos\Theta$ expresses the fact that the probability of back scattering is larger than that of forward scattering.
The total transition probability for $\vec{K}$ is obtained by summing over the final states, $\vec{K}'$, i.e.,

$$\frac{1}{\tau_{IR}} = \frac{\pi^2\hbar^4\lambda^2\Delta^2M\alpha_{11}^6}{2L^6}\int_0^{2\pi} d\Theta(1-\cos\Theta)e^{-\lambda^2q^2/4}(\gamma_c/m_e - \gamma_v/m_h)^2 \ . \tag{2.10}$$

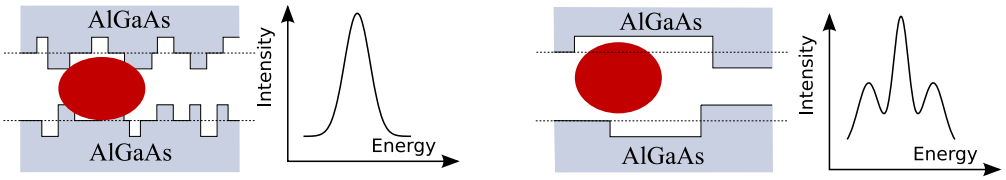

Figure 13: The extent of the wavefunction compared to the size of constant width islands in a single quantum well. Left hand side: the exciton samples many valleys. Right hand side: the exciton is located in one single island. Also shown are the corresponding schematic spectra.

This expression can be significantly simplified, if we use the parabolic dispersion relation, and take the limit $K \to 0$, in which case the scattering time reduces to

$$\frac{1}{\tau_{IR}} = \frac{\pi^5 \hbar^4 \Delta^2 \lambda^2 M}{L^6} \left(\frac{1}{m_e} - \frac{1}{m_h} \right)^2 \tag{2.11}$$

It is important to note that depending on the ratio of the correlation length and the exciton Bohr radius, the potential due to well-width fluctuations can present itself in two different ways.

If the correlation length is larger than the Bohr radius, separate exciton levels will form, as shown in Fig. 13. This usually happens if the growth process is interrupted for some time, and atoms on the surface reach thermal equilibrium by coagulating into separate islands [82, 83]. The signatures of the large correlation length can easily be tracked in the luminescence spectrum, for in this case the exciton energy changes from place to place, and in the spatially integrated spectrum several lines could be distinguished.

On the other hand, if the correlation length is smaller than the Bohr radius, then the exciton wavefunction "samples" all well-widths, and only one spectral peak will be present, inhomogeneously broadened by the well-width fluctuations. In all measurements we saw only one peak, therefore, we can assume that the correlation length is smaller than the Bohr radius. (See also Fig. 14.) This is also expected from the fact that the growth process was not interrupted when the samples were fabricated.

2. Scattering with impurities:

   The scattering potential is assumed to be spherically symmetric, to have a range of r_0 (which can be approximated as the lattice constant) and a strength of $\Delta U_{c,v}$ for the electrons and holes, respectively. Since the range is much smaller than the quantum well width, the potential can be assumed to be spherically symmetric. The scattering rate is then equal to [77]

$$\frac{1}{\tau_{IP}} = \frac{8\pi^2 N x(1-x) r_0^6 (m_e + m_h)}{3\hbar^2 L} \left(\Delta U_v - \Delta U_c\right)^2 \ , \tag{2.12}$$

   where N is the number of alloy sites per unit volume, x is the fractional alloy concentration, and m_e and m_h are the electron and hole masses, respectively. Impurity scattering is mainly relevant in InGaAs, AlGaAs, and doped GaAs samples [24, 77]. It still has a small contribution in pure GaAs, since the wavefunctions penetrate into the barriers, which are made of either AlGaAs or $Al_{0.7}Ga_{0.3}As$.

3. Acoustic phonon scattering:

   With the deformation potential, $D_{c,v}$, for the electrons and holes, the scattering potential is given as

$$U_{c,v}^{DP}(\vec{q}) = \sqrt{\frac{\hbar q}{2\varrho u V}} D_{c,v} \ , \tag{2.13}$$

   where ϱ is the mass density, V is the crystal volume and u is the sound velocity of transvers phonons, the scattering time is [74, 78]

$$\frac{1}{\tau_{DP}} = \frac{3\alpha_{11}^6 k_B T (m_e + m_h)}{4\pi\hbar^3 \varrho u^2 L} \int_0^{2\pi} d\Theta (1 - \cos\Theta)(D_c\gamma_c - D_c\gamma_v)^2 \ . \tag{2.14}$$

4. Piezoelectric phonon scattering:

   The interaction potential is

$$U_{c,v}^{PZ}(\vec{q}) = \frac{e}{\epsilon}\sqrt{\frac{\hbar}{2\varrho\omega V}} h_{c,v} \ , \tag{2.15}$$

   where $h_{c,v}$ is the piezoelectric constant for the conduction and valence bands, respectively. The scattering time becomes [74]

$$\frac{1}{\tau_{PZ}} = \frac{e^2}{\hbar(2\pi\epsilon)^2} \frac{k_B T}{\varrho u^2} \frac{4M\alpha_{11}^6}{L^2\hbar^2} I(q) \ , \tag{2.16}$$

where the factor $I(q)$ involves an integral on the $E = E(q)$ energy shell, but does not contain T or L dependence.

5. Longitudinal optical phonon scattering: The energy of the longitudinal optical phonon is around 35 meV, which is much higher than the exciton binding energy. Therefore, interacting with the phonon, the exciton either dissociates into an electron-hole pair, or evolves into an excited state, and carries away the remainder of the energy as kinetic energy. In this regard, this process does not contribute to exciton diffusion [84, 85].

2.2 EXPERIMENTAL

Having established the characteristic dependence of the various scattering processes on the external parameters, we now turn to the discussion of the experimental results on exciton motion in a plane landscape. In these experiments, an external bias was applied to the samples, and excitons were created by a pulsed laser, with a repetition period of 4 μs, which was chosen to be at least twice as long as the exciton lifetime, so that at the arrival of the next laser pulse, very few excitons were left over from the previous pulse.

Fig. 14 shows a composite of the time-integrated luminescence from the 100-Å well structure, for various voltages, recorded by projecting an image of the sample onto the entrance slit of an imaging spectrometer. These images show both the spatial and the spectral profile of the luminescence. As we discussed in Chapter 1, as the applied voltage is increased, the lifetime increases, and the excitons travel further.

In each of the images, there is a blue shift of the spectral position near the central excitation spot, which is the region of highest exciton density, and the spectral position falls as the density decreases far from the laser excitation spot. This shift comes from the repulsive interactions of the excitons, which lead to a mean-field energy shift. We will discuss this in great detail in Chapter 5. This strong repulsion of the excitons gives a strong pressure-driven expansion of the exciton gas immediately after the laser pulse.

We can also measure the time evolution of the exciton motion by imaging points located at various distances from the excitation spot. A typical set of such time-traces taken by a

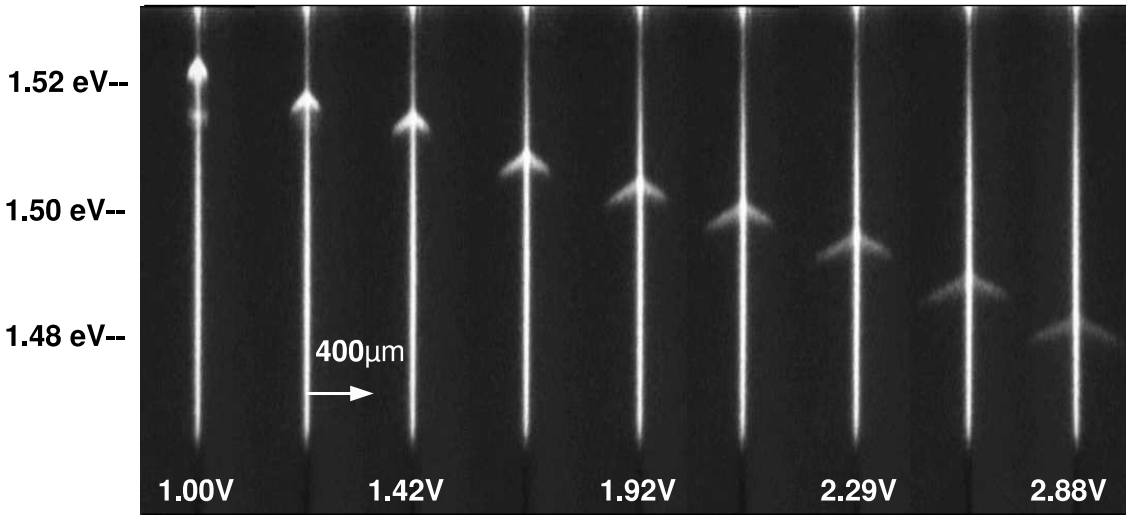

Figure 14: Composite of the time-integrated luminescence from the 100-Å well structure, recorded with an Oriel MS257^{TM} imaging spectrometer, for various applied voltages and with a laser excitation power of 2.7 mW. The narrow vertical line in the center of each image is impurity luminescence from the GaAs substrate, which is also excited by the laser. The chevron-like cloud spreading out from the central line shows the motion of the excitons away from the laser spot. The bright spots at the top of the images are emission from the direct excitons.

PMT is shown in Fig. 15. The rise time of the luminescence is longer for spots further away from the excitation spot, consistent with the picture that the excitons move out from the excitation spot without becoming localized.

We can quantitatively extract the diffusion constant of the excitons using the time-resolved luminescence. Fig. 16 shows a series of spatially and temporally resolved exciton emission profiles, which was produced by taking a set of time-traces similar to those in Fig. 15 and, at each time, ordering them according to their spatial positions. In this case the width of the wells was 100 Å. The data in the figure are fit to Gaussian distributions. The widths of these fits are then used to get an estimate for the diffusion coefficient.

As is well known, in the case of a purely diffusive process, the variance increases linearly with time; in particular, for a 2D, cylindrically symmetric system, the solution of the diffusion equation

$$\frac{\partial n}{\partial t} = \nabla(D\nabla n) - \frac{n}{\tau} \tag{2.17}$$

is

$$n(r,t) = \frac{n_0 t_0}{t_0 + t} \exp\left(-\frac{r^2}{4D(t_0+t)} - \frac{t}{\tau}\right) \ , \tag{2.18}$$

which implies that the variance is equal to $\sigma^2 = 2D(t_0 + t)$. Here we implicitely assumed that D does not depend on the spatial coordinate. In Eq. (2.17) we have also taken into account the radiative lifetime of excitons by including the decay term on the right hand side.

We therefore determine the diffusion constant by fitting a straight line to the plotted σ^2 versus time, at late times when the transport is diffusive; this slope is twice the diffusion constant D. In the equation above, $r^2 = x^2 + y^2$, $n(r,t)$ is the density of excitons, n_0 is the initial density at $r = 0$, and τ is the lifetime. t_0 specifies the width of the of the excitation, assumed to be Gaussian. Note that since the diffusion equation is linear in the density, the finite lifetime of excitons causes an overall drop in the intensity with increasing time, but has no effect on the variance of the Gaussian fit.

A typical plot of the time-dependence of the variance-squared for the 100-Å sample is shown in Fig. 17. Immediately after the laser pulse, the exciton cloud expands rapidly; then at late times, the behavior becomes linear. At very late times, when the exciton density has dropped considerably, the slope also decreases, due to localization. The initial interval can be explained if one takes into account that following the pulse the exciton density is very

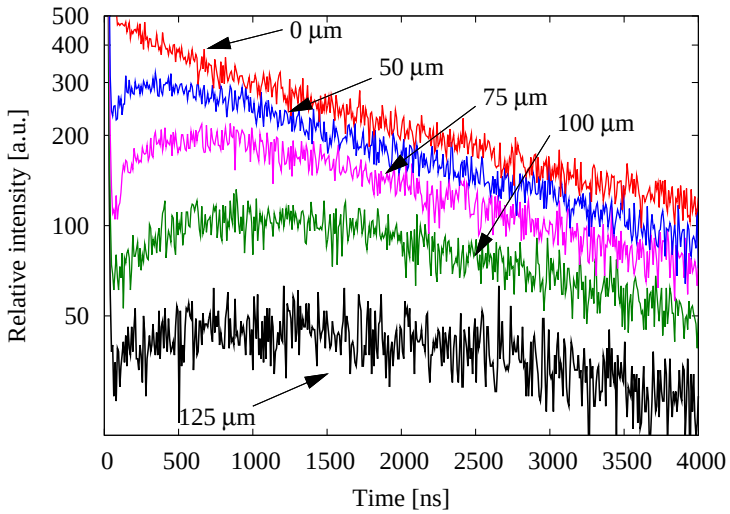

Figure 15: Indirect exciton luminescence intensity integrated over the wavelength range 821-825 nm, as a function of time for various points on the sample with 100 Å well width. The curves are labeled by the distance x in the plane from the central laser spot. The average excitation power, tuned to the indirect exciton resonance at 796 nm, was 30 μW and the repetition period 4 μs.

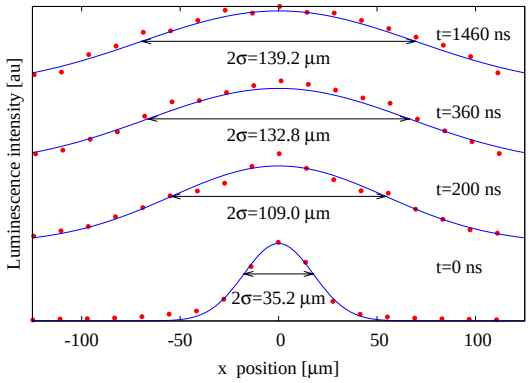

Figure 16: Expansion of the exciton cloud at different times after the excitation. In this particular case the well-width was 100 Å. The measured luminescence intensities are normalized. Also shown are the Gaussian fits with the value of the variance. The conditions are the same as in Fig. 15.

high. This results in a pressure due to dipole-dipole repulsion between aligned excitons. This pressure causes drift-like motion of the the excitons to move away from the excitation spot. A secondary effect of exciton density can be the filling up of local minima by excitons [86], which leads to a higher diffusion coefficient. At late times, after the density has dropped, pure exciton diffusion sets in and starts to dominate. We will return to the nature of the diffusion process in Chapter 8.

The time-dependence of the variance-squared for all four double well samples is shown in Fig. 18. Here we can clearly see that, though all other conditions are the same, the diffusive regimes have characteristically different slopes.

From the slopes in Fig. 18 we can determine the diffusion coefficients as discussed above. Fig. 19 shows the results for the four double well samples. The excitation density in all cases was kept low, in order to minimize the time in which the expansion of the exciton cloud is nondiffusive due to high dipole-dipole pressure. The applied electric fields (7, 5.8, 3 and 2.5 V/μm for the 80, 100, 120 and 140-Å quantum wells, respectively) were selected in such a way that the resulting lifetimes were comparable. As seen in this graph, there is an overall

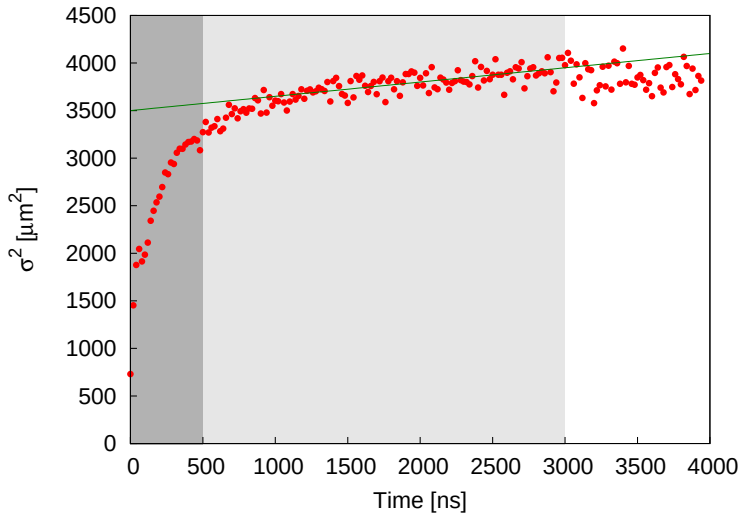

Figure 17: Measured variance-squared vs. time for the 100-Å sample, for average laser power 30 μW and pulse period 4 μs. The straight line represents a linear fit to the measured values in the range of 1000-3000 ns, i.e., when the expansions is purely diffusive. The shaded regimes are the strongly driven (dark grey), the purely diffusive (light grey) and localizing (white).

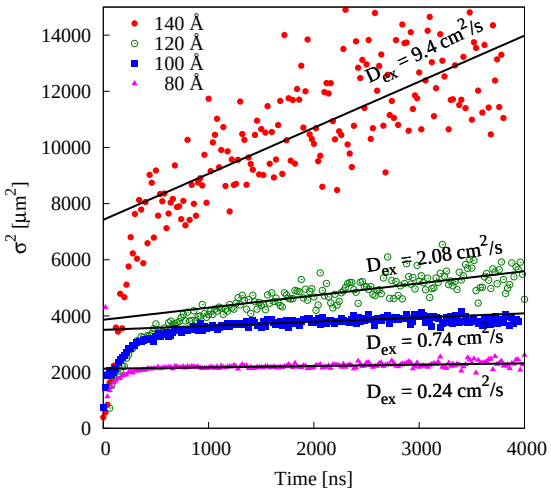

Figure 18: Measured variance-squared vs. time for the four samples, for average laser power 30 μW and pulse period 4 μs. The straight lines represent linear fits to the measured values in the range of 1000-3000 ns, i.e., when the expansions is purely diffusive.

increase in the diffusion coefficient as the well width is increased, consistent with a $D \sim L^6$ power law. This is in accordance with both previous measurements for electron transport [72], and the theoretical considerations outlined above.

From the measured diffusion coefficients, we can also determine the characteristic scattering time, τ_0. In two dimensions, the diffusion coefficient is $D = \bar{v^2}\tau_0$, where $\bar{v^2} = 2k_BT/m$. Hence,

$$\tau_0 = \frac{m_{ex}D}{2k_BT} \ , \tag{2.19}$$

which gives about 10 ps for the 120-Å quantum wells.

We have already pointed out that the exciton cloud does not expand indefinitely, as a simple diffusion process would require, but at very late times (or at very low densities) the excitons stop moving, and they appear to become localized, as indicated by the nearly-zero diffusion at late times in Fig. 17. This conclusion is also supported by Fig. 20, from Snoke et al. [87], where it was shown that the extent of the exciton cloud scales as the square root of the power. This is consistent with the picture that excitons move out of the excitation

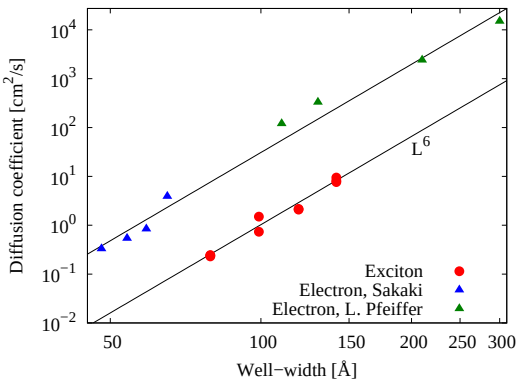

Figure 19: Measured diffusion coefficient as a function of well-width on a log-log plot, both for electrons [72, 88] and excitons. For comparison, also shown is the theoretical dependence, $D \sim L^6$.

spot, fill up the localization centers and stop.

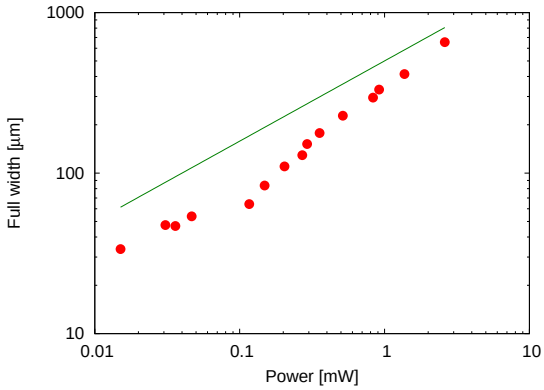

Figure 20: Power dependence of the size of the exciton cloud under continuous excitation by a laser tuned to the direct exciton resonance at 796 nm. The temperature is 1.6 K, the well-width is 100 Å.

3.0 TRAPPING COUPLED QUANTUM WELL EXCITONS BY STRESS

3.1 METHODS TO TRAP QW EXCITONS

As we pointed out in the introduction, trapping in two-dimensional systems is necessary for a BEC-type phase transition. In this section we discuss various methods of producing a macroscopic trap for quantum well excitons. We would like to mention, however, that in many cases there are already mesoscopic traps, simply because of the imperfection of the crystal. Several authors, e.g., Dremin et al. [36], and Yang et al. [89] used these mesoscopic traps to break the translational invariance of the system. The problem with these methods is that these traps are not reproducible and completely out of control as to their size or depth. Moreover, their small size leads to a large energy separation between consecutive levels in the trap, even comparable to the depth of the trap. In this case, however, one cannot talk about a well-defined phase transition. Also, repulsion between excitons washes out the trap at very low densities, as discussed below.

Up till now, five different methods have surfaced in the literature: electric field traps [44, 45, 90, 91], stress traps [93, 94], optical traps [95], magnetic traps [92], and traps produced by controlled well-width variations [96], which would rely on well-width dependence of the exciton energy as discussed in the introductory chapter. This last one appears to be a proposal only, and no experimental realizations have yet been demonstrated. Here we explain only the second method, and defer discussing the first one till the next chapter.

3.2 PIKUS-BIR POTENTIAL

The Hamiltonian of the hole states can be obtained by the method of invariants, after the crystal potential is expanded in terms of the stress [97, 98], and and for a zinc-blende crystal it takes the form

$$\begin{aligned} H_{PB} &= a(\epsilon_{xx}+\epsilon_{yy}+\epsilon_{zz}) + 3b\left[(J_x^2 - J^2/3)\epsilon_{xx} + (J_y^2 - J^2/3)\epsilon_{yy} + (J_z^2 - J^2/3)\epsilon_{zz}\right] \\ &+ \frac{6d}{\sqrt{3}}\left[\frac{\epsilon_{xy}}{2}(J_xJ_y + J_yJ_x) + \frac{\epsilon_{yz}}{2}(J_yJ_z + J_zJ_y) + \frac{\epsilon_{zx}}{2}(J_zJ_x + J_xJ_z)\right] , \end{aligned} \tag{3.1}$$

where J_x, J_y, J_z are the $J = 3/2$ angular momentum matrices. The coefficients a, b and d are the deformation potentials.

Taking the specific form of the angular momentum matrices, we arrive at

$$H_{PB} = a(\epsilon_{xx}+\epsilon_{yy}+\epsilon_{zz}) + \tag{3.2}$$

$$\frac{3}{2}\begin{pmatrix} b\epsilon_{sh} & 2d(\epsilon_{zx} - i\epsilon_{yz}) & \sqrt{3}b\epsilon_x^y - 2id\epsilon_{xy} & 0 \\ 2d(\epsilon_{zx} + i\epsilon_{yz}) & -b\epsilon_{sh} & 0 & \sqrt{3}b\epsilon_x^y - 2id\epsilon_{xy} \\ \sqrt{3}b\epsilon_x^y + 2id\epsilon_{xy} & 0 & -b\epsilon_{sh} & -2d(\epsilon_{zx} - i\epsilon_{yz}) \\ 0 & \sqrt{3}b\epsilon_x^y + 2id\epsilon_{xy} & -2d(\epsilon_{zx} + i\epsilon_{yz}) & b\epsilon_{sh} \end{pmatrix} \tag{3.3}$$

where $\epsilon_{sh} = 2\epsilon_{zz} - \epsilon_{yy} - \epsilon_{xx}$, and $\epsilon_x^y = \epsilon_{xx} - \epsilon_{yy}$.

We have to keep in mind, however, that this Hamiltonian acts on the quadruply degenerate (two light and two heavy holes) Γ_7 states of the valence band. Therefore, since the quantum confinement splits those four states into two doublets (the light holes and the heavy holes), we have to take the two lowest energy eigenvectors only.

The Hamiltonian above can be diagonalized, yielding the two eigenvalues

$$E = a(\epsilon_{xx}+\epsilon_{yy}+\epsilon_{zz}) - 3\sqrt{b^2(\epsilon_{xx}^2+\epsilon_{yy}^2+\epsilon_{zz}^2 - \epsilon_{xx}\epsilon_{yy} - \epsilon_{yy}\epsilon_{zz} - \epsilon_{xx}\epsilon_{zz}) + d^2(\epsilon_{xy}^2+\epsilon_{yz}^2+\epsilon_{zx}^2)} \tag{3.4}$$

for the heavy holes, and

$$E = a(\epsilon_{xx} + \epsilon_{yy} + \epsilon_{zz}) + 3\sqrt{b^2(\epsilon_{xx}^2 + \epsilon_{yy}^2 + \epsilon_{zz}^2 - \epsilon_{xx}\epsilon_{yy} - \epsilon_{yy}\epsilon_{zz} - \epsilon_{xx}\epsilon_{zz}) + d^2(\epsilon_{xy}^2 + \epsilon_{yz}^2 + \epsilon_{zx}^2)} \tag{3.5}$$

for the light holes. The hydrostatic term shifts both bands by the same amount, while the shear term splits them. (In our case, this splitting is an additional term, for the bands are already split by the quantum confinement.) The reason for this is that the hydrostatic stress does not change the symmetry of the crystal, therefore, all bands are affected in the same manner, while the shear stress modifies the symmetry.

In polariton experiments, it has recently been observed that the various heavy hole bands have different deformation potentials, namely, for the same stress, the first and second heavy hole polaritons shift by different amount [99].

The quantum confinement can be treated properly if we add E_{hh}^{cf} and E_{lh}^{cf} to the $|\pm 3/2\rangle$, $|\pm 1/2\rangle$ states in the diagonal in Eq. (3.4). However, since this perturbation is present only in the diagonal of the matrix, it simply splits the heavy hole and light hole states by $E_{lh}^{cf} - E_{hh}^{cf}$, but does not change the results in Eqs. (3.4),(3.5).

What is important in our case is that the energy of the heavy hole band depends on the *local* stress. Fig. 21 shows the setup to create the non-uniform stress distribution

Using the Hamiltonian in Eq. (3.1) or the eigenenergies in Eq. (3.4), we can determine the exciton energies, if we solve for the 6 independent elements of the stress tensor. We can obtain the strains by iteratively solving the wave equation in the steady state, i.e.,

$$\sum_{jlm} C_{ijlm} \frac{\partial \epsilon_{lm}}{\partial x_j} = \frac{1}{2} \sum_{jlm} C_{ijlm} \left(\frac{\partial^2 u_l}{\partial x_j \partial x_m} + \frac{\partial^2 u_m}{\partial x_j \partial x_l} \right) = 0 \ , \tag{3.6}$$

where C_{ijkl} are the components of the elastic tensor [100]. The cubic GaAs has a particularly simple tensor, with only 3 independent components [17],

$$C_{xxxx} = 1.2 \cdot 10^7 \mathrm{N/cm}^2, \quad C_{xxyy} = 5.5 \cdot 10^6 \mathrm{N/cm}^2, \quad C_{yzyz} = 6.0 \cdot 10^6 \mathrm{N/cm}^2 \ . \tag{3.7}$$

When solving for the stresses, we have to stipulate the appropriate boundary conditions. The experimental implementation is shown in Fig. 21, and it implies the following boundary conditions: the displacement is zero around a circle of diameter 2 mm on both the top and

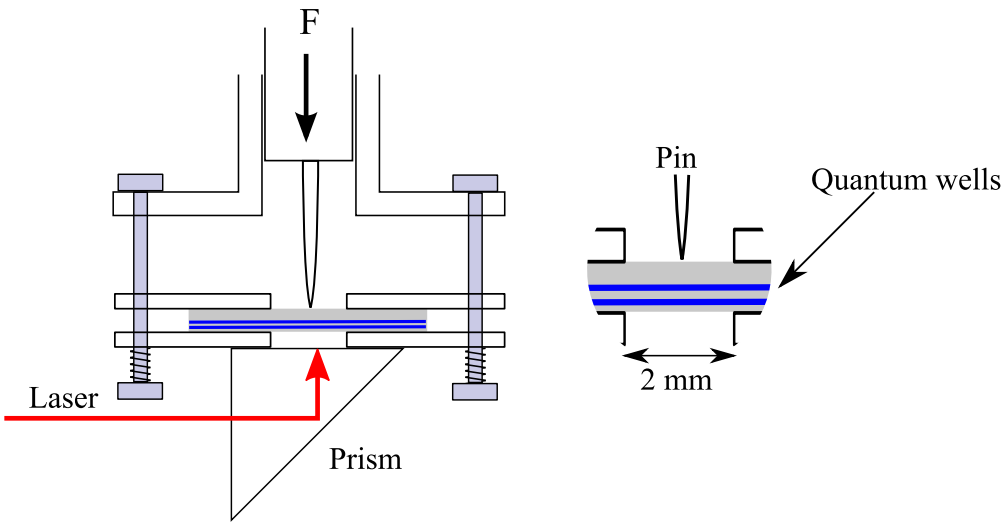

Figure 21: Configuration to create a non-uniform stress distribution. The sample is held between the two plates by the springs. The prism serves as a folding mirror in the setup.

the bottom of the sample, the bottom and top surfaces are free-standing, with the exception of the point where the force is applied. These can be written out as

$$0 = C_{44}\epsilon_{xz} \tag{3.8}$$

$$0 = C_{44}\epsilon_{yz} \tag{3.9}$$

$$F_z = C_{12}(\epsilon_{xx} + \epsilon_{yy}) + C_{11}\epsilon_{zz} \ , \tag{3.10}$$

where the force, F_z, is zero everywhere, except for the point where it is applied. Having specified the boundary conditions, we numerically solve for the stresses.

Fig. 22a shows the resulting hydrostatic stress and the corresponding energy landscape through the center of the trap in the plane of the quantum wells. In principle, the constants a, b and d could be calculated from the atomic wavefunctions, but instead of doing that, we take the experimentally measured values $a = -7$ eV, $b = 2$ eV and $d = 5.5$ eV [94, 101].

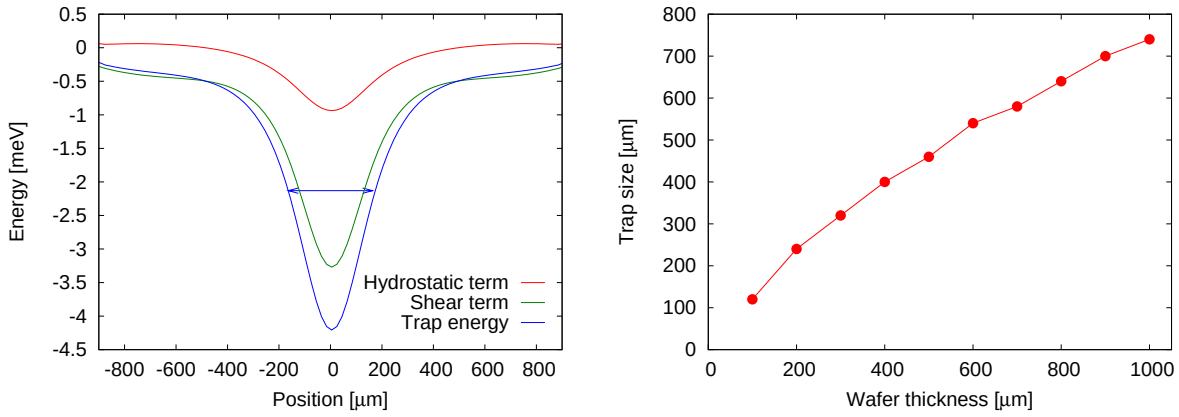

(a) (b)

Figure 22: Numerical results for the model discussed in the text. a) The non-uniform hydrostatic stress distribution and the corresponding trap energy in the heavy hole bands for a 300-μm thick wafer. The arrows show the definition of the trap size, full width at half maximum. After [94]. b) The size of the trap as a function of the wafer thickness, as determined from the model above. The size is defined as the full width at half maximum. After [93, 103].

Platero and Altarelli [102] cites values of $a = -6.7$ eV, $b = 1.7$ eV and $d = 4.5$ eV, which are still relatively close to those three numbers above.

Using the model above, we can also conclude that the size of the trap produced in this way scales nearly linearly with the thickness of the wafer, as shown in Fig. 22b. This observation was also confirmed in our experience: using a 150-μm thick wafer instead of a 300-μm wafer reduced the trap width by about a factor of two. We can understand this if we take into account that the bottom surface is stress-free, therefore, the force applied on the top surface must "heal" in a length scale given by thickness, and thus all spatial derivatives change accordingly. The experimental consequence is that in order to produce steep traps, we need to use as thin samples as possible.

We mention here that dynamic stress has previously been used for trapping excitons. In those cases, the elastic deformation is produced by standing or traveling acoustic waves, and the antinodes of the wave act as the potential minimum or maximum [104, 105, 106, 107, 108].

3.2.1 Experimental configuration

Fig. 21 shows the experimental configuration to create a non-uniform stress distribution in DQW systems. The wafer is clamped between two metal plates, both having a small (2 mm in diameter) hole in it. The sample is pressed from the substrate's side by a moveable sharp pin. Since the bottom surface (the side of the quantum wells) of the wafer is free, this force bends the wafer, creating a lateral expansion in it. The samples were mounted at room temperature, while the experiments were conducted at cryogenic temperatures. In order to avoid the creation of unwanted stresses due to the difference in the thermal contraction of the various materials involved, we always used spring mounts, as shown in the figure. The fact that without applied stress the exciton energies did not change from place to place proves that in this way we could avoid introducing stresses related to thermal contractions.

In Fig. 23 the resulting exciton trap can be seen. Also shown is a parabolic fit through the center of the trap, and the corresponding spring constant, $\alpha = 42$ eV/cm^2. This value of the spring constant was typical in these experiments. The parabolic approximation is valid over a range of ± 150 μm from the center.

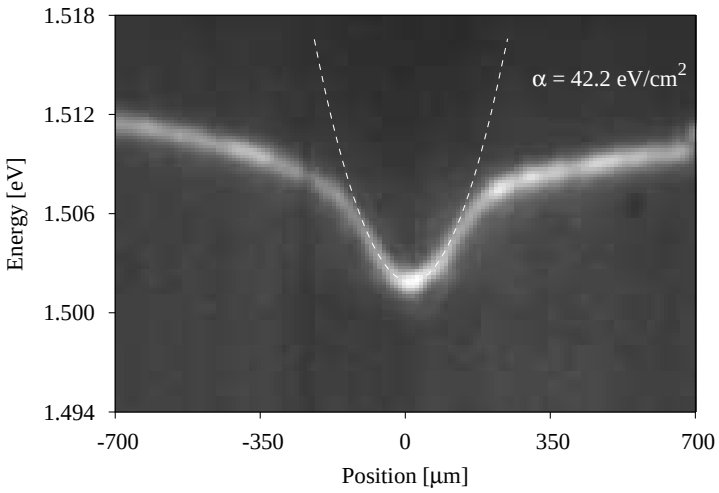

Figure 23: The potential trap created by the non-uniform stress distribution as measured by the spectral position of the indirect excitonic luminescence. The laser, tuned to the stress-free direct exciton resonance, was defocused and the excitation intensity was low, 1 mW continuous wave, so that the whole wafer was illuminated and the local density was low, thus the renormalization of the potential by exciton-exciton interaction can be neglected.

3.3 MEASURING THE TEMPERATURE OF EXCITONS

First, we describe experiments on measuring the exciton temperature directly, and we return to the problem of exciton-exciton interaction in Chapter 5. These measurements have fundamental importance, for in the literature, experimenters typically assume that the excitons reach the lattice temperature, but have no direct evidence for this [31]. In principle, the spectrum of the luminescence can be used, but this involves the assumption that the radiation probability is energy-independent in the relevant energy range [109, 125].

In this section we assume that we are far from quantum degeneracy, i.e., the exciton ensemble is described by the classical distribution

$$n(\vec{r},\vec{p}) = N_0 e^{-\beta(V(\vec{r})+\vec{p}^2/2m)} \ , \tag{3.11}$$

where $V(\vec{r})$ is the (possibly renormalized) trapping potential, and $\vec{p}$ is the center-of-mass momentum of the particles. In principle, we can deduce the temperature by measuring only in half of the phase space, i.e., integrate over either the momenta or the coordinate, and measure the particle distribution of $n(\vec{r})$ or $n(\vec{p})$.

This is common practice in atomic physics [2, 3], where measuring the exact shape of the trap is difficult, and it is better to measure the momentum distribution instead. This is done in a time-of-flight configuration: the trapping potential is switched off, and the absorption image of the ensemble is taken as a function of time. From the time evolution of the spatial distribution of the absorption strength the momentum distribution can then be reconstructed. It is important to point out that this measurement is destructive in the sense that for each snapshot a new ensemble has to be created under the exact same conditions, because by taking the image the distribution function of the system is altered.

In semiconductors with a strong phonon-assisted photon emission process (e.g., Cu_2O), it is possible to extract the temperature from the line shape of the phonon-assisted luminescence line, even without a trap [110, 111].

The presence of a well-controlled and measurable trapping potential makes it possible to measure the temperature of the ensemble through its spatial distribution function, or in other words, integrate over the momenta.

In our case, the luminescence intensity is proportional to the local exciton density. Taking the distribution function from Eq. (3.11) and integrating over the momenta, the measured intensity at position $\vec{r}$ is given by

$$I(\vec{r}) = I_0 \int_{[\vec{p}]} d\vec{p} e^{-\beta(p^2/2m)} e^{-\beta V(\vec{r})} = \tilde{I}_0 e^{-\beta V(\vec{r})} \int_{[\vec{p}]} d\vec{p} e^{-\beta(p^2/2m)} \ , \tag{3.12}$$

where we denoted the momentum component of the phase space of optically active excitons by $[\vec{p}]$. What is important here is that the momenta can be separated from the spatial variables. In equilibrium, one thus expects the cloud profile to be given by

$$n(r) = n_0(T) \exp\left[-\frac{\left(\frac{1}{2}\alpha r^2 + V[n(r)]\right)}{k_B T} \right], \tag{3.13}$$

where $\frac{1}{2}\alpha r^2$ is the harmonic approximation of the externally applied potential, and $V[n(r)]$ is the energy due to the exciton-exciton interaction. When the density is low, the term renormalizing the external potential will drop out, and the spatial profile will be a simple Gaussian, with width given by the temperature and the force constant of the harmonic potential. Equating the measured spatial distribution with Eq. (3.13), i.e.,

$$\exp\left[-\frac{r^2}{2\sigma^2} \right] = \exp\left[-\frac{1}{2}\frac{\alpha r^2}{k_B T} \right], \tag{3.14}$$

we arrive at a simple relationship between the size of the cloud and the temperature,

$$T_{\text{eff}} = \frac{\alpha \sigma^2}{k_B} \ , \tag{3.15}$$

where σ is the variance of the Gaussian profile which is the best fit.

As we did in Chapter 2, in the case of free diffusion, we can plot the size of the exciton cloud as a function of time. Fig. 24 shows the width of the spatial profile as a function of time for various temperatures and excitation powers. We also show a typical spatial profile long after the excitation in order to justify the Gaussian fits.

We can deduce a number of things from Fig. 24. First, initially the expansion is fast, as in the case of the plane diffusion, but then the restoring force of the trap starts to drive particles back towards the center. The expansion is faster for higher temperatures, in accord with the fact that in that case the diffusion coefficient is higher. Moreover, the expansion is

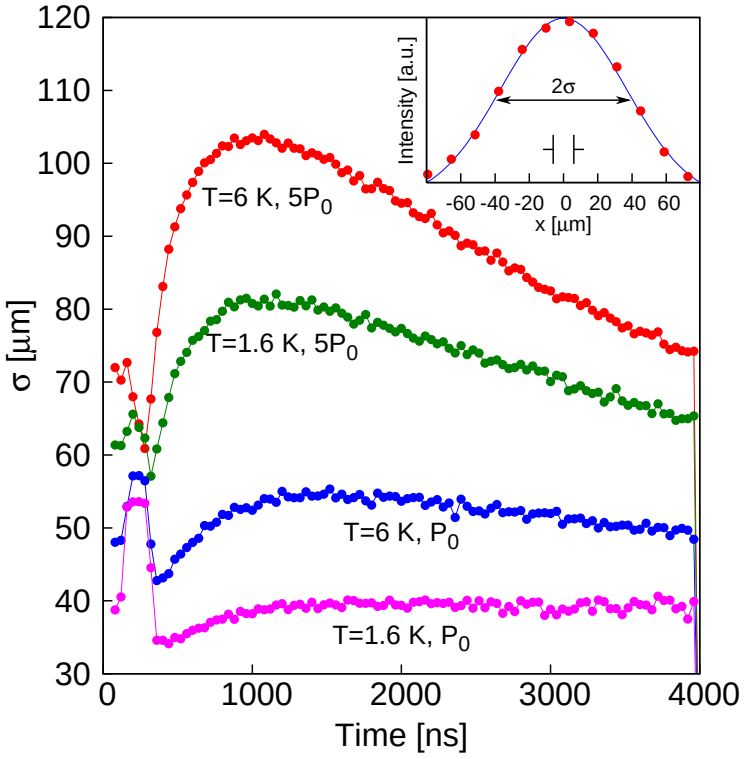

Figure 24: Time evolution of the spatial profile of the luminescence for $T = 1.6$ K and $T = 6$ K, and $P_0 = 100$ μW. The inset shows a typical profile long after the excitation. The inset also indicates the instrumental resolution. The 100-ns-long laser excitation takes place at $t = 200$ ns.

faster for higher excitation powers, in accord with the fact that in that case the number of excitons, and hence, the repulsive force exerted on them is larger.

We can use the measured σ to determine the effective temperature as we outlined in Eq. (3.15). This is shown in Fig. 25

As we have pointed out in Chapter 1, the radiative lifetime of the particles is proportional to the inverse of the temperature. This provides us with an additional tool to check for consistency. In Fig. 25 we also plotted the temperature deduced from time evolution of the total intensity. The time evolution of the number of particles in the trap obeys the differential equation

$$\frac{dN}{dt} = -A\frac{N}{T(t)} \ . \tag{3.16}$$

The factor A depends on the applied external field, as discussed in Chapter 1.

Initially, excitons possess some excess energy, due to the fact that the direct-indirect conversion brings particles to an energetically lower lying state, and some time is needed to emit phonons to release the energy difference. If we assume that the temperature decays exponentially as

$$T(t) = T_b + (T_0 - T_b)e^{-t/\tau_c} \ , \tag{3.17}$$

where T_b and T_0 are the bath and initial temperature, respectively, then the resulting differential equation becomes separable and can be integrated as

$$N(t) = N_0 \exp\left[-A\int_0^t \frac{dt'}{T_b + (T_0 - T_b)e^{-t'/\tau_c}}\right] \ . \tag{3.18}$$

This expression can then be used to fit the time evolution of the total intensity. In Fig. 25, the parameters are $T_b = 1.6$ K, $T_0 = 5$ K, and $\tau_c = 190$ ns.

The fact that the decay of the excitons at late times is single exponential as shown in Fig. 25, also confirms two claims. The first is that we see exciton decay, and not emission from an electron-hole plasma: in the latter case, in order to radiate, an electron must find a hole, therefore, the decay rate is proportional to the product of the electron and hole number, while in the first case, an electron is annihilated with its own hole, therefore, the radiation intensity is proportional to the number of particle pairs, i.e., excitons. The plasma-type recombination is relevant in luminescence ring experiments [112, 113, 114, 115, 116, 117].

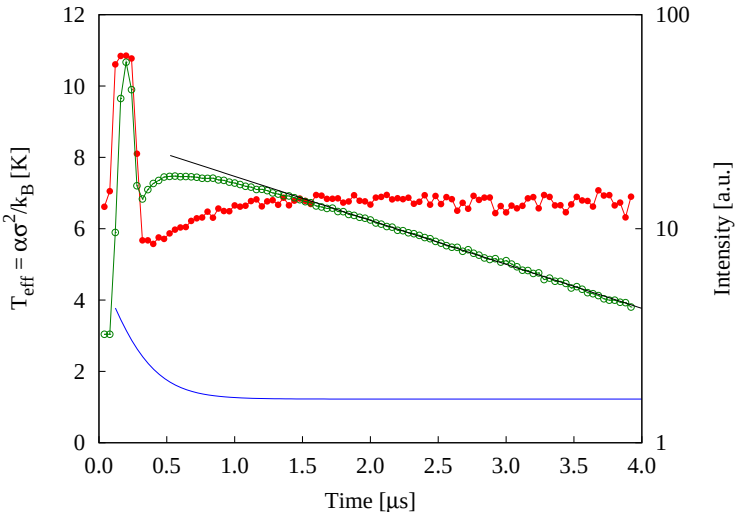

Figure 25: Red circles: width of the exciton cloud in the trap as a function of time, from Gaussian fits to the spatial profile at all times, given as an effective temperature as discussed in the text. The excitation power was 100 μW. Green circles: total luminescence intensity for the same data, integrated spatially and spectrally (right axis). Solid black line: a straight-line fit to the late time-intensity data. The data before 0.3 μs are obscured by bright substrate luminescence, during the 100-ns laser pulse. Blue line: the temperature of the exciton gas as a function of time, deduced from a fit to the intensity vs. time data and using Eq. (3.15).

Second, the single exponential decay also implies that there is no density-dependent Auger recombination as seen, e.g., for excitons in Cu_2O [118, 119, 120].

Naively, one would expect that the temperature of the exciton gas determined this way should equilibrate at the lattice temperature of 1.6 K. As seen in Fig. 25, however, at long times after the laser pulse, the excitons at low density reach a cloud size which stays constant in time, even as their density drops, indicating thermal equilibrium, but the effective temperature deduced from the cloud size is 6.6 K, not 1.6 K.

We note here that the solution Eq. (3.18) is still valid if we change the parameters as $T_b \to 6.6$ K, $T_0 \to 10$ K and $A \to 1.6A/6.6$. With the new parameters, Eq. (3.18) fits the measured intensity equally well.

One might guess that perhaps the excitons at these late times have a temperature well above 1.6 K, due to lack of thermalization. There are several arguments against this, however. First, although the lattice will be heated by the the laser pulse, the total energy deposited is so low, and the time constant for cooling so fast, that the increase of lattice temperature above 1.6 K is a few Kelvin at most. Because we used a 100 ns laser pulse, two-photon absorption is negligible. The excess energy per photon was 45 meV in the resonant excitation of the direct, single-quantum-well exciton. Knowing the heat capacity of GaAs, $C \approx 10^{-5}$ J/g/K [18], the laser light absorption length of approximately 1 μm [18, 19], and the excitation area of $(30\mu\text{m})^2$, for 100 μW average laser power, one can easily estimate the maximum temperature as 9 K. The excess heat quickly diffuses away from the 1 μm region of absorption. Taking $t = 100$ ns, the heat diffusion coefficient $D_h > 1000$ cm^2/s, the diffusion length is $\ell = \sqrt{D_h t} = 10^{-2}$ cm $= 100$ μm, which also means that the temperature maximum with respect to the background also drops a hundredfold, at least. Even if we take into account that at the He-GaAs interface only longitudinal phonons can propagate into the liquid, this could not cause more than a threefold increase in the cool-down time [121]. This conclusion can also be confirmed by the numerical solution for the heat diffusion, as shown in Fig. 26, where we applied the most conservative numbers for the heat diffusion coefficient, 1000 cm^2/s, and the heat capacity, 10^{-5} J/g/K.

Since the lattice itself cools down to the temperature of the He in a matter of a couple of ns, we have to look for other possible mechanisms for the discrepancy between the effective

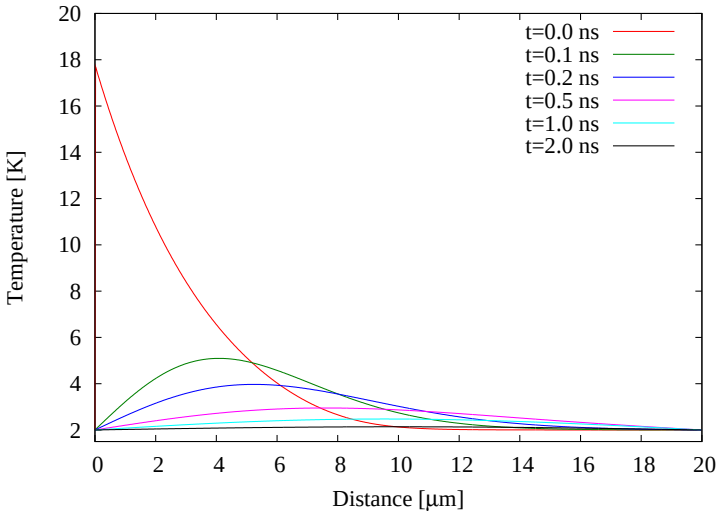

Figure 26: Time evolution of the temperature of the lattice after a laser excitation that would bring the temperature maximum to about 18 K. The distance is measured from the surface of the sample, i.e., the laser beam penetrates the wafer from the left.

exciton temperature and that of the background.

The time scale for thermalization of the exciton gas to the lattice, by phonon emission, is well known for excitons in quantum wells; recent calculations [86], which have been reproduced for our experimental conditions using the methods described in earlier work [122]. As seen in Fig. 27, the time to reach just a few percent higher than the lattice temperature is just a few nanoseconds. To reach temperatures below 1 K can take much longer, hundreds of nanoseconds [86], but still less than our many-microsecond lifetimes. These simulations are in agreement with the experimental result, shown in Fig. 25, that the lifetime of the excitons does not change after the first 500 nanoseconds or so [49].

It might be possible that the time to reach spatial equilibrium is simply much longer than what we can measure, thus we would deduce a false temperature from the cloud size. We can, however, estimate the timescale of spatial equilibration.

We know that the excitons are free to move in the trap at these temperatures because experiments without an externally-applied trap show diffusion of the excitons at these den-

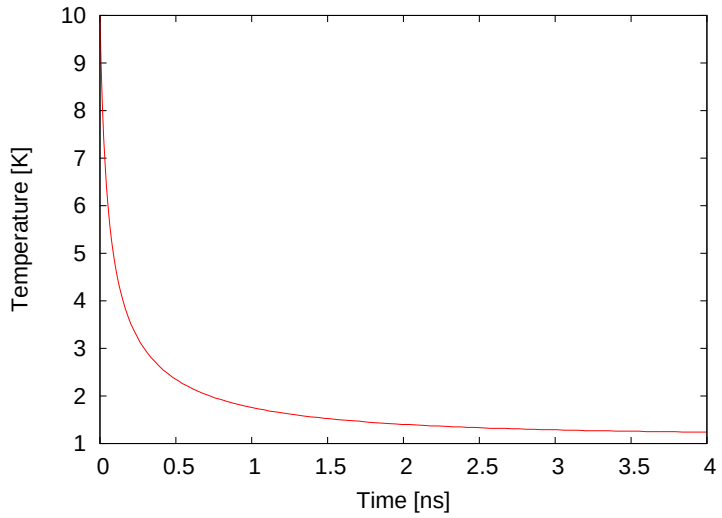

Figure 27: Time evolution of the temperature of excitons. The bath temperature is 1.2 K, and we assume an initial exciton temperature of 10 K. From [124].

sities and temperatures [123]. Solving the simple diffusion equation with the drift force of the trap, $\alpha\vec{r}$,

$$\frac{\partial n}{\partial t} = \nabla \cdot (D\vec{\nabla} n) + \frac{\tau_0}{m_x} \nabla \cdot (\alpha \vec{r} n) \ , \tag{3.19}$$

with the initial condition $n(r) = n_0 \exp(-r^2/2\sigma_i^2)$, yields the solution

$$n(r) = n_0 \frac{\exp\left(-\frac{r^2}{2(\sigma_f^2 - (\sigma_f^2 - \sigma_i^2)\exp(-\frac{2t\alpha\tau_0}{m}))} \right)}{2\pi(\sigma_f^2 - (\sigma_f^2 - \sigma_i^2)\exp(-\frac{2t\alpha\tau_0}{m}))} \ . \tag{3.20}$$

Hence, the characteristic time for the equilibration is

$$\tau = \frac{m}{2\alpha\tau_0} = \frac{k_B T}{2\alpha D} \ . \tag{3.21}$$

Substituting $\alpha = 40$ eV/cm^2, $D = 0.74$ cm^2/s and $T = 1.6K$ yields $\tau \approx 1.5$ μs, consistent with Fig. 25. Moreover, since we create the excitons in the center of the trap at $t = 0$, lack of equilibration in this case would give a false *low* temperature, not too high a temperature, because the cloud would be smaller than the equilibrium size.

The natural time scales of the system all indicate that the gas of excitons should be in equilibrium at the lattice temperature. We therefore must consider the possibility of a heat source. There are two possible sources. First, we must consider the possibility that leakage light from the laser heats the exciton ensemble. Although the excitons are created by a pulsed laser, a continuous wave (cw) component, even if it is small, acts as a continuous source of excitons with excess energy $\sim$ 40 meV, since the laser creates direct, single-quantum-well, excitons which must convert down into spatially indirect excitons in the double quantum well structure. In order to ascertain whether this is the case, we sent the laser light through an acousto-optic modulator (AOM) and repeated the measurements with different duty cycles, to allow different amounts of the cw light between the laser pulses to pass through to the sample. If leakage light between the pulses were responsible for the heating, then the two duty cycles would give different time evolutions of the cloud size. As Fig. 28 shows, there is no discernible difference between the two cases.

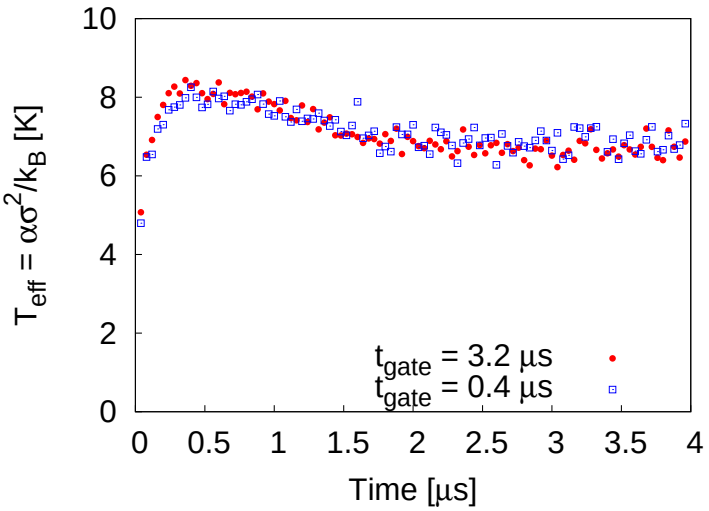

Figure 28: Time evolution of the cloud size expressed as the effective temperature for two different duty cycles of the AOM cell. Full red circles: 10%, blue open squares: 80%. The inset shows the actual band structure, and demonstrates how an electron tunnelling through the 500-Å barrier separating the superlattices from the quantum wells can have energies up to 400 meV with respect to the ground state of a quantum well exciton.

The other possibility is that current through the sample heats the excitons. The current density through the sample was on the order of 1 μA/cm^2. While this value seems to be rather low, we have to keep in mind that an electron that tunnels into the quantum wells comes with an excess energy of about 300-400 meV, as illustrated in the inset of Fig. 28. If these hot electrons can spend enough time in the quantum wells, then we cannot rule out the possibility that this leads to elevated temperatures. If we imagine a small population of hot carriers $n_{\rm hot}$ added to a cold population of thermalized excitons $n_{\rm cold}$, the new effective temperature will be approximately $(k_B T_{\rm hot} n_{\rm hot} + k_B T_{\rm cold} n_{\rm cold})/(n_{\rm hot} + n_{\rm cold})$. In the low density case of Fig. 29, we estimate that the cold exciton densities are a few times 10^9 cm^{-2}. If the tunneling current remains hot for 1 ns, then a current of 1 μA/cm^2 corresponds to a density in the quantum wells of about 10^4 cm^{-2}. For 400 meV excess energy per carrier, this is marginally enough to raise the cold exciton temperature by a few tenths of a degree. This is a very approximate estimate, however, and therefore we cannot rule out that current plays a role in heating the exciton gas.

We note that if current does play a role in heating the excitons, its effect will be much less at higher excitation densities, since the tunneling current is roughly constant, and therefore the ratio of these hot carriers to the total population will decrease and become negligible when the generated exciton density is higher, in the range 10^{10} cm^{-2}.

Third, it might be possible that excitons, initially pushed high in the trap by the strong exciton-exciton interaction, become localized when their density drops below a certain threshold value. This would also be consistent with Fig. 17. In any case, it seems that one cannot simply assume that the exciton temperature, defined by the spatial equilibrium of particles, is equal to the lattice temperature below 5 Kelvin. We point out, that on a much shorter time scale (13 ns), based on the spectrum of the luminescence, Gorbunov et al. [125] also measured an exciton temperature higher (around 5 Kelvin) than that of the lattice (2 Kelvin). While in their case, the temperature seemed to converge to 5 K, due to the high repetition rate of their laser, it is not clear whether the excitons would cool down to 2 Kelvin given long enough time, or this is indeed their final temperature.

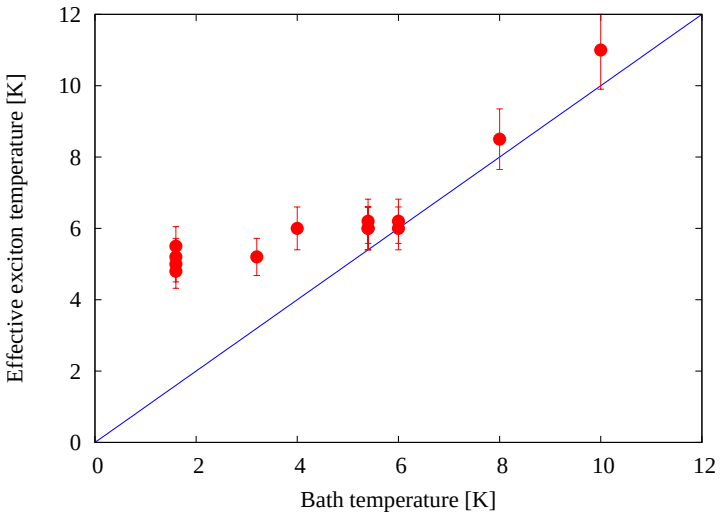

Figure 29: Measured effective temperature as a function of bath temperature. The solid straight line is the bath temperature. The errors are estimated from the uncertainty in determining the spring constant of the trapping potential. The instrumental resolution given in the inset of Fig. 24 was deconvolved assuming simple quadrature.

4.0 ELECTRIC FIELD TRAPS FOR EXCITONS

In Chapter 1, we pointed out that the energy of indirect excitons depends on the magnitude of the electric field, and in particular, the energy minimum is located at points of high field. This means that if an electric field has an in-plane maximum, excitons can be expected to accumulate there and become trapped. This is counter-intuitive to some extent, for excitons are charge-neutral particles, therefore, they do not react to an electric field. However, what plays a role here is not the field itself, but its variation in space, the gradient.

We also pointed out, that as the electric field increases, so does the lifetime, which means that in such a trap excitons do not have a single lifetime, but live long at the low-energy points, and annihilate more quickly at the high-energy points. This is analogous to evaporative cooling in atomic condensates: the high-energy particles are removed from the system through recombination. On the other hand, due to this anisotropy in the lifetime, the analysis and interpretation of experimental data is more difficult.

4.1 TRAPPING CONFIGURATIONS

Contrary to the stress trapping method, which is quite unique and in this form is used only in our group, electrostatic traps are very popular, and many configurations have been developed over the years. In all cases, the inhomogeneous electric field is produced by a flat conducting surface on one side of the coupled quantum wells, and a gate on the other side, held at a potential different from that of the flat surface.

In the simplest case, the gate can be a single tip, as in Gorbunov and Timofeev [45, 126]. In this case, the front side of the sample was conducting, while the back side was insulating.

A small AFM tip at the back side was then held at a potential higher than the front side. The inhomogeneous electric field between the tip and the front side produces a V-shaped exciton potential with a size determined by the thickness of the sample and the size of the tip. The same group used traps created by the electric field around the edge of a circular and a metallic aperture. This configuration has the advantage that the field of view is clear, but on the other hand, the potential minimum is not at the center of the trap.

Hammack et al. [44] produced a transparent gate structure with a set of concentric circles on the front side of the sample, as shown in Fig. 30(c). The potential of the circles could individually be set. This means that by changing the relative voltages on the circles, various trap-shapes could be realized. The trap size in these experiments was in the order of a couple μm. Zimmermann et al. used the same principle, with the exception that the gates on the front side were arranged in a configuration of two interleaving combs [128, 129].

High et al. [15] took this approach one step further by dynamically modulating the trap: by pulling one of the electrodes to a potential lower than its vicinity, they created a barrier which could be switched on or off. In the presence of the barrier, excitons are prevented from flowing from one place to another. This produces an "excitonic transistor" where the control signal is electronic.

Gärtner et al. [42] used the resistance of the front side gate to produce the gradient: holding the two ends of the front side gate at different voltages, a potential gradient is produced, in which excitons created on the high energy (low potential) side roll down. Fig. 30(d). In this case, one of the technical limitations is the maximum current that the front side gate can support: the potential difference between the two ends cannot be raised indefinitely, because the induced current would heat the sample, amongst other things.

The same group has successfully used a field-effect structure, which was produced by sandwiching a SiO_2 layer between the surface of the GaAs heterostructure and a semitransparent metallic top gate [43]. They showed that excitons were trapped at the perimeter of the structure, and explained the trapping mechanism by a combination of the quantum confined Stark effect and local field enhancement. In this case, however, the trap was one-dimensional, in the sense that in one direction possessed a spring constant of about 10 keV/cm^2, while in the other it was flat.

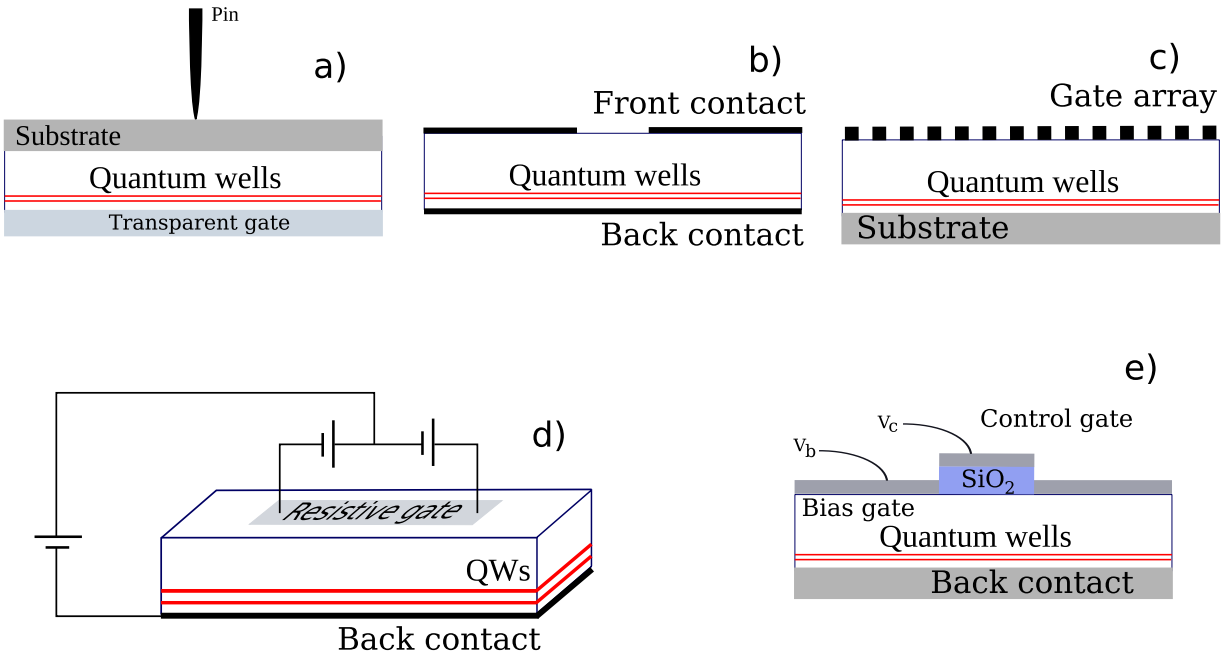

Figure 30: Various electric field trapping scenarios. a) Trap by Gorbunov et al. [45]. b) Trap by Gorbunov et al. [125]. c) Trap by Hammack et al. [44]. d) Trap by Gärtner et al. [42]. e) Trap by Gärtner et al. [43].

4.2 LIMITATIONS OF ELECTRIC TRAPS

At first, it seems that electric field traps could be very flexible, both in terms of their shapes and their depths, for the shapes can relatively easily be reconfigured by applying different gate configurations, and the depth (and consequently, the apparent spring constant) can be as high as desired. First, even with the most careful design of the sample, a small leakage current will always be present. This current increases very rapidly as the bias potential is increased.

More importantly, however, the in-plane component of the electric field pulls the electrons and holes in opposite directions, which, in turn, leads to the ionization of excitons [127, 128]. In a couple of papers, Rapaport et al. [90, 130] pointed out that ionization poses a severe limitation on the applicability of deep electrostatic traps.

The maximum density of excitons that a trap can support is determined by the repulsion between the particles and the depth of the trap. Treating the repulsion in the mean-field approximation, the energy shift due to exciton-exciton repulsion is

$$\Delta E = \gamma n_{ex} \ , \tag{4.1}$$

where γ is a constant, which can be measured or derived from first principles. (We will return to this point in Chapter 5.) Therefore, in order to facilitate more particles, and beat their repulsion, the depth trap must be increased. On the other hand, the increase in the required electric field ionizes the particles, thus reducing the trap lifetime. The lifetime as a function of the exciton density is shown in Fig. 31a. The density was deduced from the depth of the trap and the value of $\gamma = 1.5 \cdot 10^{-10}$ meV cm^2, which is a typical value for a 100-Å double quantum well [9, 90]. The three aspect ratios are given by the distance between the substrate and the quantum wells divided by the distance between the substrate and the capping layer, as in Fig. 31b.

From Fig. 31a, we can see that as the density is increased, the trap lifetime drops very rapidly, almost exponentially. At a density of about $3 \cdot 10^{10}$ cm^{-2}, even in the best trap ($z/l = 0.2$) the lifetime is less than 1 μs. Based on the measurements in Chapter 3, excitons

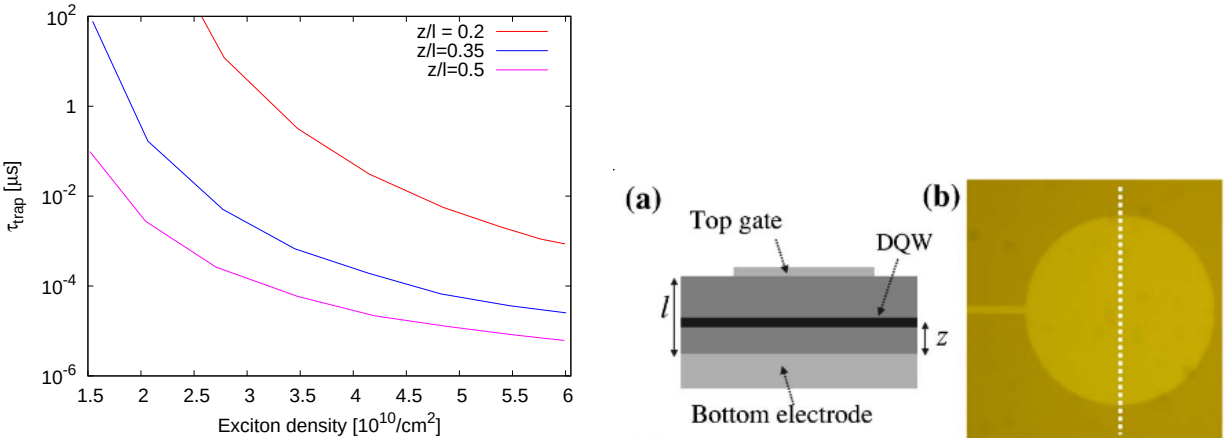

Figure 31: Left hand side: Theoretical prediction for the lifetime of excitons as a function of the exciton density for three different aspect ratios of the trap. After [130]. Right hand side: The schematics of the trap used in the experiments (a), and the microscope image of the front side gate with a diameter of 50 μm. The small wire is for biasing the gate, and has a width of about 2 μm.

need about this much time to come to equilibrium, which means that an equilibrium gas with a density higher than $3 \cdot 10^{10}$ cm^{-2} is not feasible in these kinds of traps.

4.3 BACK-SIDE BIASSED TRAPS

From the optical point of view, applying a trap from the back side of the sample seems simpler, for in this case the field of view is not obstructed. We, therefore, tried this method first.

In order to produce a reasonably sized trap (less than a hundred μm in diameter), two requirements must be fulfilled. The first is that the pin be this large at most, and the second is that the pin be very close (some tens of μm) to the front side (the location of the quantum wells) of the sample. This also means that the wafer must be either very thin, or an appropriate hole must be "drilled" to accommodate the pin.

Our first attempt was to etch the pin into the wafer, i.e., to etch a very long and narrow hole, and metalize its surface. We used a plasma ion etcher at Cornell University's Nanofabrication Facility, which also means that various preparation steps needed to be completed, such as, coating the wafer with photoresist, baking it, placing a Cr mask on it, lifting off the uncovered photoresist and loading it into a etching chamber. Given the temperature range of these steps, and the difficulties in the handling of the sample, this also implies that only relatively thick (~ 200 μm) and rigid wafers could be used. In turn, this means that the hole had to be deep and have a large aspect ratio. As it turned out, the depth posed the most serious difficulty, for at least, two reasons. One is that etching takes a long time, during which the mask needs to remain resistive. A 2-μm thick Cr mask with a 200-μm hole could withstand the etching process for about 40-60 minutes, during which the the hole reached a depth of about 15 μm. The thickness of the mask cannot be increased indefinitely, because the strain that builds up between the bottom and the top surface during the evaporation peels off the Cr layer, if its thickness is beyond some threshold value. The 2 μm value quoted above is about the largest thickness that we could grow without peel-off.

Since we could not succeed with the Cr mask, we tried to create a very rudimentary

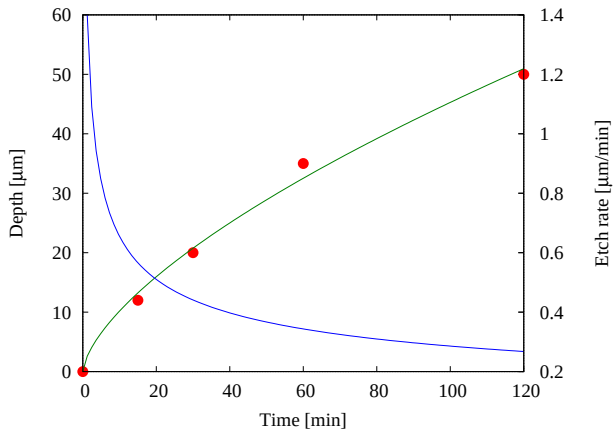

Figure 32: The depth of the hole as a function of time, left axis, solid circles. The solid green line is a $\sim \sqrt{t}$ dependence. Also shown is the deduced etching rate (blue curve) on the right axis. The mask had a 1.5-mm diameter hole on it.

mask by attaching a stainless steel washer with a small hole on it to the sample. Even with this, the etching speed becomes prohibitively low at larger depths, as shown in Fig. 32. With the original Cr mask with the 200-μm hole, in the same amount of time, we could etch a 15-20 μm deep hole. From these results, it became clear that a completely different approach should be taken for any chance of success.

In addition to the low speed, the profile of the cavity was far from satisfactory, as can be seen in Fig. 33. The irregularities and bumps grew larger and larger as time wore on, and we could not produce a hole with smooth bottom. Therefore, we have concluded that this method is not suitable for producing the an electrostatic trap.

4.3.1 Thin-wafer samples

Our second attempt was to use a very thin wafer, with all the difficulties associated with handling. However, it turned out that this task is not impossible, and we could etch, handle and mount a wafer of thickness between 5 and 10 μm. The wafer was then placed on an indium-tin-oxide coated glass, which served as one of the electrodes, and was biased by a

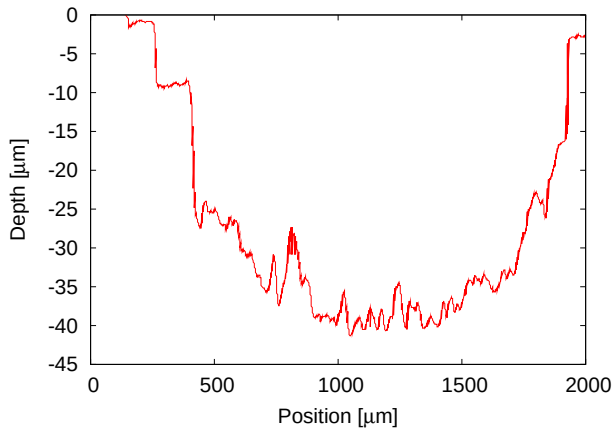

Figure 33: Profile of the hole produced by reactive plasma etching with a stainless steel mask. The etching time was 60 minutes. The profile was taken with a mechanical profiler of tip size 40 μm, which also determines the spatial resolution.

small, electrolytically etched pin from the back side. The diameter of the pin was around 15 μm. Fig. 34 shows the outline of the trap when a small bias potential is applied between the front side and the pin.

This method also had problems: since the preparation takes place at room temperature, while the experiments are done at He temperatures, the samples cannot be glued to the glass plate, it can only rest on it. However, these very thin wafers tend to bend and lose contact with the glass. Also, the very small force exerted by the pin when touching the sample was enough to break it.

Thus, although we could demonstrate a proof of principle, and show that an electrostatic trap can be created in this way, we did not conduct more measurements with this configuration.

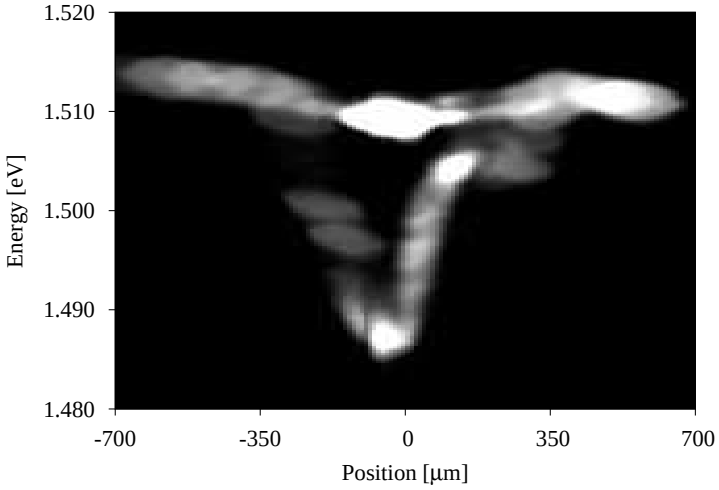

Figure 34: Outline of a trap produced on a thin-wafer sample, in a configuration similar to that in Fig. 30 a). The laser was scanned through the center of the trap while the integration took place.

4.4 FRONT-SIDE BIASED TRAPS

In collaboration with Gang Chen and Ronen Rapaport of Bell Labs, we conducted experiments on an electrostatic trap which was patterned on the front side, as shown in Fig. 31b. A semitransparent TiO disc-shaped gate was used to produce a cylindrical trap of size $20 - 80$ μm in diameter with a flat bottom. This geometry has the advantage that since the field is constant almost throughout the trap, ionization takes place only at the edges. However, the ionization is strong at the edges, thus leading to a "leaky" trap [46, 90, 131].

Since the trap size was rather small (30-80 μm), and close to the spatial resolution of our imaging system ($\sim$ 13 μm), in order to verify trapping, we measured the shift of the spectral peak of the luminescence as a function of continuous pumping power. This is shown in Fig. 35. For comparison, we also show the exciton density when the sample is biassed uniformly, i.e., when no trapping potential is present. The exciton density is determined from the shift divided by γ, as in Eq. (4.1).

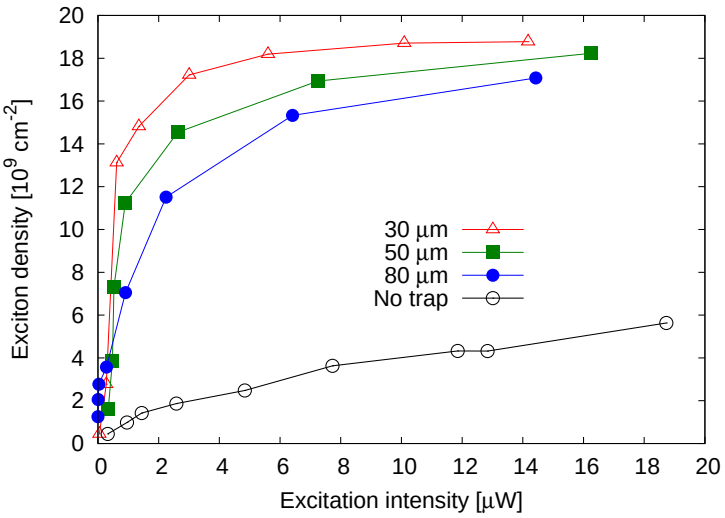

Figure 35: The exciton density as a function of the pump power for three different trap sizes, and the flat potential. The temperature was 2 K. From [90].

There are two things that we can conclude from this figure. First, the traps indeed confine the exciton gas, because the density achieved is higher in all three traps than in the trapless case. Second, for the smaller trap the confinement is stronger, because for the same excitation power, the exciton density is higher in a smaller trap.

The dynamics of the exciton gas can be measured in the same way as in Chapters 2 and 3, i.e., by time-resolving the luminescence at various points on the sample. Fig. 36 shows the spatial distribution of excitons in an 80-μm trap for three different times after a 2-ps excitation. The trap was biased at 6 V, which resulted in a trap of about 30 meV in depth. As in the case of the stress trap, excitons move away from the excitation spot very quickly, and after about 500 ns, the distribution is flat, indicating that equilibrium has been achieved. We note that this time for the equilibration is of the same order of magnitude as in the stress traps.

Thermal equilibrium after the first 500 ns is also supported by the time evolution of the spectrally integrated intensity at the center of the trap, as shown in Fig. 37. Initially, the intensity drops very fast, because excitons move away from the center. Later, however, when

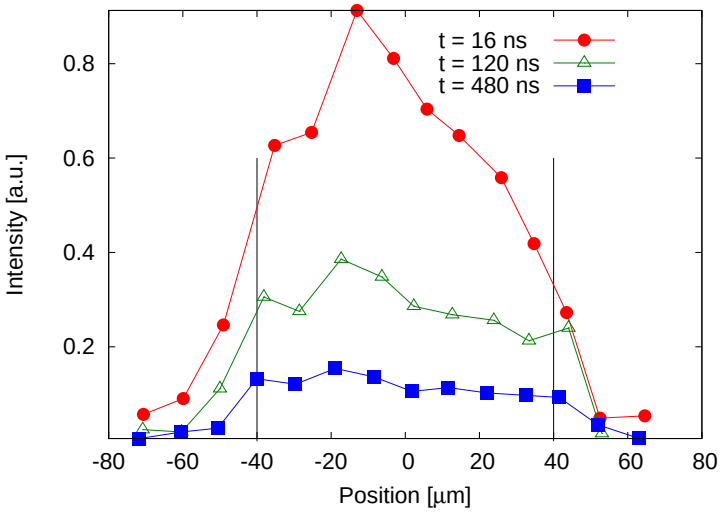

Figure 36: The exciton density as a function of spatial position for three different times. The vertical lines indicate the boundaries of the trap. The temperature was 2 K. From [90].

the intensity distribution is flat,the time trace becomes single exponential. As we discussed in Chapter 1, this indicates that the exciton gas has a well-defined temperature. Also, the lifetime that we can deduce from this plot is comparable to the lifetime of a uniformly biassed sample at the same potential, which indicates that particles do not leak out of the trap at the boundaries and the exciton ionization is not too significant.

Cheng and Rapaport also demonstrated the possibility of dynamic modulation of this trap at a frequency of about 100 kHz: changing the bias voltage moves excitons spectrally, at the same time, reduces their lifetime. Thus, particles can be removed from the trap at will [131]. The same idea has been utilized in "exciton-transistors" in the work High et al. [15]. The maximum of the modulation speed is determined by the capacitance and resistance of the sample, and is not related to excitonic properties, and with proper design, it can be increased significantly.

These results show that electric means can indeed be used to trap excitons and confine them in a small area for times up to a couple of μs. In fact, the depth of these traps is comparable to or even exceeds that of the stress traps. However, since exciton ionization

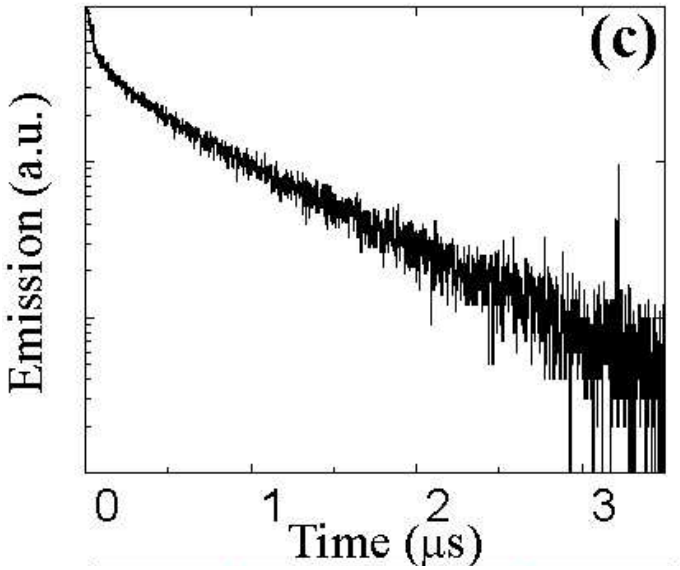

Figure 37: Time evolution of the spectrally integrated intensity at the center of the trap. The temperature was 2 K. From [90].

due to the in-plane component of the electric field reduces the exciton lifetime, these traps have a severe limitation. This might be the reason why we have not observed signatures of quantum degeneracy in such traps.

5.0 THE ROLE OF INTERACTION

5.1 REPULSIVE INTERACTION BETWEEN EXCITONS

The description of exciton-exciton interaction is a long-standing theoretical problem, and based on the literature, it still seems far from being settled [9, 140, 141, 142, 143]. This is mainly due to the fact that the bosonic commutation relation is not strictly obeyed, and various approximations must be implemented in order to render the problem tractable. In the case of atoms, the nuclei can be treated as infinitely heavy compared to the electrons, and nucleus exchange can be neglected. For excitons, the picture is completely different: the constituents, the electrons and holes, have comparable masses, and exchange must be taken into account not only between electrons-electrons and holes-holes, but in a complete model, even between electrons and holes.

From the experimental point of view, the calibration of the absolute exciton density is a difficult problem: not only have we got to know the electron-hole creation accurately, but also the rate of formation of excitons, and in the case of coupled quantum well excitons, even the conversion rate from the direct to the indirect state. Estimates for all these processes carry a large margin of error. In the literature, there have been attempts to calibrate the absolute exciton density by measuring the transition rates of various excitonic levels. This method, however, also has its limitations. First, the energy difference between two exciton levels is, at least, in the case of GaAs quantum well excitons, of the order of a couple of meV, which implies that THz techniques must be applied. Second, in order for this method to reliably work, these excitonic levels must be well separated from each other, other absorbing states, and their environment, which is not a trivial requirement [144].

On the other hand, being able to trap excitons in a harmonic potential also means that

we have a way of studying their interactions under controlled conditions, since the exciton-exciton interactions determine the spectral energy shifts of their luminescence. The physical origin of the repulsive interaction comes from two sources, the Coulomb interaction between the constituents and phase-space filling. As for the latter one, as the density is increased, and the interparticle spacing becomes comparable to the Bohr radius, the fermionic structure of excitons can no longer be neglected. To the Coulomb interaction, an intuitive, though somewhat inaccurate meaning can be attached. We have seen in Chapter 1 that indirect excitons are dipoles aligned along the growth direction, with electrons and holes residing in different quantum wells. In the mean-field approximation, this repulsion results in an energy shift which is proportional to the exciton density,

$$\Delta E = \gamma n_{\rm ex} = \frac{4\pi e d}{\epsilon} n_{\rm ex} \ , \tag{5.1}$$

where d is the dipole moment of the exciton, and can be taken as the distance between the centers of the two quantum wells multiplied by the electric charge [9]. This is sometimes referred to as the *capacitor formula* [86, 96, 131], because as excitons become aligned under the influence of the external electric field, the relative position of electrons and holes tends to cancel the external field, and this cancellation is proportional to the number of charges accumulated in the two quantum wells, just as it would happen in a parallel-plate capacitor, as shown in Fig. 38.

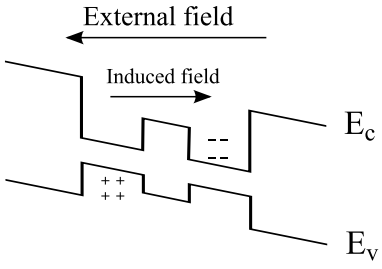

Figure 38: The cancellation of the external electric field due to the presence of aligned dipoles.

On one hand, the presence of repulsive interaction prevents the formation of biexcitons, which, at least, when searching for BEC, would be a limiting factor. Molecule formation, which is the analogue of biexciton formation, is a known problem in hydrogenic BEC experiments, where it is overcome by polarizing the spin of H atoms: two H atoms with the same spin cannot lower their energy by forming a molecule [132]. On the other hand, however, this repulsion is not always advantageous, since it reduces the strength of the trapping potential. Fig. 39 shows the profile of the trap as the excitation intensity is turned up. The laser was defocused, so that the whole trap was illuminated. As seen in this figure, the trap becomes shallower as the density increases.

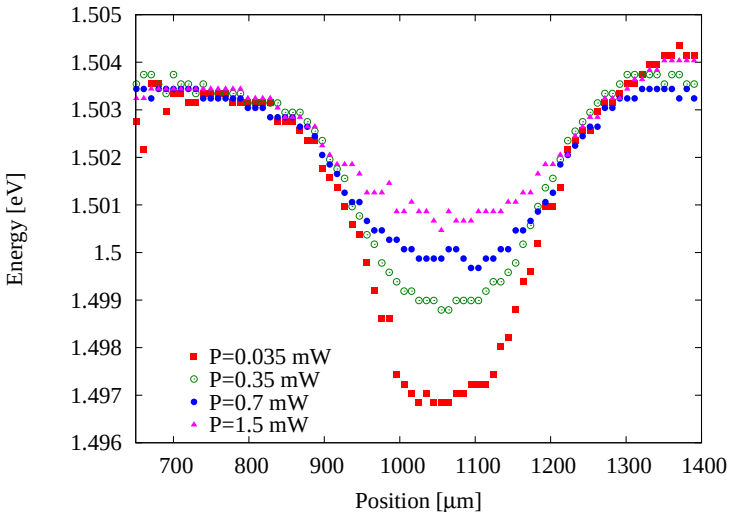

Figure 39: Renormalization of the trapping potential in a 100-Å double quantum well due to exciton-exciton repulsion: the trap is flattened as the number of excitons is increased. In this case, a defocused, continuous wave diode laser tuned to the stress-free single exciton resonance at 796 nm was used to excite the sample.

In this chapter first we discuss experiments that we conducted in order to gain some insight into the nature of exciton-exciton interactions, and in the second part, we consider a simple model to explain the experimental results.

5.2 EXPERIMENTAL

Instead of measuring the renormalization of the trap by exciting the sample by a continuous laser beam and changing the laser power, we can take advantage of the fact that the lifetime of the excitons is finite. If pulsed excitation is applied, the exciton population changes between pulses, simply because the recombination of particles removes them from the system. Beyond the convenience, dynamically measuring the luminescence spectra has an experimental advantage over the continuous measurement. During the excitation, free carriers are also created, which, in turn, produce a DC photo-current. However, this photo-current contributes to the electric field across the sample, and thus, to the energy of the indirect excitons. Changing the excitation power changes the photo-current and the energy shift associated with it. On the other hand, in the dynamic measurement, the photo-current and the related energy shift are the same for all exciton densities, because the fall time of the photo-current is much longer than the time between consecutive pulses. This means that any energy shift in the measured luminescence is a result of exciton-exciton interaction.

Since the exciton population evolves between pulses, we can thus expect any density-dependent effect to show a dynamic behavior. This is indeed the case, as we can see it in Fig. 40, where we plot the luminescence intensity as a function of both space and energy, as taken by a time-gated CCD camera. The gating time was equal to about 1/20 of the lifetime, i.e., 200 ns for an exciton lifetime of about 4 μs. By adhering to such short gating times, we can avoid non-physical broadening in the measured luminescence, since the exciton population does not change by more than 5% during the integration window.

At the initial moment, excitons are located at the point of excitation, with high density. As time goes on, their density drops both because of recombination, and because they move away from the excitation spot, and tend to fill up the trap according to the equilibrium distribution Eq. (3.13). (The excitation spot is smaller than the size dictated by Eq. (3.13).)

Fig. 41 shows the spectrum of the luminescence at the center of the trap integrated over an area of radius 10 μm, as shown in Fig. 40 for three different times after the excitation. These spectra are taken from Fig. 40, and their height is proportional to the absolute intensity. We can clearly see both the red shift at late times and the spectral narrowing of the luminescence.

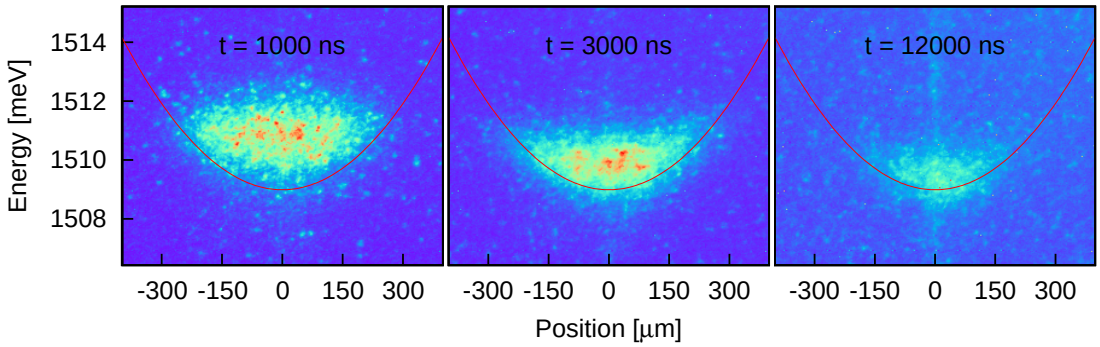

Figure 40: Luminescence in the trap at three instants in time, after a short excitation pulse. The red lines show the trap without renormalization. Time is measured from the beginning of the laser pulse, and the bath temperature is 8 Kelvin. The long vertical line on the right-most figure is the substrate luminescence excited by the very weak laser light between pulses. The spatial integration range for the spectra in Fig. 41 is between -10 and 10 μm.

Also, the spectra are not entirely symmetric, and have a low-energy tail, which is probably due to localized states.

In order to extract quantitative information, we applied the fitting function

$$f(E) = A \exp\left[\frac{(E - E_0)^2}{2c^2(1 + dE)}\right] , \tag{5.2}$$

where we introduced d as an asymmetry factor. This function fits the spectra reasonably for all times, and its width can be expressed analytically as

$$\Delta = 2c\sqrt{\ln 2}\sqrt{\ln 2c^2d^2 + 2E_0d + 2} . \tag{5.3}$$

First, we will explain how the absolute exciton density can be estimated using spectra similar to those in Fig. 41. As discussed in Chapters 1 and 3, after the exciton cloud reaches its final temperature, the luminescence intensity can be used as a measure of the exciton density. We have also shown that there is no reason to assume that the exciton cloud would cool for longer than about 500 ns. Therefore, after the initial 500 ns, we can make a direct link

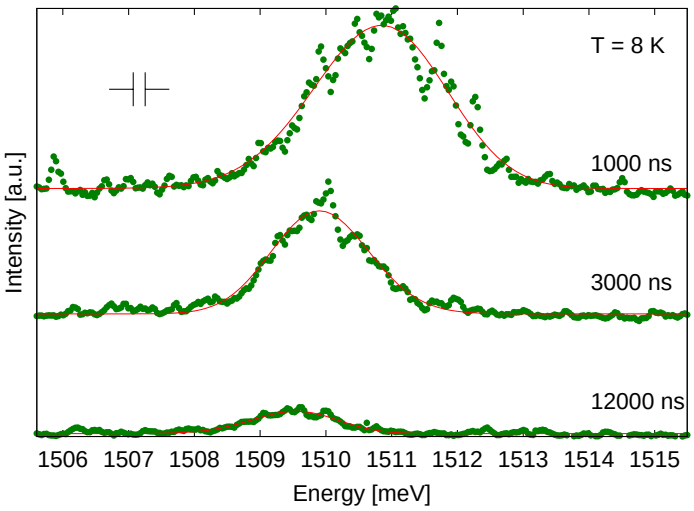

Figure 41: Luminescence spectra at the center of the trap for the same conditions as in Fig. 40. Also shown are the spectral resolution, and the fitting functions, Eq. (5.2).

between the exciton density and the luminescence blue shift, E_0, in the fitting function. Such a plot is given in Fig. 42. Initially, the dependence is double-valued, which is a consequence of the early rise-time of the luminescence intensity in Fig. 25. Then the relationship becomes linear over a wide density range. The linearity indicates that we are dealing with excitonic and not free carrier luminescence, because in the latter case the intensity is proportional to the square of the particle density [50, 133, 134]. This measurement was taken with the photomultiplier tube, and the measurement point, the center of the trap, was defined with the help of a small pin-hole, as discussed in Chapter 2.

If we could give a rough estimate for the number of created excitons for a given laser pulse energy, we could deduce the repulsion coefficient in Eq. (4.1).

We have got to take into account the following factors:

1. Direct-to-indirect exciton conversion efficiency. Under the conditions that we used, it was around 40%, which can be inferred from the relative intensities of the temporally, spatially and spectrally integrated luminescence of the direct and indirect excitons. Obviously, this

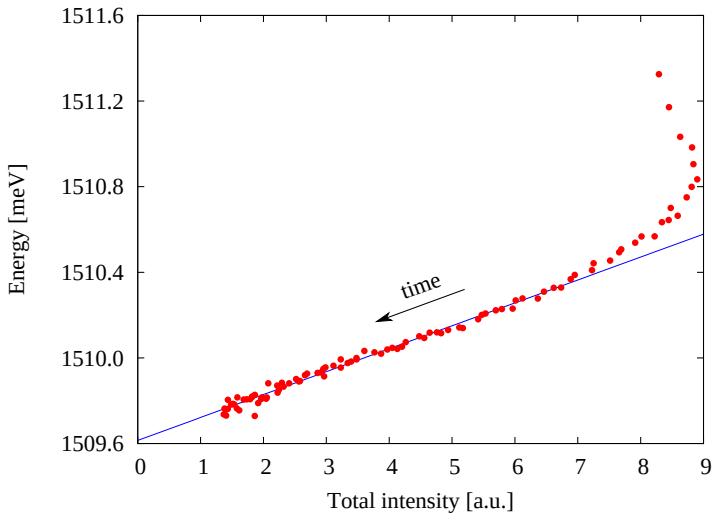

Figure 42: Energy shift at the center of the trap as a function of total luminescence intensity measured at the same point. Time flows from right to left (decreasing luminescence intensity). The initial curvature on the right hand side of the graph can be attributed to the non-monotonic behavior of the intensity at early times. The conditions are the same as in the case of Fig. 25.

number cannot be exact, for we cannot account for processes that turn direct excitons into particles that do not radiate at the indirect energy.

2. The difference in the refractive index of He liquid/vapor and GaAs, which can be approximated as

$$R = \frac{(n-1)^2}{(n+1)^2} \approx 0.29 \ , \tag{5.4}$$

for the refractive index of GaAs at $\lambda = 800$ nm is $n = 3.4$ [18, 19].

3. Reflections and losses on optical elements and cryostat windows. This could be measured simply by comparing the power of a laser source before and after it passes through the elements in question, and it turned out to be around 60%.

4. Excitonic absorption length of quantum wells. For this we take the value from Young et al. [136], who measured this by comparing the transmitted power of the excitation

laser tuned to the excitonic absorption with and without quantum wells. The absorption length for the direct exciton transition is 1.65 μm^{-1} [136, 137], and the energy is absorbed in the combined thickness of the two quantum wells, which is, in the present case, 200 Å.

5. Absorption of light in the barrier. The quantum wells are separated from the outside world by a superlattice and a 1000-Å barrier. (C.f. Fig. 6.) The superlattice is designed to be transparent for $\lambda > 760$ nm, while the barrier has an attenuation length of about 1 μm [18, 19]. Therefore, the barrier reduces the light intensity by approx. 10%.

Putting everything together, one photon creates approximately

$$\begin{array}{ccccccccccc} 0.71 & \cdot & 0.4 & \cdot & \dfrac{0.02}{1.65} & \cdot & 0.4 & \cdot & 0.9 & = & 0.003 \\ \uparrow & & \uparrow & & \uparrow & & \uparrow & & \uparrow & & \\ \text{Reflection} & & \text{conversion} & & \text{well} - \text{abs.} & & \text{optics} & & \text{GaAs barriers} & & \end{array}$$

indirect excitons on average.

With these numbers, we get an absolute exciton density of about $1.3 \cdot 10^9$ cm^{-2} for the leftmost point in Fig. 42, which implies a value of $\gamma \approx 0.9 \cdot 10^{-10}$ meV cm^2. Given the large uncertainties in the experimental estimate of the density, this value of γ is in reasonable agreement with the theoretical predictions of $\gamma \approx 1.5 \cdot 10^{-10}$ meV cm^2 of [9, 140]. We note here that Schindler and Zimmermann have recently revised this number [142, 143], claiming that it is probably reduced by a factor of about 8 due to exciton-exciton anticorrelation. This, however, would mean that the absolute exciton density corresponding to the same shift should be 8 times higher. The only place where we could have missed a factor of 8 is the absorption length of the quantum wells, which, instead of 1.65 μm, should then be around 200 nm. While this is not impossible that it is indeed 200 nm, the fact that it is so different from the established value in [136, 137] makes it somewhat untenable.

5.3 LINE BROADENING

The interaction of excitons presents itself not only in the shift of the luminescence energy, but also in its width: the very interaction that is responsible for the correction of the energy is

also responsible for the increased collision rate that, in turn, leads to an increased linewidth. This is what would make the link between the shift and the broadening important from the theoretical point of view, because a complete theory should be capable of predicting the relationship of both from the same principles, without any reference to the absolute densities.

Looking back at Fig. 40, we can see that as time goes on, or as the density of the exciton cloud drops, the luminescence line becomes sharper. In order to quantitatively assess this behavior, we determined the spectral width as defined in Eq. (5.2), and took the instrumental resolution into account. In principle, we could de-convolve the measured spectrum with the instrumental resolution, which could be defined as the spectrum of a very narrow spectral standard. Instead of doing this, we will assume that both the true spectrum and the instrumental resolution can be described by Gaussians functions of widths σ_1 and σ_2, respectively. With these, the measured spectrum would have a width of $\sigma_{meas} = \sqrt{\sigma_1^2 + \sigma_2^2}$, i.e., the true line width can be obtained as $\sigma_1 = \sqrt{\sigma_{meas}^2 - \sigma_2^2}$. σ_2 is mainly determined by the slit openings of the spectrometer, and in the present experiments, it was about 0.1 meV.

We plot σ_1 as a function of the energy shift, or, in terms of the fit parameters, Δ vs. E_0, where we now measure E_0 from the energy at zero density, or the intercept on the energy (vertical) axis in Fig. 42. This line is shown in Fig. 43 for a high and a low temperature case. The dependence of the width on the shift could always be fitted by a straight line, with a well-defined slope, i.e., the line width is given by

$$\Delta = \delta(T)(E - E(n_{ex} = 0)) + \Delta_0 = \delta(t)E_0 + \Delta_0 \ . \tag{5.5}$$

In Fig. 43, for the low temperature case, the linewidth seems to come to a constant value at very low shift. We take this constant to be the inhomogeneous broadening due to disorder. Homogeneous broadening owing to phonon scattering is negligible at these low temperatures [49, 138, 139]. We excluded those points from the linear fits. Apart from those points, the straight lines belonging to different temperatures clearly have different slopes.

These slopes, δ, are summarized in Fig. 44 for a temperature range of 2-20 Kelvin. Surprisingly, even at the lowest temperatures, the slope takes on a positive value, and by extrapolation, we would get a value of about 0.2 for the T=0 case.

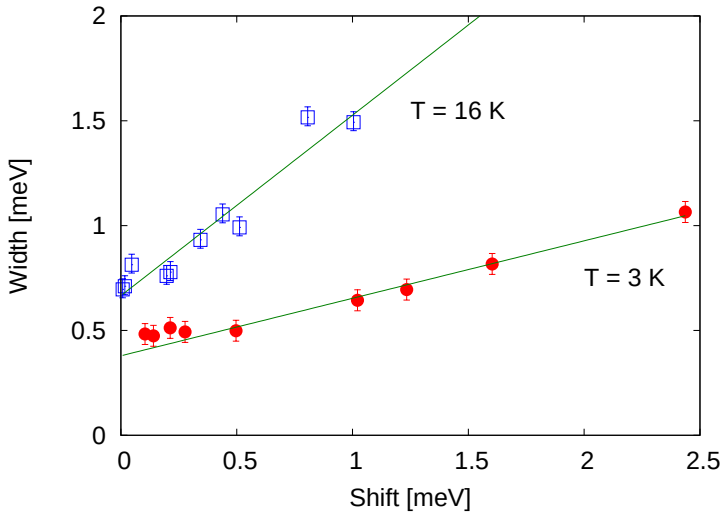

Figure 43: Line broadening as a function of line shift for the 120-Å double quantum well at 3 K and 16 Kelvin. The errorbars were determined from the errors in the fits.

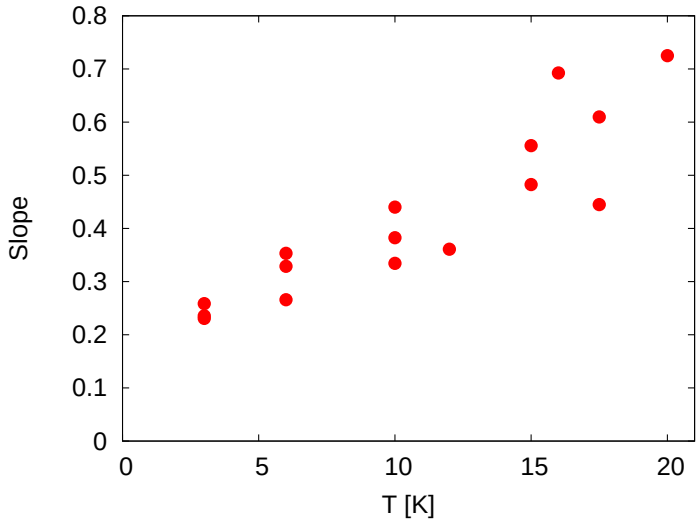

Figure 44: Line broadening coefficient, δ, as a function of temperature for the 120-Å double quantum well.

We can qualitatively explain the behavior above if we calculate the energy shifts and the broadening of the luminescence as a function of temperature. We shall consider only exciton-exciton interaction. At higher temperatures, when, e.g., optical phonons are thermally excited, this description would obviously break down. However, the activation energy of optical phonons in GaAs is around 35 meV [18], or about 400 Kelvin, which is much higher than the energy range we are interested in. According to an experimental study by Gopal et al. [145], interaction with optical phonons should not be relevant below 50-60 Kelvin. From the work of Rudin and Reinecke [146] we can also conclude that for a wide range of quantum well width, the interaction with acoustic phonons results in a line-broadening of about 1-3 μeV/K. This is also consistent with the findings of Feldmann et al. [49]. Nor do we consider scattering with impurities and quantum well width fluctuations, because as we deduced in Eq. (2.19), the characteristic scattering time for these quantum wells is around 10 ps, which would result in a broadening of about 0.06 meV, which is much smaller than the one measured here.

We also have to point out that the blue shift that we measure could, in principle, also be related to a change in the binding energy of excitons. Indeed, Aouani et al. [61] deduced how the presence of an electron-hole plasma affects the binding energy. However, if the change in the binding energy were relevant in our case, then it would also affect the exciton lifetime, and we would not measure a single exponential decay as in Fig. 25. Therefore, we can rule out this possibility.

5.4 THEORETICAL CONSIDERATIONS

To calculate the scattering rate for exciton-exciton interaction, we denote the momentum of the in-coming particles by $\vec{k}_1$ and $\vec{k}_2$, while that of the out-going particles by $\vec{k}_3$ and $\vec{k}_4$. We will assume that the two-body potential depends on the absolute value of the momentum transfer, $|\vec{k}_1 - \vec{k}_3|$. (Momentum conservation ensures that the momentum transfer for particles

2 and 4 is the same.) Then the two-body interaction takes the form

$$U = \frac{1}{L^2} \sum_{\vec{k}_1,\vec{k}_2,\vec{k}_3,\vec{k}_4} U_{\vec{k}_1,\vec{k}_2,\vec{k}_3,\vec{k}_4} a^\dagger_{\vec{k}_4} a^\dagger_{\vec{k}_3} a_{\vec{k}_2} a_{\vec{k}_1} = \frac{1}{L^2} \sum_{\vec{k}_1,\vec{k}_2,\vec{k}_3,\vec{k}_4} U(|\vec{k}_1 - \vec{k}_3|) a^\dagger_{\vec{k}_4} a^\dagger_{\vec{k}_3} a_{\vec{k}_2} a_{\vec{k}_1} \ . \tag{5.6}$$

If we assume that the state of the system without interaction is adequately described by the Fock vector

$$|i\rangle = |\dots N_{\vec{k}_1} \dots N_{\vec{k}_2} \dots N_{\vec{k}_3} \dots N_{\vec{k}_4} \dots \rangle \ , \tag{5.7}$$

then treating the interaction as a perturbation leads to the renormalization of the eigenenergies [59]. In Eq. (5.7) $N_{\vec{k}_1}$ is the *number* of particles in the state discribed by the wave vector $\vec{k}_1$. In first order, the interaction potential leads to the perturbation energy

$$\Delta^{(1)} = \langle i|U|i\rangle \ , \tag{5.8}$$

while the next order is

$$\Delta^{(2)} = \mathcal{P} \left(\sum_m \frac{|\langle m|U|i\rangle|^2}{E_i - E_m} \right) \ , \tag{5.9}$$

and

$$\Gamma^{(2)} = \pi \sum_m |\langle m|U|i\rangle|^2 \delta(E_i - E_m) \ , \tag{5.10}$$

where $\mathcal{P}$ stands for the principal value, and m runs through the intermediate states. $\Delta^{(1)}$ and $\Delta^{(2)}$ are the real energy shifts, while $\Gamma^{(2)}$ is the imaginary part of the energy, which leads to line broadening.

In all three cases, we have to evaluate matrix elements of the form $\langle m|U|i\rangle$. Moreover, we are interested in the shift and broadening of one particular exciton state, which we will denote by $\vec{k}_1$. Since this is our initial or final state, we will not integrate over it.

Taking the Fock state in Eq. (5.7), the action of $a^\dagger_{\vec{k}_4} a^\dagger_{\vec{k}_3} a_{\vec{k}_2} a_{\vec{k}_1}$ on this state is

$$\begin{aligned} & a^\dagger_{\vec{k}_4} a^\dagger_{\vec{k}_3} a_{\vec{k}_2} a_{\vec{k}_1} \quad | \quad \dots N_{\vec{k}_1} \dots N_{\vec{k}_2} \dots N_{\vec{k}_3} \dots N_{\vec{k}_4} \dots \rangle \\ = & \sqrt{N_{\vec{k}_1}} \sqrt{N_{\vec{k}_2}} \sqrt{1 + N_{\vec{k}_3}} \sqrt{1 + N_{\vec{k}_4}} \quad | \quad \dots N_{\vec{k}_1} - 1 \dots N_{\vec{k}_2} - 1 \dots N_{\vec{k}_3} + 1 \dots N_{\vec{k}_4} + 1 \dots \rangle \ , \end{aligned} \tag{5.11}$$

except for the case when $\vec{k}_1 = \vec{k}_3$ or $\vec{k}_1 = \vec{k}_4$. Since this state is multiplied by $\langle m|$, and the Fock states are orthonormal, $\langle m|a^\dagger_{\vec{k}_4} a^\dagger_{\vec{k}_3} a_{\vec{k}_2} a_{\vec{k}_1}|i\rangle \neq 0$ only if

$$\langle m| = \langle \dots N_{\vec{k}_1} - 1 \dots N_{\vec{k}_2} - 1 \dots N_{\vec{k}_3} + 1 \dots N_{\vec{k}_4} + 1 \dots | \ , \tag{5.12}$$

i.e., the action of $a^\dagger_{\vec{k}_4} a^\dagger_{\vec{k}_3} a_{\vec{k}_2} a_{\vec{k}_1}$ on $|i\rangle$ fixes $\langle m|$.

When calculating the perturbed energies, for the sake of simplicity, we will assume a parabolic and isotropic dispersion relation, thus the occupation numbers $f(\vec{k}) = N_{\vec{k}}$ can be simplified as $f(\vec{k}) = f(k^2)$. We will also use the abbreviation $g(k) = 1 + f(k)$.

Let us begin with the calculation of the first order shift. In this case we do not sum over the intermediate states, and we also have the restriction $\langle m| = \langle i|$. This means that the creation and destruction operators must be paired in the potential, namely, either $\vec{k}_1 = \vec{k}_3$ and $\vec{k}_2 = \vec{k}_4$, or $\vec{k}_1 = \vec{k}_4$ and $\vec{k}_2 = \vec{k}_3$. We can also drop the condition on momentum conservation, for $\vec{k}_1 + \vec{k}_2 = \vec{k}_3 + \vec{k}_4$ is automatically satisfied in this case. Finally, when the creation operators act on a state, a particle with that particular wave vector has already been removed, i.e., the prefactor of the creation operator is not $\sqrt{1+N}$, but simply $\sqrt{N}$. Therefore, the first order shift in the total energy can be calculated as

$$\begin{aligned}
\Delta^{(1)}_{\vec{k}_1} &= \frac{1}{L^2} \sum_{\vec{k}_2,\vec{k}_3,\vec{k}_4} U(|\vec{k}_1 - \vec{k}_3|) \langle i| a^\dagger_{\vec{k}_4} a^\dagger_{\vec{k}_3} a_{\vec{k}_2} a_{\vec{k}_1} |i\rangle \\
&= \frac{1}{L^2} \sum_{\vec{k}_2,\vec{k}_3,\vec{k}_4} U(|\vec{k}_1 - \vec{k}_3|) \sqrt{N_{\vec{k}_1}} \sqrt{N_{\vec{k}_2}} \sqrt{N_{\vec{k}_3}} \sqrt{N_{\vec{k}_4}} \left(\delta_{\vec{k}_1,\vec{k}_3} \delta_{\vec{k}_2,\vec{k}_4} + \delta_{\vec{k}_1,\vec{k}_4} \delta_{\vec{k}_2,\vec{k}_3} \right) \\
&= \frac{1}{L^2} \left(\frac{L}{2\pi} \right)^2 N_{\vec{k}_1} \left\{ U(0) \int d\vec{k}_2 N_{\vec{k}_2} + \int d\vec{k}_2 N_{\vec{k}_2} U(|\vec{k}_1 - \vec{k}_2|) \right\} \\
&= \frac{N_{\vec{k}_1}}{4\pi^2} \left\{ U(0) N + \int d\vec{k}_2 N_{\vec{k}_2} U(|\vec{k}_1 - \vec{k}_2|) \right\} \qquad (5.13)
\end{aligned}$$

This is the *total* energy change in first order, where the second term is the bosonic *exchange* term. If we want to calculate the shift in the luminescence energy, we need the energy change *per particle*. Therefore, the shift in the emission energy is

$$\Delta E_{k_1} = \frac{\Delta^{(1)}_{k_1}}{N_{k_1}} = U(0) n + \frac{1}{4\pi^2} \int d\vec{k}_2 N_{\vec{k}_2} U(|\vec{k}_1 - \vec{k}_2|) \ , \qquad (5.14)$$

which is linear in the total particle density, n. We also notice that this correction to the energy is independent of the temperature, if the scattering potential is independent of the momentum transfer, $|\vec{k}_1 - \vec{k}_2|$, in which case it reduces to

$$\Delta E_{k_1} = 2U(0) n \ . \qquad (5.15)$$

We now calculate the line broadening given by Eq. (5.10). With the assumption on the dispersion relation, the delta function in energy can be replaced by a delta function in the square of the absolute value of the vectors. Hence, the integrand in Eq. (5.10) takes on the form

$$\begin{aligned} S(\vec{k}_1,\vec{k}_2,\vec{k}_3,\vec{k}_4) &= \frac{U^2(|\vec{k}_1-\vec{k}_3|)}{L^4}\left(\frac{L}{2\pi}\right)^4 \delta(\vec{k}_1+\vec{k}_2-\vec{k}_3-\vec{k}_4)\delta(k_1^2+k_2^2-k_3^2-k_4^2) \\ &\quad \times f(k_1^2)f(k_2^2)g(k_3^2)g(k_4^2)\ . \end{aligned} \tag{5.16}$$

First, we take advantage of the delta function of the momentum to eliminate $\vec{k}_4$, thus an integration over $\vec{k}_4$ results in

$$\begin{aligned} \int d\vec{k}_4 S(\vec{k}_1,\vec{k}_2,\vec{k}_3,\vec{k}_4) &= U^2(|\vec{k}_1-\vec{k}_3|)\left(\frac{1}{2\pi}\right)^4 \delta(k_1^2+k_2^2-k_3^2-|\vec{k}_1+\vec{k}_2-\vec{k}_3|^2) \\ &\quad \times f(k_1^2)f(k_2^2)g(k_3^2)g(|\vec{k}_1+\vec{k}_2-\vec{k}_3|^2)\ . \end{aligned} \tag{5.17}$$

We now define $\vec{k}' = \vec{k}_1 - \vec{k}_3$, i.e., by denoting the angle between $\vec{k}_2$ and $\vec{k}'$ by ϑ_2, we get

$$|\vec{k}_1+\vec{k}_2-\vec{k}_3|^2 = |\vec{k}'+\vec{k}_2|^2 = k'^2+k_2^2+2k'k_2\cos\vartheta_2\ . \tag{5.18}$$

We define ϑ_3 in a similar fashion, as the angle between $\vec{k}_1$ and $\vec{k}_3$. Thus, an integration over $\vec{k}_2$ yields

$$\begin{aligned} \int d\vec{k}_2 d\vec{k}_4 S(\vec{k}_1,\vec{k}_2,\vec{k}_3,\vec{k}_4) &= U^2(k')\left(\frac{1}{2\pi}\right)^4 \int d\vec{k}_2 \delta(k_1^2+k_2^2-k_3^2-|\vec{k}'+\vec{k}_2|^2) \\ &\quad \times f(k_1^2)f(k_2^2)g(k_3^2)g(|\vec{k}'+\vec{k}_2|^2) \\ &= U^2(k')\left(\frac{1}{2\pi}\right)^4 \int k_2 dk_2 d\vartheta_2 \delta(k_1^2-k_3^2-k'^2-2k'k_2\cos\vartheta_2) \\ &\quad \times f(k_1^2)f(k_2^2)g(k_3^2)g(|\vec{k}'+\vec{k}_2|^2)\ . \end{aligned}$$

We integrate over ϑ_2 first to eliminate the Dirac delta by making use of the identity

$$\int dy\, h(y)\delta(l(y)) = \sum_i \frac{h(y_i)}{|l'(y_i)|}\ , \tag{5.19}$$

where the summation runs over the roots of $l(y)$. Substituting $l(\vartheta_2) = k_1^2 - k_3^2 - k'^2 - 2k'k_2\cos\vartheta_2$, and using $\sin(\cos^{-1}(x)) = \pm\sqrt{1-x^2}$, we arrive at

$$\int_0^{2\pi} d\vartheta_2 \delta(k_1^2 - k_3^2 - k'^2 - 2k'k_2\cos\vartheta_2) = \frac{2}{2k'k_2\sqrt{1-\left(\frac{k_1^2-k_3^2-k'^2}{2k'k_2}\right)^2}} \tag{5.20}$$

where the factor of 2 comes from the summation over the two roots of the cosine. When evaluating the Dirac delta, we also need to guarantee that we have roots; this gives a condition on the length of $\vec{k}_2$, because we demand

$$|k_1^2 - k_3^2 - k'^2| < 2k'k_2 \ , \tag{5.21}$$

which, after solving for k_2, can be cast as

$$k_2 > \max\left(\frac{k_1^2 - k_3^2 - k'^2}{2k'}, \frac{k_3^2 - k_1^2 + k'^2}{2k'}\right) = K_{\min} \ . \tag{5.22}$$

Thus the integration over $\vec{k}_2$ results in

$$\int d\vec{k}_2 d\vec{k}_4 S(\vec{k}_1,\vec{k}_2,\vec{k}_3,\vec{k}_4) = \left(\frac{1}{2\pi}\right)^4 U^2(|\vec{k}_1-\vec{k}_3|^2)\int_{K_{\min}}^{\infty} dk_2 \frac{f(k_1^2)f(k_2^2)g(k_3^2)g(k_1^2+k_2^2-k_3^2)}{k'\sqrt{1-\left(\frac{k_1^2-k_3^2-k'^2}{2k_2k'}\right)^2}} \tag{5.23}$$

Since we still need to integrate over $\vec{k}_3$, the scattering integral becomes

$$\begin{aligned} S(\vec{k}_1) &= \left(\frac{1}{2\pi}\right)^4 \int_0^{2\pi} d\vartheta_3 \int_0^{\infty} k_3 dk_3 U^2(|\vec{k}_1-\vec{k}_3|)\int_{K_{\min}}^{\infty} dk_2 f(k_1^2)f(k_2^2)g(k_3^2) \\ &\quad \times \frac{g(k_1^2+k_2^2-k_3^2)}{k'\sqrt{1-\frac{k_3^2(k_1\cos\vartheta_3-k_3)^2}{k_2^2(k_1^2+k_3^2-2k_1k_3\cos\vartheta_3)}}} \ . \end{aligned} \tag{5.24}$$

Assuming that the distribution function is classical, i.e., $g(k^2)$ can be replaced by 1, leads to

$$\Gamma^{(2)}_{\vec{k}_1,out} = \frac{2m}{\hbar^2}\frac{1}{16\pi^3}\int_0^{2\pi} d\vartheta_3 \int_0^{\infty} k_3 dk_3 U^2(|\vec{k}_1-\vec{k}_3|)\int_{K_{\min}}^{\infty} dk_2 \frac{f(k_1^2)f(k_2^2)}{k'\sqrt{1-\frac{k_3^2(k_1\cos\vartheta_3-k_3)^2}{k_2^2(k_1^2+k_3^2-2k_1k_3\cos\vartheta_3)}}} \ . \tag{5.25}$$

This expression gives the rate of scattering *out* of state $\vec{k}_1$, since the initial state was $\vec{k}_1$. In order to calculate the total scattering rate, we have to account for processes that have $\vec{k}_1$ as their final state. Instead of calculating the integral for the scattering *in*, we can note that

in thermal equilibrium, the two scattering rates should be equal to each other, and thus the total scattering rate is then obtained as the sum of these two, i.e.,

$$\Gamma_1^{(2)} = 2\Gamma_{\vec{k}_1,out}^{(2)} \ . \tag{5.26}$$

The second order shift is given by Eq. (5.9). The only differences between this term and Eq. (5.10) are the energy denominator and the absence of the restriction on energy conservation. (In fact, the energy denominator plays a role very similar to that of the Dirac delta.) The energy denominator can be obtained if we reckon that, with respect to the initial state $|i\rangle$, in the intermediate state $\langle m|$ we have one more particle at momentum $\vec{k}_3$ and $\vec{k}_4$, and one less particle at momentum $\vec{k}_1$ and $\vec{k}_2$, respectively. Therefore,

$$E_i - E_m = \frac{\hbar^2}{2m}(k_1^2 + k_2^2 - k_3^2 - k_4^2) \ . \tag{5.27}$$

Using this expression for the denominator, $\Delta_{k_1}^{(2)}$ can be calculated in the same way as $\Gamma_{k_1}^{(2)}$. First, we define $\vec{k}' = \vec{k}_1 - \vec{k}_3$, and integrate over $\vec{k}_4$. Hence,

$$\begin{aligned}
\Delta_{k_1}^{(2)} &= \frac{2m}{\hbar^2}\left(\frac{1}{2\pi}\right)^4 \int d\vec{k}_3 \int d\vec{k}_2 \int d\vec{k}_4 \frac{U^2(|\vec{k}_1 - \vec{k}_3|) f(k_1^2) f(k_2^2)}{k_1^2 + k_2^2 - k_3^2 - k_4^2} \delta(\vec{k}_1 + \vec{k}_2 - \vec{k}_3 - \vec{k}_4) \\
&= \frac{2m}{\hbar^2}\left(\frac{1}{2\pi}\right)^4 \int d\vec{k}_3 \int d\vec{k}_2 \frac{U^2(|\vec{k}_1 - \vec{k}_3|) f(k_1^2) f(k_2^2)}{k_1^2 + k_2^2 - k_3^2 - |\vec{k}' + \vec{k}_2|^2} \\
&= \frac{2m}{\hbar^2}\left(\frac{1}{2\pi}\right)^4 \int d\vec{k}_3 \int k_2 dk_2 \int d\vartheta_2 \frac{U^2(|\vec{k}_1 - \vec{k}_3|) f(k_1^2) f(k_2^2)}{k_1^2 - k_3^2 - k'^2 - 2k' k_2 \cos\vartheta_2}
\end{aligned} \tag{5.28}$$

where ϑ_2 is the angle between $\vec{k}'$ and $\vec{k}_2$

We perform the integration over ϑ_2 first. The integral has the form

$$\int_0^{2\pi} \frac{d\vartheta}{A + B\cos\vartheta} \ , \tag{5.29}$$

which can be evaluated by the method of residues. First, we introduce the new variable $z = e^{i\theta}$, and integrate on the unit circle as

$$\int_0^{2\pi} \frac{d\theta}{A + B\cos\theta} = \oint_{|z|=1} \frac{dz}{i(zA + Bz^2/2 - B/2)} = \oint_{|z|=1} \frac{2dz}{iB(z - z_1)(z - z_2)} \ , \tag{5.30}$$

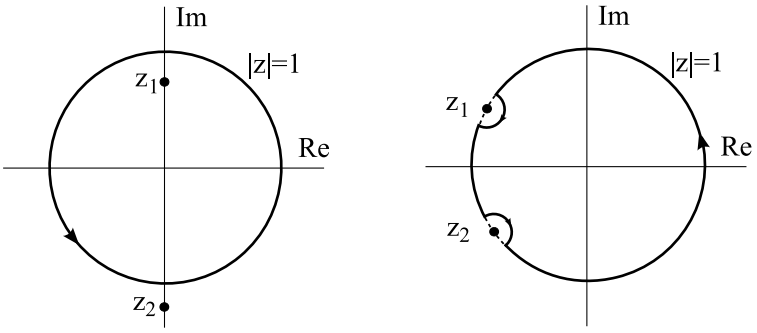

Figure 45: The location of the two poles for $|A| > B$ (left), and for $|A| < B$ (right). Also shown is the integration contour for both cases.

with

$$z_1 = i\frac{\sqrt{A^2 - B^2} - A}{B} \qquad \text{and} \qquad z_2 = -i\frac{\sqrt{A^2 - B^2} + A}{B} \tag{5.31}$$

In the case $|A| > B$, the integrand has a pole at z_1 and another one at z_2. Only z_1 is inside the unit circle, and thus the integral is

$$\oint_{|z|=1} \frac{1}{iB/2(z - z_1)(z - z_2)} = 2\pi i \mathrm{Res}_{z=z_1} \frac{2}{iB(z - z_1)(z - z_2)} = \frac{4\pi}{B(z_2 - z_1)} = \frac{2\pi}{\sqrt{A^2 - B^2}} \ . \tag{5.32}$$

Obviously, if $A < 0$, then the integral is negative, while for $A > 0$ it is positive.

When, on the other hand, $|A| < B$, the poles are located at $z_1 = -(\sqrt{B^2 - A^2} - iA)/B$ and $z_2 = (\sqrt{B^2 - A^2} - iA)/B$, both on the unit circle. We can, therefore, cut them out, and integrate along a small arc of radius ϵ at the two poles, and then take the $\epsilon \to 0$ limit, as shown in Fig. 45. For any $\epsilon > 0$, the integral evaluates to zero, for there are no singularities enclosed. Therefore, in the case $|A| < B$, the integral is zero. It should be emphasized that cutting out the singularities on the unit circle is nothing else but the meaning of the principal value integral in Eq. (5.9).

The condition $A > B$ translates to

$$\frac{k_1^2 - k_3^2 - k'^2}{2k'} > k_2 \tag{5.33}$$

while $-A > B$ is equivalent to

$$\frac{k_3^2 + k'^2 - k_1^2}{2k'} > k_2 \ . \tag{5.34}$$

Substituting the value of A and B into Eq. (5.28) gives

$$\Delta_{k_1}^{(2)} = \frac{2m}{\hbar^2}\frac{f(k_1^2)}{8\pi^3}\int d\vec{k}_3 U^2(|\vec{k}_1 - \vec{k}_3|)\int_0^{K_{\min}} dk_2 \frac{f(k_2^2)\mathrm{sgn}(k_1^2 - k_3^2 - k'^2)}{k'\sqrt{\frac{k_3^2(k_1\cos\vartheta_3 - k_3)^2}{k_2^2(k_1^2+k_3^2-2k_1k_3\cos\vartheta_3)} - 1}} \ , \tag{5.35}$$

where $\mathrm{sgn}(x)$ is the sign of x, and $K_{\min}$ was defined in Eq. (5.22).

The first and second order shifts and the broadening in Eqs. (5.14), (5.25), (5.35) do not have a temperature dependence for U=constant, as can be shown on dimensional grounds.

5.4.1 Numerical considerations

The integrals in Eqs. (5.14), (5.25), (5.35) do not lend themselves to analytical evaluation; therefore, we have to calculate them numerically. We then must define infinity and the bin size. It seems plausible to choose the maximum length of the wave vector, $k_{\max}$, to coincide with ten times the thermal energy, in which case, the occupation number drops to about 10^{-5} at the upper bound, and to choose the minimum length of the wave vector, $k_{\min}$, to be equal to the inverse of the size of the system. 1 cm for the size is a good order-of-magnitude definition, given that in most cases the wafer was about 5 mm by 5 mm.

The functions under the integrals change rapidly in the vicinity of the limit, $K_{\min}$. Therefore, we can cut out this point, and integrate between $K_{\min} \pm k_{\min}$ and the other limit. In order to account for the rapid change, we adjust the mesh size, and sum over intervals of $k_{\min}, (1+\varepsilon)k_{\min}, (1+\varepsilon)^2 k_{\min}, (1+\varepsilon)^3 k_{\min} \ldots$ as we move farther from the singularity. In this way we add numbers that are of the same order of magnitude. Once the integration over k_2 is performed, the other three variables are regular, and we do not expect any numerical difficulties, thus we can take an equidistant mesh in the angles (in all cases dividing the total angle by a number between 100 and 200 worked), and a mesh increasing as $k_{\min}, (1+\varepsilon)k_{\min}, (1+\varepsilon)^2 k_{\min}, (1+\varepsilon)^3 k_{\min} \ldots$ for k_3. This means that $1+\varepsilon \approx \exp(\ln(k_{\max}/n))$, where n is the number of mesh points.

In order to ascertain that the numerical results are consistent, we compared the values of the integrals as the number of mesh points is increased by a factor of 10. The convergence

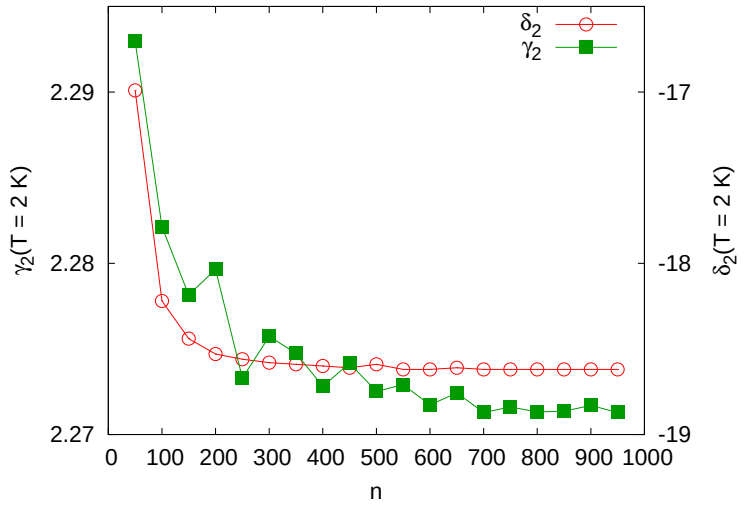

Figure 46: The convergence of the two integrals in Eqs. (5.25),(5.35) as the number of mesh points is increased. The angular resolution was fixed at $\pi/50$, and the units are $\frac{2m}{\hbar^2}\frac{\tilde{u}^2}{8\pi^3}n_{\rm ex}$.

at $T = 2$ K is shown in Fig. 46. The division in angle was 100. We see that at around 250, δ_2 becomes flat, and even around 400 divisions, the deviation of γ_2 from the limiting value is less than a percent.

5.4.2 Numerical results

First we define the functions $\delta_1(\vec{k}_1, T), \delta_2(\vec{k}_1, T)$ and $\gamma_2(\vec{k}_1, T)$ as

$$\delta_1(\vec{k}_1, T) = \int d\vec{k}_2 N_{\vec{k}_2} |\vec{k}_1 - \vec{k}_2|^\eta \ , \tag{5.36}$$

$$\delta_2(\vec{k}_1, T) = \int_0^{2\pi} d\vartheta_3 \int_0^\infty k_3 dk_3 |\vec{k}_1 - \vec{k}_3|^{2\eta} \int_0^{K_{\rm min}} dk_2 \frac{f(k_2^2)\mathrm{sgn}(k_1^2 - k_3^2 - k'^2)}{k'\sqrt{\frac{k_3^2(k_1\cos\vartheta_3 - k_3)^2}{k_2^2(k_1^2+k_3^2-2k_1k_3\cos\vartheta_3)} - 1}} \ , \tag{5.37}$$

and

$$\gamma_2(\vec{k}_1, T) = \int_0^{2\pi} d\vartheta_3 \int_0^\infty k_3 dk_3 |\vec{k}_1 - \vec{k}_3|^{2\eta} \int_{K_{\rm min}}^\infty dk_2 \frac{f(k_1^2) f(k_2^2)}{k'\sqrt{1 - \frac{k_3^2(k_1\cos\vartheta_3 - k_3)^2}{k_2^2(k_1^2+k_3^2-2k_1k_3\cos\vartheta_3)}}} \ , \tag{5.38}$$

where the scattering potential is equal to $U(k) = \tilde{u}k^{\eta}$. With these, the shifts and broadening are given by

$$\Delta_1 = \frac{\tilde{u}}{4\pi^2}\delta_1(\vec{k}_1, T) \ , \tag{5.39}$$

$$\Delta^{(2)} = \frac{2m}{\hbar^2}\frac{\tilde{u}^2}{8\pi^3}\delta_2(\vec{k}_1, T) \ , \tag{5.40}$$

$$\Gamma^{(2)} = \frac{2m}{\hbar^2}\frac{\tilde{u}^2}{8\pi^3}\gamma_2(\vec{k}_1, T) \ . \tag{5.41}$$

We still need to specify the scattering potentials. We will study the case $U \sim \sqrt{k}$, because, based on the work of Schindler and Zimmermann, this dependence seems to be physically justified [143]. The theory for the scattering potential is based on a Heitler-London-type symmetrized two-exciton wavefunction. As they pointed out, a standard Hartree-Fock approach, which uses an incorrect normalization of the wavefunctions, would overestimate the strength of the scattering potential. Having obtained the two-body interaction, they use it in a T-matrix, which accounts for the self-energy and the bosonic direct and exchange terms. This calculation gives $U(k) \sim \sqrt{k}$, which in real space would give the expected $U(r) \sim 1/r^3$ behavior for large r. The scattering amplitude as a function of momentum with a fit to $\sim \sqrt{k}$ is shown in Fig. 47.

In their many-body theory, Schindler and Zimmermann deduce the temperature dependence of the shift and broadening of the perturbation energies, which is shown in Fig.48 for the case of a 120-Å double quantum well. The figure gives the relative weight of the real and imaginary parts, in units of the energy given by the capacitor formula in Eq. (5.1). It is important to point out that, since this theory gives only a correction to capacitor formula in the form of a multiplicative factor, both the energy shift and the broadening are linear in the exciton density.

Using these results, we can plot the ratio of the broadening to the shift (essentially the slope in Fig.44), which is shown in Fig.49. As can be seen, the instead of increasing, the slope decreases as the temperature increases. We will return to the possible reasons behind this.

Having discussed the theoretical results in [143], we now turn to the simple second-order perturbation theory outline at the beginning of this section. First, we plot $\delta_2(\vec{k}_1 \to 0, T)$

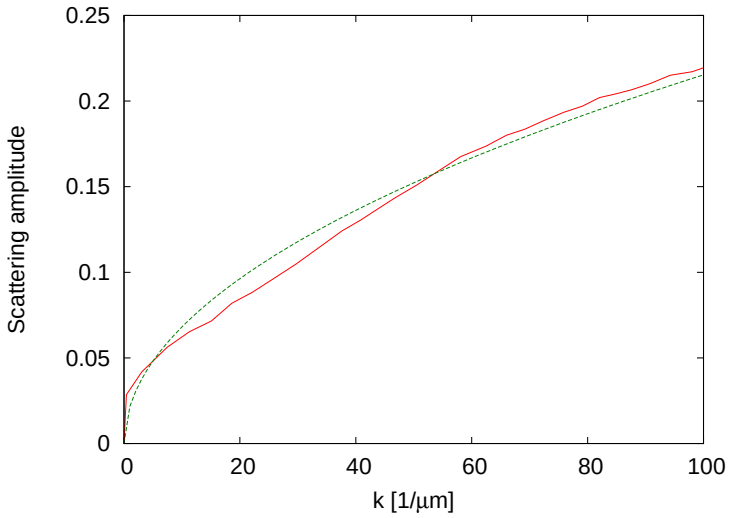

Figure 47: Real part of the total scattering amplitude as a function of momentum (solid red line). Also shown is a fit to $\sqrt{k}$ (green dashed line). From [143].

and $\gamma_2(\vec{k}_1 \to 0, T)$ in Fig. 50 as a function of temperature. The coefficient in the real part, $\delta_2(T)$, is always negative. We can understand this, if we recall that that integral depends on the sign of the quantity $k_1 \cos\vartheta_3 - k_3$, which is almost always negative, therefore, we expect that the integral is negative.

In Eq. (5.41) $\tilde{u}$ and $U(0)$ play the role of the fitting parameters. We see that the broadening is linear in the density, as is the blue shift. Thus, with a proper $\tilde{u}$ and $U(0)$, the broadening vs. blue shift can be fitted, and it gives a linear relation, as in Fig. 43. However, what would give a stricter condition for $\tilde{u}$ and $U(0)$ is the temperature dependence of the broadening vs. blue shift curves in Fig. 44.

In the next figure, Fig. 51, we plot the ratio of $\Gamma_2(0,T)$ and $\Delta_1(0,T) + \Delta^{(2)}(0,T)$, given by

$$\delta(T) = \frac{\Gamma^{(2)}}{\Delta_1 + \Delta^{(2)}} = \frac{\frac{2m}{\hbar^2}\frac{\tilde{u}}{2\pi}\gamma_2(\vec{k}_1, T)}{\delta_1(\vec{k}_1, T) + \frac{2m}{\hbar^2}\frac{\tilde{u}}{2\pi}\delta_2(\vec{k}_1, T)} \ . \tag{5.42}$$

The value of $\frac{2m}{\hbar^2}\frac{\tilde{u}}{2\pi}$ for the best fit is $1.3 \cdot 10^{-4}$ $\sqrt{\text{cm}}$, which corresponds to $\tilde{u} = 1.55 \cdot 10^{-15}$ meVcm$^{5/2}$. While the trend is obtained correctly, the theory does not fit the experimental

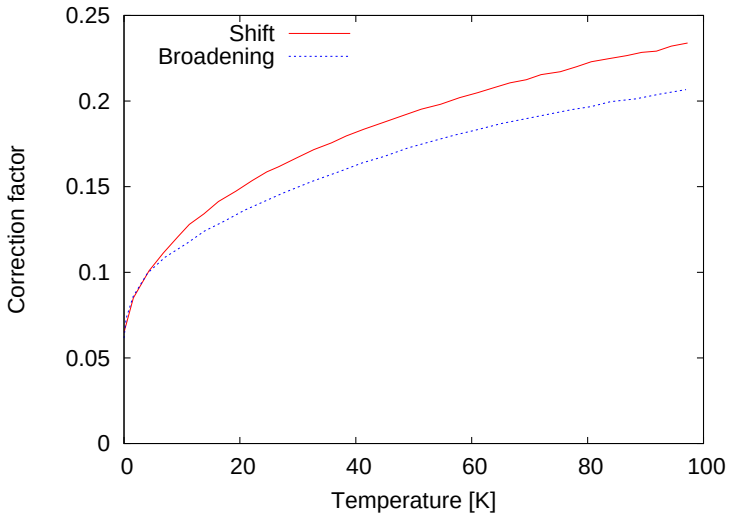

Figure 48: Real (solid red line) and imaginary (dashed blue line) part of the energy correction as a function of temperature. The unit of the energy is $\frac{4\pi ed}{\epsilon} n_{\text{ex}}$, where n_{ex} is the exciton density. From [143].

points accurately. We cannot increase the slope of the curve any further by making $\tilde{u}$ larger, because δ_1 does not depend on $\tilde{u}$, but the second factor in the denominator does, and it is negative, which means that for large $\tilde{u}$ the denominator switches sign. In other words, the slope of the curve in Fig. 51 will become negative as we pass through a singularity when we increase $\tilde{u}$. This value of $\tilde{u}$ is about 10 times larger than the value of Schindler and Zimmermann, $\tilde{u} = 1.5 \cdot 10^{-16}$ meVcm$^{5/2}$.

As we have seen above, the full many-body theory fails to account for the increasing slope, and the simple second-order theory gives too small an interaction potential. One possible reason is that in both cases, the handling of the integration cut-off is somewhat arbitrary. For the broadening it is not necessarily a problem, because in Eq. (5.25), the integration is between K_{min} and ∞, but the integrand is weighed by the occupation number $f(k_2^2)$, which very rapidly tends to zero. Therefore, changing the upper limit of the integral to $10k_BT$ from ∞ does not make any measurable difference. In other words, a reasonable upper bound can be assigned to the value of k_3, because the integration over k_2 automatically provides

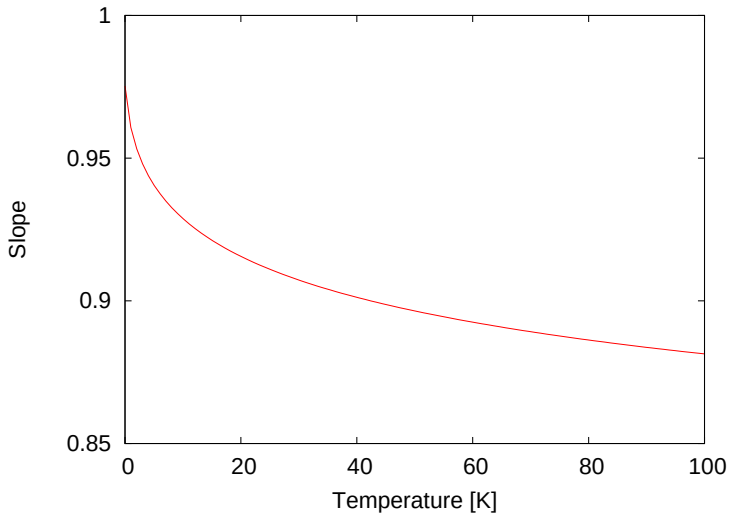

Figure 49: Slope of the broadening vs. shift curves as a function of temperature, as predicted by the theory in [143].

with a cut-off.

However, for the second order shift in Eq. (5.28) or in Eq. (5.35) does not have such a cut-off. If we fix the value of $\vec{k}_1$ and $\vec{k}_2$ in Eq. (5.28), the integrand in $\vec{k}_3$ is proportional to $U^2(|\vec{k}_1 - \vec{k}_3|)/k_3^2$, if k_3 is large compared to k_1 and k_2. This, in turn, results in an integrand in k_3, which is proportional to $U^2(|\vec{k}_1 - \vec{k}_3|)/k_3$, because the infinitesimal element $\vec{k}_3 = 2\pi k_3\, dk_3$. For $U(|\vec{k}_1 - \vec{k}_3|)$ =constant, the integral will have a logarithmic singularity, while for $U(|\vec{k}_1 - \vec{k}_3|) \sim |\vec{k}_1 - \vec{k}_3|^\eta$, the integral is proportional to $k_3^{2\eta}$, i.e., very strongly depends on the exact value of the upper bound. In physical terms, the difference between the second order shift and the broadening is that for the broadening, we have to satisfy energy conservation (c.f. Eq. (5.10), while for the the shift, the Dirac delta is replaced by the factor $(E_i - E_f)^{-1}$, which allows processes that violate energy conservation.

With this simple theory we could qualitatively explain why the luminescence line becomes broader as the density is increased, and in particular, it also demonstrates that the broadening coefficient does not tend to zero as the temperature diminishes, however, it does not give very good fits over all temperatures. This is the result of the simple premises; if

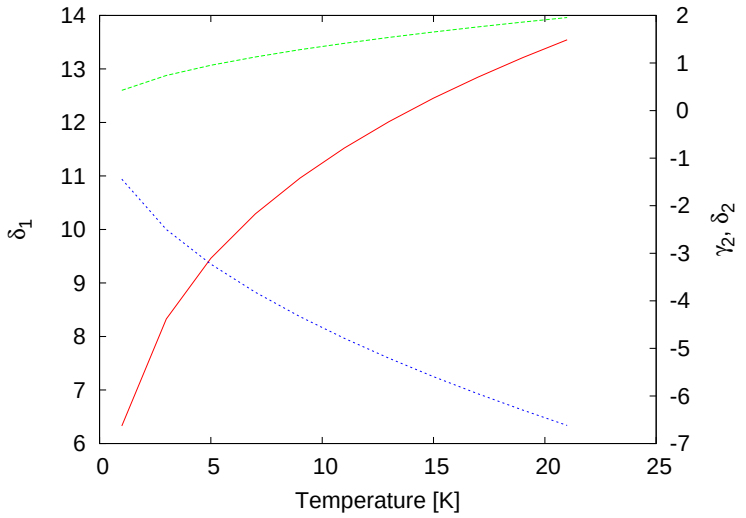

Figure 50: The coefficients δ_1, (left axis, red solid line), δ_2, and γ_2 (right axis, green and blue dashed lines) defined in Eq. (5.41) as a function of temperature. The potential is $U \sim \sqrt{k}$. The units are arbitrary.

we could derive the scattering amplitude $U(\vec{k}_1, \vec{k}_2, \vec{k}_3, \vec{k}_4)$ from first principles, and applied it instead of the simplistic approach that we discussed, the theory would be more accurate [147, 148]. As we pointed out above, in order for this perturbation approach to work, a cut-off must be defined, and if the proper potential provides us with this physical cut-off, then we expect better results. Also, we have treated only second order corrections, or, in other words, we summed over the simple loops only, and it might very well be the case that higher-order diagrams give significant corrections. Moreover, one might argue that the treatment of the temperature is not quite justified in this way, and that we should not use a zero-temperature perturbation theory for a finite-temperature system. We could then use a finite-temperature Green function method [149]. However, this is beyond the scope of this thesis.

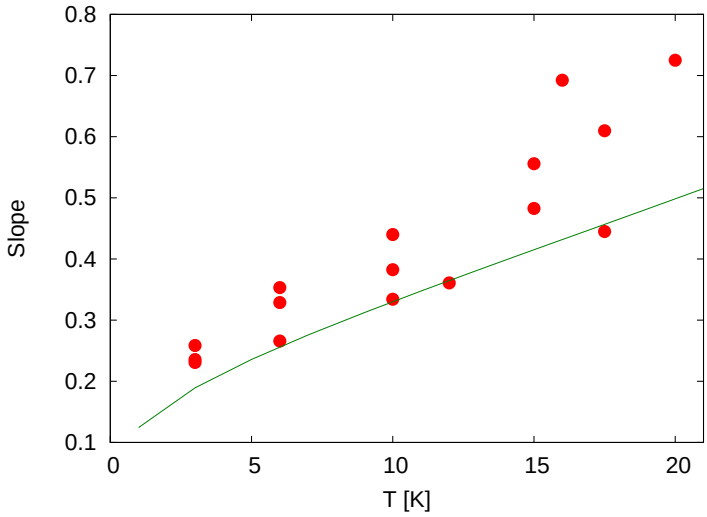

Figure 51: Line-broadening as a function of temperature as predicted by the theory above. The solid green is the theoretical dependence with $U \sim \sqrt{k}$, while the red points are the experimental data from Fig. 44. The dashed curve is the theoretical dependence with $U \sim k$.

6.0 QUANTUM WELL EXCITONS AT HIGH STRESS

In the introduction we pointed out that in these double quantum wells, the ground state of the excitons is dark (i.e., not coupled to light), and if a condensate is formed, it is expected to lead to a dark or reduced intensity region, where the ground state wave function is localized [30]. In this chapter we present preliminary data that seem to support the interpretation of a dark condensate.

6.1 BROKEN-SYMMETRY LUMINESCENCE AT HIGH STRESS

In this chapter, we will describe and analyze the excitonic luminescence at high stress, when the trapping potential is steep. We can also recall from the introduction that the threshold density for BEC, at least in the non-interacting case, is inversely proportional to the spring constant of the potential. Therefore, a steep trap favors a lower excitation density. In all experiments discussed here, we used a 120-Å double quantum well; however, these phenomena have been observed in 100-Å and 140-Å samples as well.

As the stressing force is increased, the depth of the trap increases, while its lateral size does not change considerably. This means that the trap becomes steeper and steeper. However, the depth of the trap cannot be increased indefinitely, and at a certain stress value, a sudden change occurs in the nature of the luminescence. This is shown in Fig. 52. When the stress is released, the luminescence recovers its original profile.

The spatial distribution at high stress has a four-fold symmetry in the diamond-shaped central region, and a two-fold symmetry in the two distinct lobes. The two-fold symmetry is already present in the low-stress case, because the luminescence profile is narrower along

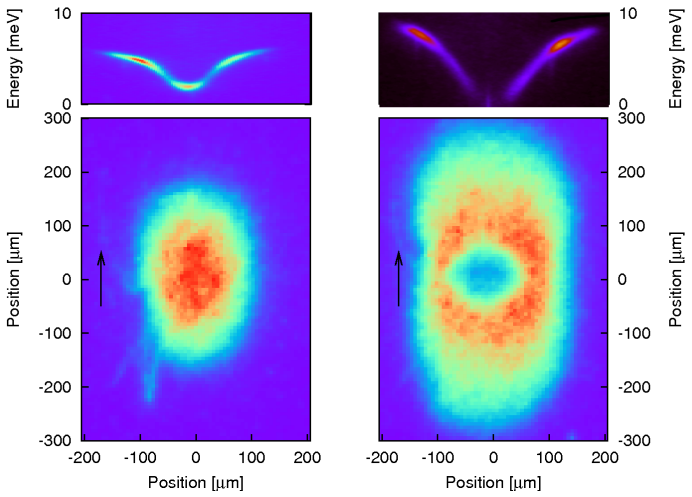

Figure 52: The profile of the trapping potential through its center at low stress (top left) and the corresponding spatial distribution (bottom left). On the right a similar profile and spatial distribution are shown for high stress. The small arrows indicate the direction of the [110] crystal axis.

the [110] crystal axis: the trapping potential seems to be stronger in one direction than in the one perpendicular to it. The breaking of the symmetry is not related to an imaging problem in the system, because if the sample is rotated along the [001] axis by a certain amount, the image of the spatial distribution is rotated in the same fashion. The strong axis of the trap is always perpendicular to the [110] crystal axis. One explanation of the two-fold symmetry might be that for technical reasons, the growth direction is not strictly parallel to the [001] crystal axis, but tilted by about 1° [88]. This is done on purpose, so that during the growth process there is a preferred orientation of the Ga/As atoms being deposited, because the atoms land on a set of terraces of planes perpendicular to [001]. If before the growth process the crystal is cleaved strictly perpendicular to [001], the atomic layers cannot assume an ordered state and the quality of the quantum wells will be poor, with large well-width fluctuations.

6.2 POSSIBLE REASONS FOR THE REDUCED LUMINESCENCE INTENSITY

The fact that at a particular point in space very reduced or no luminescence can be detected, does not necessarily mean that we have produced an excitonic condensate. Therefore, we have to inspect all possibilities carefully.

From the operational point of view, there are at least four possibilities that would explain the reduced luminescence intensity.

1. The first is that for some reason, not related to BEC, photon emission is inhibited at the place of high stress. Such could be a "break-down" of the crystal, i.e., if the deformation is so high that the crystal structure and symmetry completely changes and photon emission becomes prohibited.
2. The second is that the region of diminished luminescence acts as a sink for excitons, in which they disappear without a trace. This could be a very deep potential well, into which particles can fall. (In order to refute this scenario, we do not have to specify what would create such a deep potential well.)

3. The third possibility is that this region acts as a potential barrier, which the particles cannot scale, but flow around it.
4. And finally, this could be a puddle of dark excitons, either condensed into their ground state or occupying thermally excited states.

In the following, we will discuss the experiments we have conducted to confirm or refute the various possibilities. These are not all imaginable possibilities, and in order to prove that we have a BEC of excitons, further tests must be conducted. At this point, we can only rule out the first 3 options, but we do not have an unequivocal evidence for excitonic BEC, which would be the subject of future work.

6.2.1 Why not a structural change?

The first option can be ruled out by noting three features of the luminescence. The first is that any change in the crystal symmetry should be abrupt: the crystal either possesses a particular symmetry or it does not, but one would not expect a state in-between. Therefore, the intensity distribution should have a sharp cut-off at the boundary. But according to Fig. 53, the transition is not sharp.

We can also point out that the size of the reduced luminescence region depends on the excitation intensity, as it can be seen in Fig. 53. The only variable is the excitation power, all other parameters are kept constant. In order to exclude any stray light, the luminescence intensity was integrated between 1200 and 7900 ns after the beginning of the laser pulse (1000 ns long with a repetition period of 8000 ns), and a narrow band band-pass filter with a center wavelength of 820 nm and a full width of 10 nm was placed in front of the spectrometer [153]. The bias voltage was set to a value that resulted in an indirect exciton wavelength of 820 nm. The gating of the CCD removes the main laser pulse from the signal, while the band-pass filter prevents any background light from reaching the detector. As we can see in this figure, as the excitation intensity is reduced, the gap between the two luminescence peaks closes, and at the lowest power, it completely disappears. This, again, does not support the notion of any structural change in the crystal.

Finally, according to Fig. 54, the size of the hole depends on the applied external electric

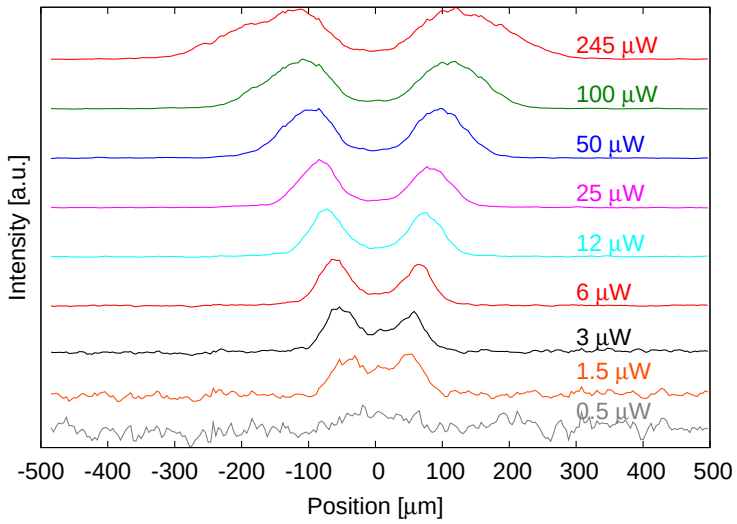

Figure 53: The dependence of the size of the reduced luminescence region on the excitation intensity. The spatial profiles are taken along a horizontal line across the center of the trap. All intensities are normalized to 1 at their respective maximum.

potential. The straight line fit through the maximum of the profiles has a slope different from infinity, which means that the size of the hole increases with the electric field. Keeping in mind that with increasing external potential the lifetime of excitons increases (C.f. Fig. 9), this also indicates that the more particles we have in the trap, the bigger the hole grows.

6.2.2 Why not a sink of particles?

This possibility is the easiest to rule out, if we observe that a sink takes particles out of the system, and therefore, it reduces the lifetime as deduced from the time dependence of the luminescence intensity. We therefore conducted a measurement in which excitons were created on the high side of the stress well, and the time evolution of the luminescence was measured in two cases: once when the stress was high enough to produce the black hole, and once when the stress was reduced to a value just before the appearance of the black hole, but all other conditions, such as excitation power and wavelength, temperature and

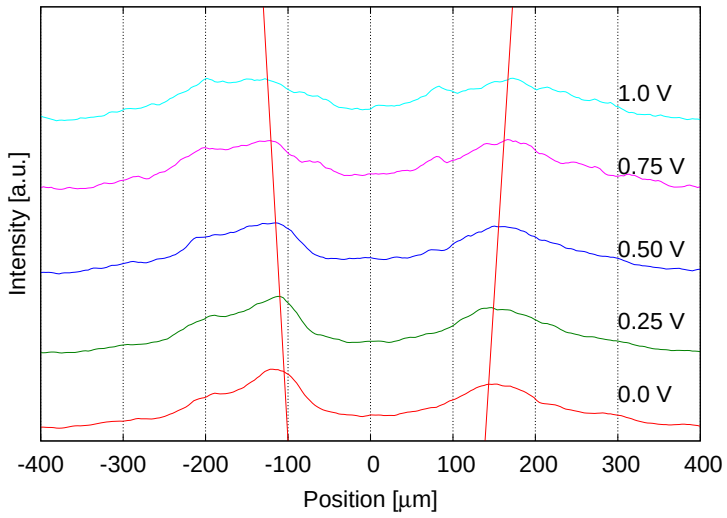

Figure 54: The dependence of the size of the reduced luminescence region on the applied electric field. The intensity is integrated spectrally over a range of about 7.5 meV. Also shown is a straight line fit through the maximum of the profiles.

bias voltage were kept the same. Contrary to the expected behavior of a sink, the lifetime slightly increases as the stress is increased beyond the appearance of the black hole, as shown in Fig. 55. This would be consistent with the particles being in a dark state, and slowly converting into bright ones.

Also, when particles are created on the side of the trap, they proceed downwards, but when they reach the vicinity of the hole, they seem to flow around it, as shown in the time evolution of the luminescence in Fig. 56. In this case, the narrow-band filter was not used, and the substrate luminescence at the laser spot can be seen as a small, bright spot. Interestingly, even though excitons are created on the right hand side of the line separating the two lobes, they flow around or through the center, and appear on the left hand side.

Finally, bright excitons can be created even when the laser is moved to the center of the trap, where the hole is. They do not appear till they cover some distance from the center. All this indicates that we are dealing with a type of barrier at the center, and not a sink.

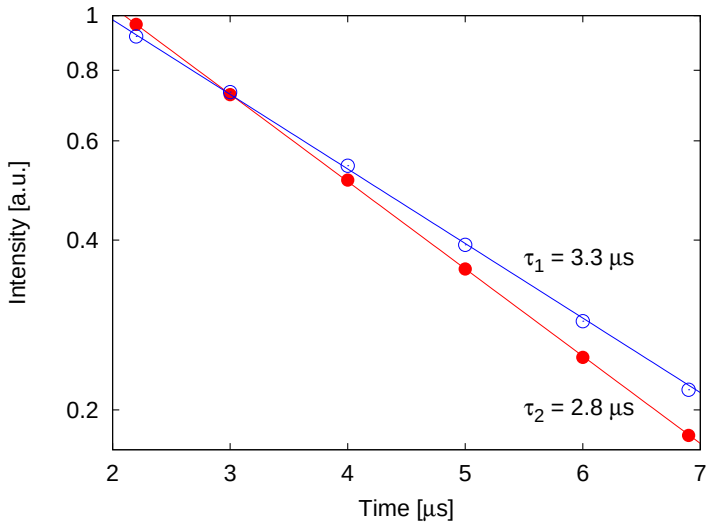

Figure 55: Comparison of the lifetime of excitons in two different cases: once with moderate stress, when the trap is uniform (solid red circles), and once with high stress, when the trap shows a black hole at the center (open blue circles).

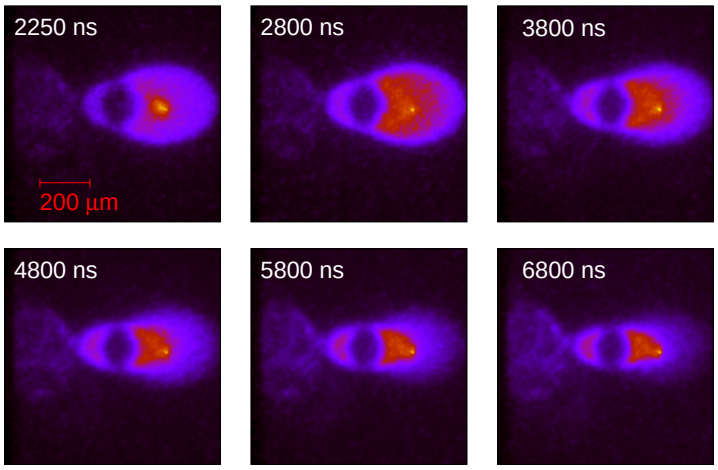

Figure 56: Time sequence of bright excitons flowing around the hole. The spontaneous light of the laser was not filtered spectrally, and it shows up as a small, bright spot on the pictures.

6.2.3 Why not a structural barrier?

The case of a structural barrier can be discarded on the same ground as that of structural change in the symmetry: the size shows a very clear power dependence, which indicates that the size is related to the very particles that are created by the light.

At this point, we are left with the fourth possibility, namely, that dark particles of some kind play a role.

6.2.4 Power dependence and temperature dependence

We also investigated the temperature and power dependence of the reduced luminescence region. By changing the temperature, we could introduce changes in the applied stress, for the thermal expansion coefficients of the various parts in our apparatus can be different, resulting in a different thermal expansion as the temperature is changed. To avoid this, we re-applied the stress after changing the temperature. In order to produce the same stress at a different temperature, we measured the compression of the spring from the point when the pin touched down on the sample. (This point can easily be identified, because both the pin and the substrate are conducting, and we only need to prove that we have electrical contact between two points.) In this particular case, the compression was 60 μm, although, without the knowledge of the Hooke constant of the spring, it is only a reference number, indicating that we have the same external stress.

Fig. 57 shows how the character of the reduced luminescence region depends on temperature. The pulsed diode laser is tuned to the direct resonance at 808 nm, and the luminescence is integrated over time, except for the period when the laser pulse is on. Spectral filtering is applied as well. As seen, at high temperatures, the luminescence originates from a single region, and as the temperature is lowered, two lobes develop. At the same time, the difference between the intensity minimum and maxima along either a vertical or a horizontal cut becomes deeper.

The size of the hole also depends on the excitation power, which, again, points to a underlying reason different from a structural transition. This is shown in Fig. 58 where the temperature was fixed at 2 K, and the bias of the diode laser tuned to the direct exciton

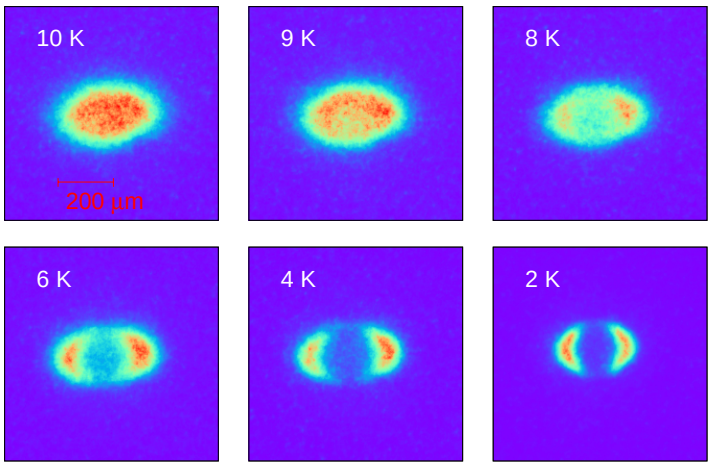

Figure 57: The temperature dependence of the luminescence when the applied stress is high. The laser is gated and all light outside of the range of interest is spectrally filtered. The excitation power is 400 μW.

resonance at 808 nm was turned up to increase the excitation power.

On one hand, at high temperatures the modulation decreases, while on the other hand, increasing the pump power develops higher modulation. We can, therefore, try to find the critical power for each temperature at which the modulation in the intensity distribution appears. The results for two fixed stresses are summarized in Fig. 59. At each temperature and stress, the pump power was increased till an intensity dip appeared at the center of the luminescence. The excitation was continuous, except for a short time when the integration was done. The error bars were deduced as the difference between the highest power without the dip and the lowest power with the dip. Since this definition is subjective to some degree, these are only indicative values.

When interpreting the results, we have to keep in mind that, as the temperature is increased, the lifetime of excitons becomes longer (C.f. Fig. 11.). Since here we have an almost continuous excitation, this also means that at higher temperatures we have more particles for the same pump power, for in the steady state, the radiative recombination keeps

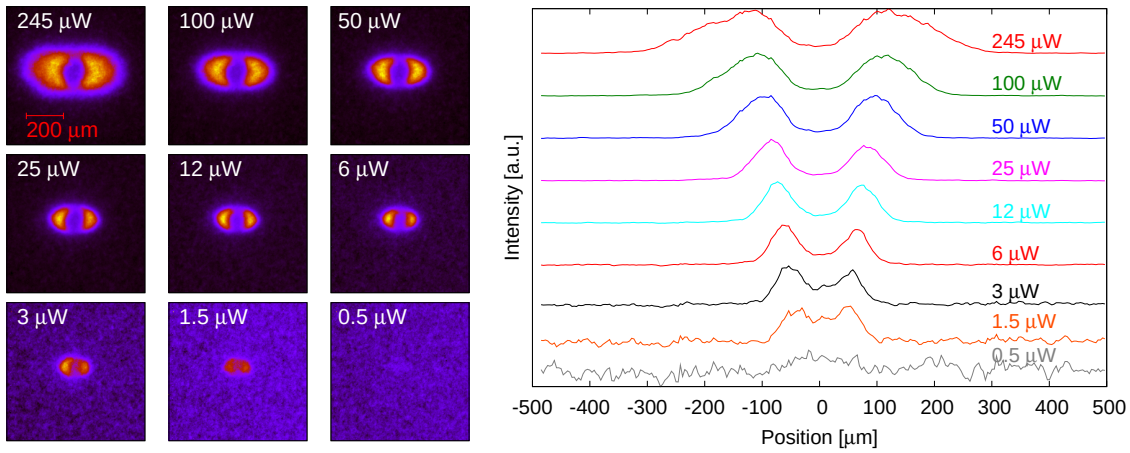

(a) (b)

Figure 58: The power dependence of the luminescence when the applied stress is high. The laser is gated and all light outside of the range of interest is spectrally filtered. The temperature is 2 K. a) shows the direct images, while the profiles in b) were taken along a horizontal line through the center of the trap.

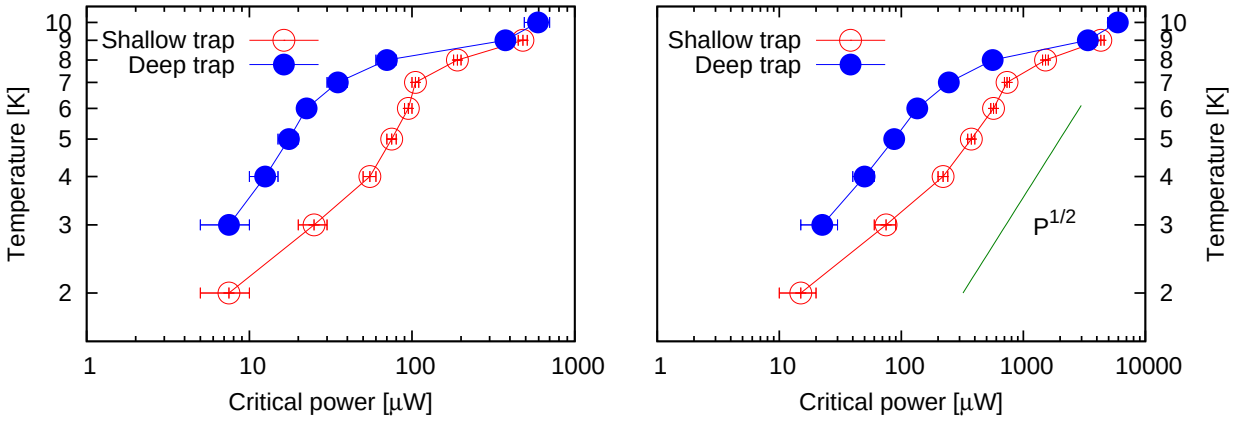

Figure 59: The connection between the critical power and the temperature. The lower curve belongs to the lower stress. The left hand side shows the raw data, while on the right hand side, we plot the corrected dependence as discussed in the text. The straight line is $\sim \sqrt{n}$. The lines are guides to the eye.

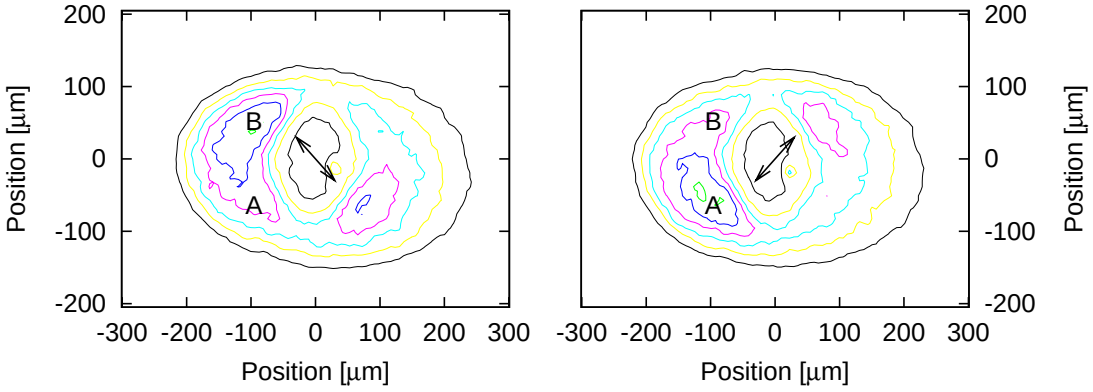

Figure 60: Intensity distribution of exciton luminescence when the polarizer is at $-45°$ (left) and $+45°$ with respect to the vertical direction. The small arrows show the orientation of the polarizer. The laser is gated and all light outside of the range of interest is spectrally filtered. The excitation power is 430 μW.

balance with the pumping. Denoting the generation term by G, the differential equation for the exciton population is

$$0 = \frac{\partial n}{\partial t} = -\frac{n}{\tau(T)} + G \ , \tag{6.1}$$

i.e., $n = G\tau(T)$. Assuming that the lifetime is linear in the temperature as in Eq. (1.32) and in Fig. 11, we can adjust the number of particles accordingly. This adjustment is also shown in Fig. 59. For comparison, we also plot $\sqrt{n}$, which, according to Eq. (1.5), would be the expected dependence in the non-interacting case.

6.2.5 Polarization of the luminescence

In Fig. 60 we show the intensity distribution for two settings of a polarizer in front of the spectrometer. These two distributions, taken at an angle of $-\pi/4$ and $+\pi/4$ with respect to the vertical, clearly show dependence on polarization, for in one case (left hand side) the intensity maximum is located at the top-right and bottom-left directions, while in the other (right hand side), they are flipped to the other side.

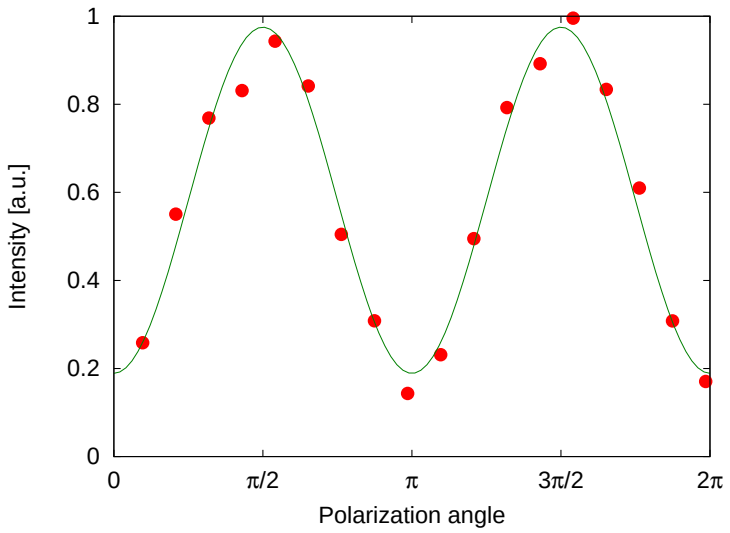

Figure 61: Intensity of a non-polarized white light source as a function of the polarizer angle.

When interpreting these intensity plots, we have to be more careful, though, because the spectrometer contains a diffraction grating, therefore, it acts as a polarizer itself [154]. This means that we have to adjust the intensities accordingly, where the normalization function can be obtained by measuring the intensity of a non-polarized light source, as the polarizer is turned. This is shown in Fig. 61. It is clear that the spectrometer has a strong polarization dependence, and that we have to normalize the measured intensities with this function.

With this normalization, the intensities of points A and B in Fig. 60 are plotted as the polarizer is turned over an angle of π. In Fig. 62, we can see that the luminescence at those two points is indeed polarized in different directions.

These results can be made more quantitative, if we assume that the intensity changes as

$$I(\phi) = I_0 \sin^2(\phi + \phi_0) + I_{bg} \ , \tag{6.2}$$

where I_{bg} is the "background" intensity, I_0 is the modulation, and ϕ_0 is the direction of the polarizer. A fit to this function is also shown in Fig. 62. With the parameters above, the visibility is defined as $I_0/(I_0 + I_{bg})$, which coincides with the standard definition $(I_{max} -$

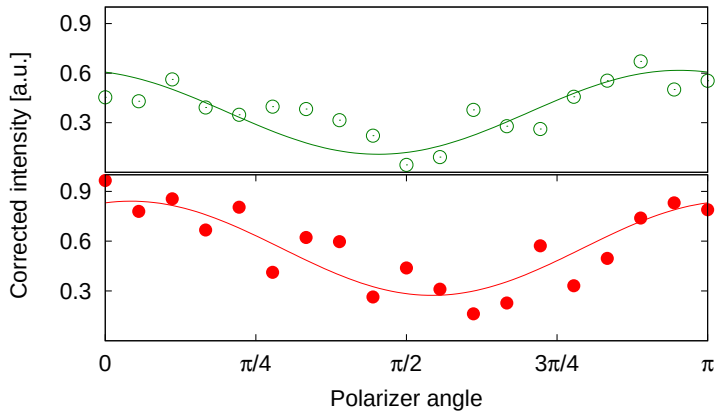

Figure 62: Intensity at point A (open circles) and B (solid circles) in Fig. 60, as the polarizer is turned through an angle of π. The inherent polarization of the spectrometer is already factored out using the results of Fig. 61. Also shown are fits to the function in Eq. (6.2). The laser is gated and all light outside of the range of interest is spectrally filtered. The excitation power is 430 μW, and the contours show the total intensity.

$I_{min})/(I_{max} + I_{min})$.

A complete map of the polarization can be seen in Fig. 63 for two cases. The right hand side of the figure shows the case, when the stress is relatively low, and the intensity distribution is uniform, while the left hand side gives the polarization, when the stress is high and the luminescence from the central region is inhibited. The direction of the polarization axis was deduced from fits to the function in Eq. (6.2), and their length is proportional to the visibility defined above. In order to relate the polarization to the position of the exciton distribution, we also plot the topographic levels of the luminescence at the angle of maximum transmittance. This is simply equal to the modulation in Eq. (6.2). From the figure, both the relative modulation and the direction of the polarization changes when the stress is increased. We should point out here that Fig. 62 shows the corrected intensities, i.e., the polarization of the spectrometer is factored out, while in Fig. 60 gives the raw data, without any correction. This is why the polarization shift in Fig. 62 is not $\pi/2$, as it would be inferred from Fig. 60 alone.

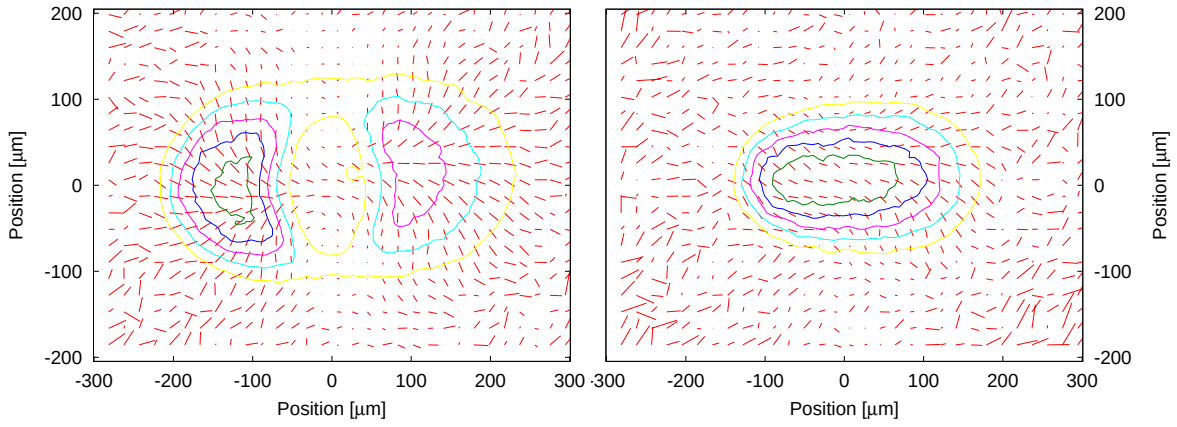

Figure 63: Polarization map of the luminescence for high (left) and for low stress (right). The direction of the vectors gives the polarization direction, while the length is proportional to the visibility. The topographic contour lines are the levels of the intensity at the corresponding polarization maximum, i.e., the value of I_0 in Eq. (6.2).

The polarization of the light emission in itself is not very surprising, and it has been observed in papers where the propagation of light in the *plane* of the quantum wells was studied [155, 156], although in our case the ligth propagates in a direction perpendicular to the quantum wells. The change in polarization can be attributed to the fact that, as stress is applied, the symmetry of the crystal changes, which leads to a splitting of the two bright states. When k_BT is smaller than this splitting, the two states will have unequal occupation.

6.3 THEORETICAL CONSIDERATIONS

We can try to model some of the experimental findings without any reference to a condensate, in fact, assuming that the gas is in the classical regime.

We will presume that we have a dark and a bright exciton population, and that they are energetically separated. Due to the interaction between particles, the potential is renormal-

ized. The renormalization is proportional to the *total* number of particles, i.e., we have to consider both populations for both potentials. Therefore, we can write

$$\tilde{V}_b(r) = V_b + \gamma(n_b(r) + n_d(r)) \tag{6.3}$$

$$\tilde{V}_d(r) = V_d + \gamma(n_b(r) + n_d(r)) \ , \tag{6.4}$$

where $V_{b,d}(r)$ are the external trapping potentials for the bright and dark excitons, respectively, and $n_{b,d}(r)$ are the bright and dark exciton distributions. The repulsion coefficients, γ, can be different in the two cases, although we will only investigate the simple case when it is the same for both types of particles.

Then we also assume that the distributions follow the Boltzmann statistics, i.e.,

$$n_b(r) = Ae^{-\beta\tilde{V}_b(r)} = Ae^{-\beta(V_b(r)+\gamma(n_b(r)+n_d(r)))} \tag{6.5}$$

$$n_d(r) = Ae^{-\beta\tilde{V}_d(r)} = Ae^{-\beta(V_d(r)+\gamma(n_b(r)+n_d(r)))} \ . \tag{6.6}$$

By dividing the two equations, we get

$$n_b(r) = n_d(r)e^{-\beta(V_b(r)-V_d(r))} \ , \tag{6.7}$$

which we can substitute into the equation for $n_d(r)$, to obtain

$$n_d(r) = A\exp\left[-\beta(V_d(r) + n_d(r)\gamma(1 + e^{-\beta(V_b(r)-V_d(r))})\right] = A\exp\left[-\beta(V_d(r) + n_d(r)g(r))\right] \tag{6.8}$$

with the definition

$$g(r) = \gamma(1 + e^{-\beta(V_b(r)-V_d(r))}) \tag{6.9}$$

Eq. (6.8) is a self-consistency equation for $n_d(r)$ (and thus, for $n_b(r)$), which we solve numerically for various values of A.

For the potential, we will take two Gaussians with the same width, and for numerical reasons, we define them as

$$V_b(r) = V_d^0 + V_{sp} - V_b^0\exp(-x^2/2\sigma^2) \tag{6.10}$$

$$V_d(r) = V_d^0(1 - \exp(-x^2/2\sigma^2)) \ . \tag{6.11}$$

This guarantees that they have a splitting as the position tends to infinity, as we would expect for the stress-free case from the theoretical considerations in Chapter 1.

Fig. 64 shows the numerical solution for the exciton distributions with a splitting of 1 meV at two temperatures, 2 and 8 K, respectively. In both cases, the particle number is 10^5 and $\gamma = 0.01$ meVμm^2. At low temperature, the distribution of the bright excitons has a pronounced minimum at the center, which disappears as the temperature is raised. This can be understood, if we notice that, as the temperature becomes comparable to the splitting, the thermodynamic difference between the two kinds of excitons disappears.

We can also demonstrate that this model would, at least qualitatively, account for the power dependence of the luminescence intensity. In Fig. 65 we plot the numerical solution for two densities, different by a factor of 10, while keeping all other parameters constant.

These results assume a classical distribution of excitons. To get distributions which look like the data, very large splitting (1 meV) must be chosen, which, in turn, implies very few excitons in bright states. This suggests that Bose degenerate statistics should be taken into account. Of course, the model could be refined in a number of ways. E.g., it is not a trivial question whether the interaction potential between the different exciton species can be taken as equal. We do not account for the two-fold symmetry in the luminescence either, as we have not said anything about the polarization.

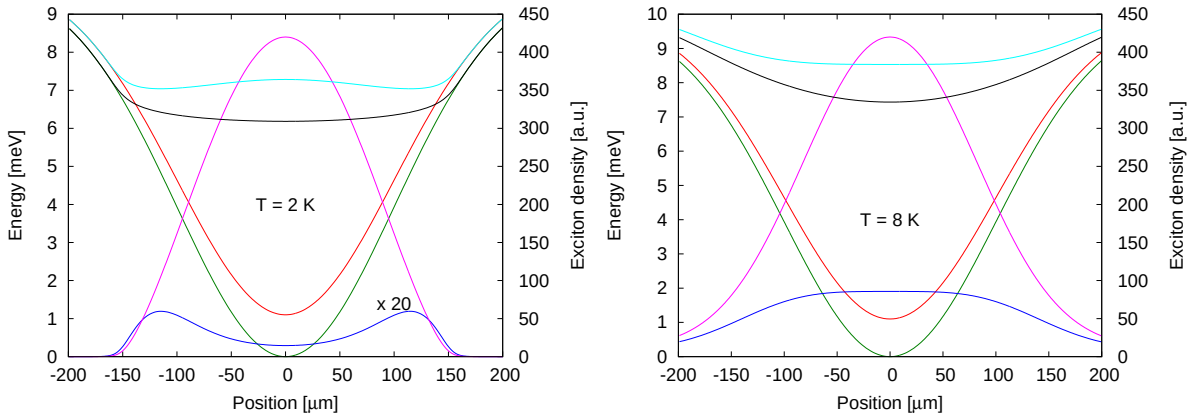

(a) Low temperature

(b) High temperature

Figure 64: The distribution of the dark (purple) and bright (dark blue) excitons in a renormalized trap. The bare trap is shown in green for the dark excitons and in red for the bright excitons, while black is the renormalized trap for the dark excitons and light blue for the bright excitons. The low-temperature case is on the left, while the right hand side shows the high temperature distributions. In a), the bright exciton density is multiplied by 20 for clarity.

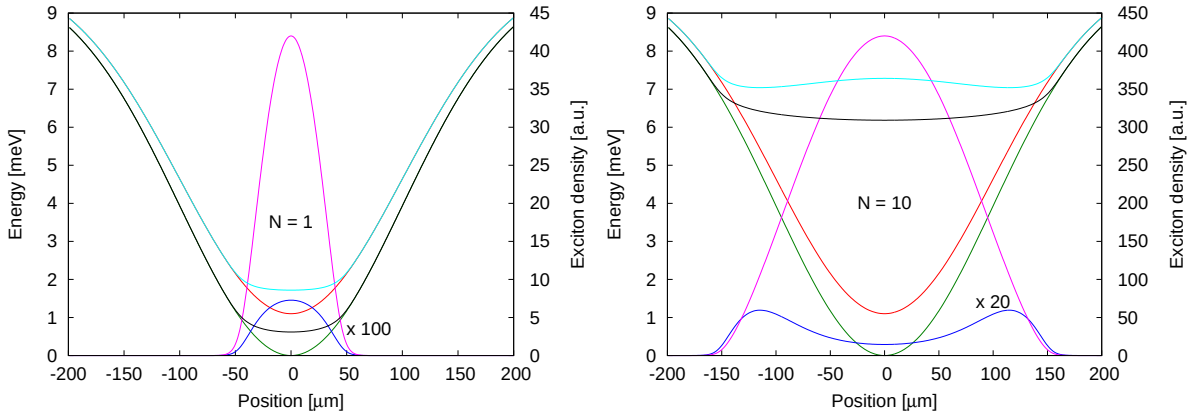

(a) Low density

(b) High density

Figure 65: The distribution of the dark (purple) and bright (dark blue) excitons in a renormalized trap for the low density (left) and high density (right). The bare trap is shown in green for the dark excitons and in red for the bright excitons, while black is the renormalized trap for the dark excitons and light blue for the bright excitons. In a), the bright exciton density is multiplied by 100, while in b) by 20 for clarity.

7.0 CONCLUDING REMARKS

The motivation of this work was to study exciton dynamics and interaction in coupled quantum well systems. The bosonic nature of excitons naturally lends them to investigations related to Bose-Einstein condensation. We have pointed out that the question of equilibrium excitonic BEC is still not settled, neither theoretically, nor experimentally. From the theoretical point of view, the exact form of the exciton-exciton interaction is still debated, while on the experimental side, it is not clear what exactly the signatures of an excitonic BEC would be. On the other hand, even without proving or disproving an excitonic BEC, we have established major milestones, such as the fact that excitons move freely in the quantum wells and that they can be trapped, and we have discussed two trapping methods at length. We also studied their interaction under controlled conditions and pointed out what would require further theoretical work to understand the findings.

In the last part of the thesis, we discussed recent, and not yet explained results on exciton luminescence at high stress. We cannot rule out the possibility that these might be a dark condensate, and there are a few facts in favor of this argument. This certainly poses both theoretical and experimental challenges for the years to come: the interaction of a dark condensate and the surrounding bright exciton population must be understood; if this is indeed a condensate, then proper a test must be developed to prove it.

It is not trivial to prove anything about an invisible object in an optical measurement, and there seems to be no other method of accessing excitons but optical. All is not lost, however. Applying an in-plane magnetic field (Voigt configuration) mixes the bright and dark excitons, thus providing an indicator for the dark population [157, 158]. This is a standard measurement in quantum dots [159].

Superfluidity of excitonic bilayer systems in an in-plane magnetic field has been predicted

in the work of Balatsky et al. [160]. We have demonstrated that these coupled quantum wells are indeed clean in terms of excitonic transport, thus they would provide an excellent test bed for those ideas.

APPENDIX

MODELLING EXCITONS IN QUANTUM WELLS

In this appendix we discuss a model to account for the experimental findings in Chapters 2 and 3, and in the final part, we show how the interaction of particles modifies the simple condition Eq. (1.5) for excitonic BEC.

A.1 DIFFUSION IN A PLANE POTENTIAL

In Chapter 2, we pointed out that excitons move in the plane of the quantum wells in a diffusive process. Therefore, our starting point will be a diffusion equation. However, in addition to a standard diffusion equation, several other factors have to be taken into account.

1. First, excitons have a finite lifetime, therefore, in the equation describing the population evolution we will have a term which is equal to the local density, $n(\vec{r})$, divided by the radiative lifetime, τ..

2. Excitons also repel each other. We can model this as a potential generated by the particles, and in the first approximation, we take the potential to be linear in the density. We have shown in Chapter 5 that this linear approximation is a valid one over a wide range of particle densities, and deviations from the linear dependence can be expected at high densities only. All the diffusion measurements were conducted at low densities.

Writing the generated potential as

$$U(\vec{r}) = \gamma n(\vec{r}) \ , \tag{.1}$$

the resulting force is

$$\vec{F}(\vec{r}) = -\gamma \nabla n(\vec{r}) \ . \tag{.2}$$

3. Finally, excitons are generated, which adds a generation term, $G(t)$, to the diffusion equation.

With these considerations, the exciton population obeys the equation [124, 131]

$$\frac{\partial n(\vec{r})}{\partial t} = \nabla(D\nabla n(\vec{r})) + \frac{\tau_0}{m}\nabla(\gamma n(\vec{r})\nabla n(\vec{r})) - \frac{n(\vec{r})}{\tau} + G(t) \ , \tag{.3}$$

where τ_0 is the scattering time [59]. The term $\nabla(\gamma n(\vec{r})\nabla n(\vec{r}))$ is the dipole current due to the potential generated by the interaction of excitons.

We have not yet specified the diffusion constant, D. According to a couple of papers by Ivanov [86, 152], the overlap of the wavefunctions of particles modifies the diffusion constant, and then it will be related to the mobility, μ, through the equation

$$\mu = D\frac{e^{T_0/T} - 1}{k_B T_0} \ , \tag{.4}$$

where $T_0 = (2\pi\hbar^2 n(\vec{r}))/(k_B g m)$ is the degeneracy temperature with an exciton degeneracy of $g = 4$ in our case. It is worth noting that in the high temperature case, when $T \gg T_0$, we recover the usual Einstein relation,

$$\mu = \frac{D}{k_B T} \ . \tag{.5}$$

This happens in the temperature range where quantum mechanical effects are not important.

Moreover, the diffusion constant, D, is the result of all the relevant scattering mechanisms, which are exciton-exciton scattering at high density (D_x), interface roughness scattering (D_{RS}) at low density, and exciton-phonon scattering, which is the slowest of all. Thus the diffusion constant is given by $D = 1/(1/D_x + 1/D_{\mathrm{RS}})$, and takes the limiting values $D = D_x$ for high, and $D = D_{\mathrm{RS}}$ for low density, neglecting the exciton-phonon scattering. Since we were interested in the late-time behavior, we do not derive D_x.

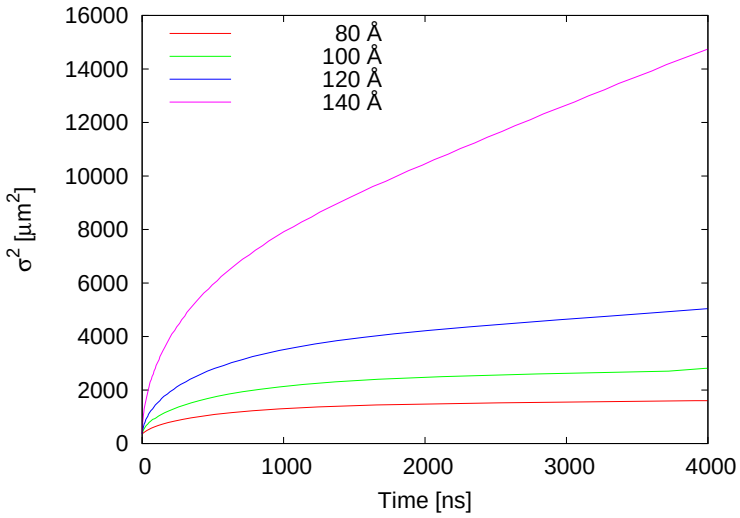

Figure 66: Time-evolution of the square of the size of the exciton cloud as predicted by the model above. All parameters are estimated from experimental results.

Fig. 66 shows the square of the variance of the numerical solution of Eq. (.3) with initial and boundary conditions consistent with the experiments, i.e., the generation term is

$$G(\vec{r},t)\Delta t = \begin{cases} 10^{11}\exp(-r^2/s\sigma^2)\ 1/\mathrm{cm}^2\ , & t=0 \\ 0\ , & t\neq 0 \end{cases} \tag{.6}$$

where $\sigma = 15\ \mu$m is a typical value from experiments, c.f. Fig. 15, and an initial density of $10^{11}\ 1/\mathrm{cm}^2$ corresponds to an excitation power of about 60 μW at 4 μs repetition rate. Δt is the time step in the numerical integration. The limiting values of the diffusion coefficient are 0.24, 0.74, 2.08, and 9.04 cm^2/s for the four quantum wells.

Initially, when the density is high and localization effects are not relevant, the importance of the repulsion can be measured by the ratio of the diffusion current to the dipole current,

$$\zeta = \frac{J_{dp}}{J_D} = \frac{n\gamma e^{T_0/T} - 1}{k_B T_0}\ . \tag{.7}$$

When $\zeta \geq 1$, the expansion of the exciton cloud is driven by the repulsive forces, and for $\zeta \leq 1$ the expansion is diffusive. Initially, the value of ζ is of the order of a couple of hundred.

This explains the very fast initial rise time in Fig. 16. As the exciton cloud increases in size and the density drops, ζ tends to zero, and pure diffusion sets in.

We mentioned in Chapter 3 that the temperature of the exciton gas changes in time, and initially it is much higher than that of the lattice. This affects both the lifetime and the diffusion constant. Rapaport et al. [131] and Hammack et al. [95] refined this model by accounting for the change in temperature, but the character of the time evolution does not change considerably, and the main conclusions are the same.

Since in the low-density case the diffusion coefficient becomes a constant, in order to account for the localization at very late time or very low densities, we have to modify the model above. We opted for the simplest solution, inserting a threshold density for diffusion, i.e., setting $D = 0$, if $n(\vec{r}) < n_0$. Physically, this would correspond to the picture that there is a given number of small traps, which inhibit the movement of particles, but they can accommodate only a finite number of excitons, because as the particle number is increased in these local minima, the inter-particle repulsion renormalizes the traps, and this prevents newer and newer particles from becoming trapped.

Fig. 67 shows how the introduction of the threshold density changes the late-time behavior of the excitonic expansion. Apart from the relatively sharp transition between the two regions, the solution indeed reproduces the experimental results.

A.2 DIFFUSION IN A STRESS TRAP

The only place where the presence of the trap modifies the model above is in the drift term in Eq. (.3), where we have to add the external potential, which we can take in the form $U(\vec{r}) = \alpha r^2/2$. All other terms are unaffected. Solving for this case gives results similar to that in Fig. 68. It is important to note here that the size dictated by the spring constant and the bath temperature would be $\sigma^2 \approx 600\ \mu\text{m}^2$ in this case, while the calculated size is around $\sigma^2 \approx 1800\ \mu\text{m}^2$. Therefore, we can account for the apparent high temperature in this model.

Fig. 69 shows the effective temperature given in Eq. (3.15) as a function of the exciton

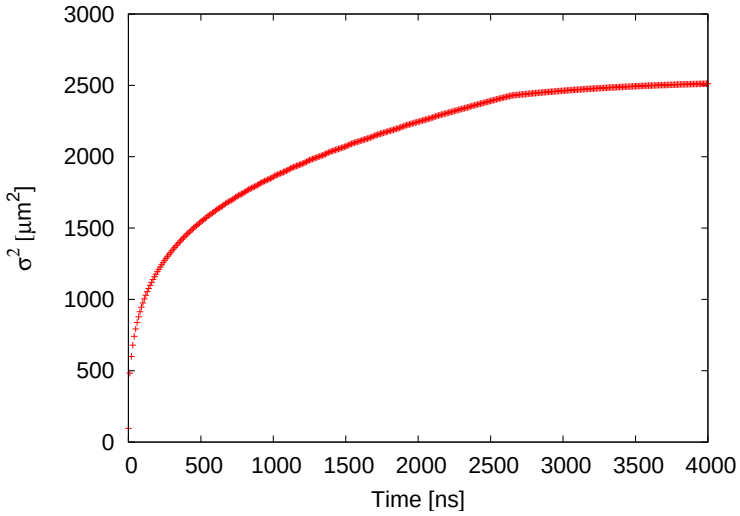

Figure 67: Time-evolution of the square of the size of the exciton cloud with a low threshold density, $n_0 = 10^8$ cm^{-2}.

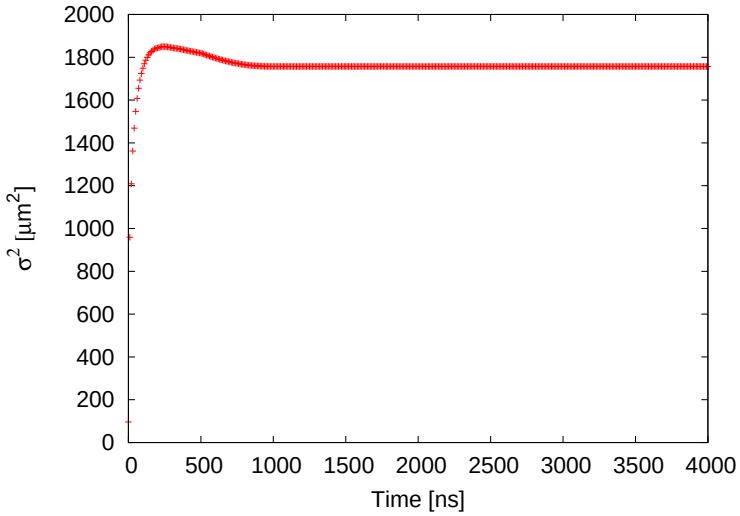

Figure 68: Time-evolution of the square of the size of the exciton cloud with a low threshold density, $n_0 = 10^8$ cm^{-2}, and a spring constant of 30 eV/cm^2. The bath temperature is 2 Kelvin.

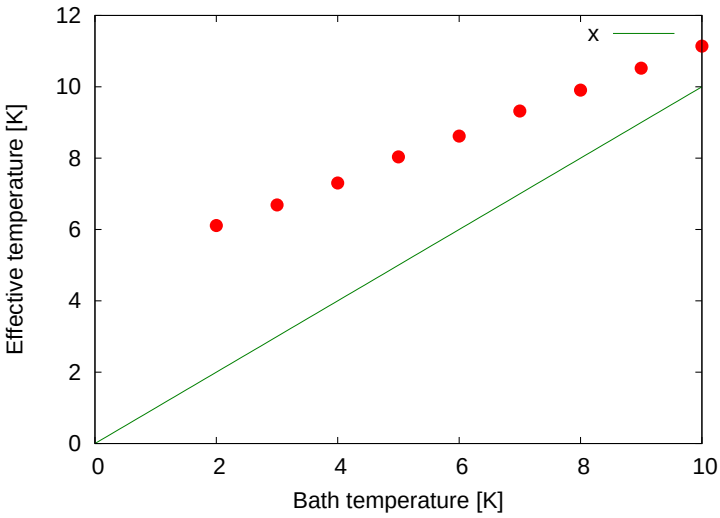

Figure 69: The temperature determined from the size of exciton cloud as a function of the bath temperature. The threshold density is $n_0 = 10^8$ cm^{-2}. Also plotted is the linear relation giving the bath temperature.

temperature. As the bath temperature is increased, the two temperatures seem to converge to the same value.

We can understand this behavior in the following way: when created, excitons repel each other, and are pushed high in the external potential. When the density drops, some of them become localized at those high potential value points, and cannot obey the restoring force of the trap. This is more apparent at low temperatures, where the final size is smaller.

A.3 BOSE-EINSTEIN CONDENSATION OF STRONGLY INTERACTING PARTICLES

In the introductory chapter we derived a relation for the critical number of particles in a harmonic potential. There we assumed that the interaction is weak, and the presence of particles does not modify the trap itself. However, in Chapter 5, we have seen that the

trap is significantly modified as the density increases. Therefore, it is an important question to ask what particle density or distribution a particular trap can support without being completely destroyed, and what effect it has on the critical number.

What makes the problem at hand difficult is the vast separation of energy scales that we have to consider. In a typical, not renormalized trap, the harmonic oscillator levels are $\Delta E = \hbar\omega_0 = \hbar\sqrt{\alpha/m_{\rm ex}} \approx 0.3$ μeV apart. (As the trap becomes renormalized, ω_0 tends to 0.) At the same time, the temperature is of the order $T \approx 2$ K, i.e., roughly 100 μeV. This also means that a semiclassical approach can be applied, including many excited harmonic oscillator states. Finally, the interaction changes the shape of the trap, and lifts its bottom by several meV.

The effect of interaction on the condensate has long been studied theoretically [150], and is described by the Gross-Pitaevskii equation. In that case, the renormalization of the external potential is taken into account by adding a term which is proportional to the square of the ground state wavefunction. We will use the same idea. The difference is that here we have to consider many states, because the thermal energy is large compared to the oscillator energies. With this modification, as in the case of the Gross-Pitaevskii equation, the potential is written as

$$V(\vec{r}) = V_0(\vec{r}) + \sum_\alpha \frac{|\Psi_\alpha(\vec{r})|^2}{e^{\beta(\epsilon_\alpha - \mu)} - 1} \ , \tag{.8}$$

where the chemical potential is fixed by the condition

$$N = \sum_\alpha \frac{1}{e^{\beta(\epsilon_\alpha - \mu)} - 1} \tag{.9}$$

and ϵ_α is the energy eigenvalue belonging to the Ψ_α eigenstate. The particle density is simply the sum of the expectation values of the field operators,

$$n(\vec{r}) = g \sum_\alpha \frac{|\Psi(\vec{r})_\alpha|^2}{e^{\beta(\epsilon_\alpha - \mu)} - 1} \tag{.10}$$

Here we explicitly take the degeneracy of each state into account in the prefactor g.

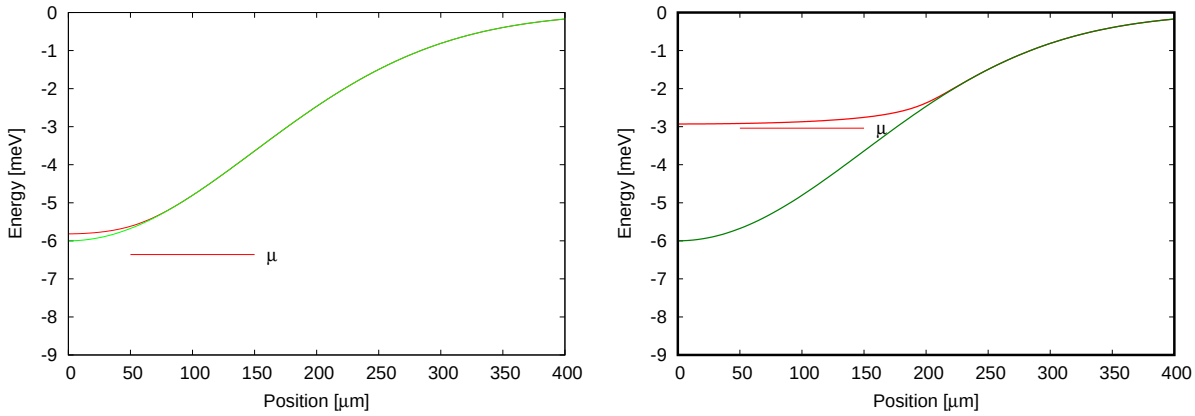

(a) Low density (b) High density

Figure 70: The renormalization of the potential at low (left) and high (right) densities. The green lines give the external potential, while the read lines are the renormalized potentials. The short red lines show the corresponding chemical potential.

In order to simplify the situation, we take a semiclassical approach, and for the various $\vec{k}$ states we use plane waves which are local, i.e., which are zero whenever the potential energy exceeds the eigenvalue $\epsilon_{\vec{k}}$ [9, 151]. Therefore, the particle density can then be expressed as

$$n(\vec{r}) = -n_{th} \ln\left(1 - e^{-\beta(V(\vec{r})-\mu)}\right) \ , \tag{.11}$$

where $n_{th} = gm/(2\pi\hbar\beta)$. Eqs. (.8),(.9) and (.11) determine the particle distribution and the chemical potential for any given N and external potential $V(\vec{r})$.

Figs. 70a,70b show the solution for the renormalized trapping potential at low and at high density, as given by the model discussed above. The repulsion coefficient was equal to the measured value $\gamma = 1.5 \cdot 10^{10}$ meV cm^2, and the number of particles is $N = 10^5$ and $N = 10^7$, respectively, while the external temperature is 2 Kelvin.

Fig. 71 shows the dependence of the chemical potential and the renormalization of the trap at its center as a function of the total number of particles. What we see is that both the chemical potential and the external potential increase as we place more and more particles in the trap. Bose-Einstein condensation would set in when those two energies are equal.

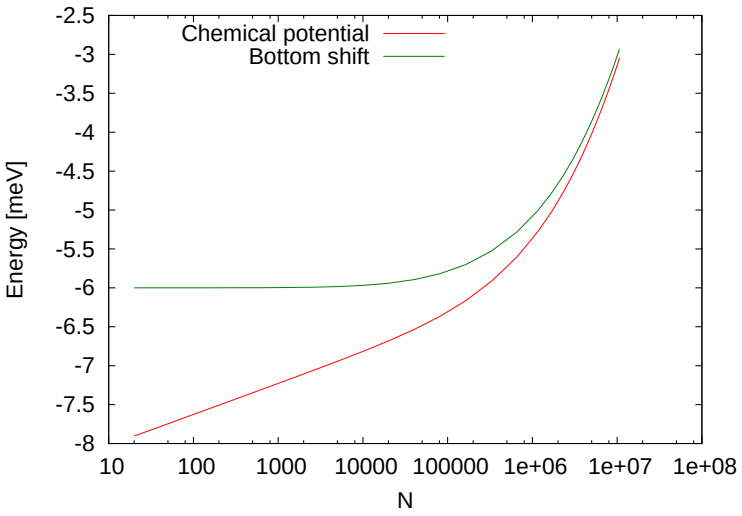

Figure 71: The renormalization of the potential and the chemical potential as a function of the total particle number in the trap.

According to the figure, this should happen somewhere around $N = 10^7$, or in terms of the blue-shift, somewhere around 3 meV. Although, we have seen such high shifts, we have not observed signatures of BEC. It might mean that the condensation happened in a dark state as discussed in previous chapters, or that we have tried to stretch this model well beyond its validity range.

BIBLIOGRAPHY

[1] T.R. Sosnick, W. M. Snow, and P.E. Sokol, Phys. Rev. B **41** 11185 (1990).

[2] K.B. Davis, M.-O. Mewes, M.R. Andrews, N.J. van Druten, D.S. Durfee, D.M. Kurn, and W. Ketterle, Phys. Rev. Lett. **75** 3969 (1995).

[3] M.H. Anderson, J.R. Ensher, M.R. Matthews, C.E. Wieman, and E.A. Cornell, Science **269** 198 (1995).

[4] H. Deng, G. Weihs, C. Santori, J. Bloch, and Y. Yamamoto, Science **298** 199 (2002).

[5] H.S. Deng, G.S. Solomon, R. Hey, K.H. Ploog, and Y. Yamamoto, Phy. Rev. Lett. **99** 126403 (2007).

[6] J. Kasprzak, M. Richard, S. Kundermann, A. Baas, P. Jeambrun, J. M. J. Keeling, F. M. Marchetti, M. H. Szymańska, R. Andr, J. L. Staehli, V. Savona, P. B. Littlewood, B. Deveaud, and Le Si Dang, Nature **443** 409 (2006).

[7] R. Balili, V. Hartwell, D. Snoke, L. Pfeiffer, and K. West, Science **316** 1007 (2007).

[8] P. Noziéres in *Bose-Einstein condensation* Eds. A. Griffin, D.W. Snoke, and S. Stringari, Cambridge University Press 1995.

[9] R. Zimmermann, Sol. State Comm. **134** 43 (2005).

[10] J. Keeling, L.S.Levitov, and P.B.Littlewood, Phys. Rev. Lett. **92** 176402 (2004).

[11] A.L. Ivanov, P.B. Littlewood, and H. Haug, Journal of Luminescence **87-89** 189 (2000).

[12] J. Fernandez-Rossier, C. Tejedor, and R. Merlin, Solid State Communnications **108** 473 (1998).

[13] A. Olaya-Castroa, L. Quirogaa, C. Tejedorc, Solid State Communnications **127** 141 (2003).

[14] S. Schmitt-Rink, D.S. Chemla, and D.A.B. Miller, Advances in Physics **38** 89 (1989).

[15] A.A. High, A.T. Hammack, L.V. Butov, M. Hanson, and A.C. Gossard, Optics Letters **32** 2466 (2007).

[16] S.A. Moskalenko, and D.W. Snoke, "Bose-Einstein Condensation of Excitons and Biexcitons", Cambridge University Press (2000).

[17] J.S. Blakemore, J. Appl. Phys. **53** R123 (1982).

[18] S. Adachi, *GaAs and Related Materials*, (World Scientific, 1994).

[19] S. Adachi, J. Appl. Phys. **58** R1 (1985).

[20] H. Mathieu, P. Lefebvre, and P. Christol, J. Appl. Phys. **72** 300 (1992).

[21] Ľ. Hrivnák, J. Appl. Phys. **72** 3218 (1992).

[22] G. F. Koster, J. O. Dimmock, R. G. Wheeler, and H. Statz, "Properties of the Thirty-two Point Groups", (MIT Press, Cambridge, Mass, 1963).

[23] T. Ostatnický, P. Gilliot, and B. Hönerlage, Journal of Applied Physics **98** 113516 (2005).

[24] H. Hillmer, A. Forchel, and C.W. Tu, J. of Phys.:Condensed Matter **5** 5563 (1993).

[25] Stephan Glutsch, "Excitons in low-dimensional semiconductors : theory, numerical methods, applications" (Springer Verlag 2004).

[26] Claus Klingshirn, *Semiconductor Optics* 3rd ed (Springer 2006).

[27] U. Rössler, S. Jorda, and B. Broido, Solid State Communications **73** 209 (1990).

[28] H.W. van Kesteren, E.C. Cosman, W.A.J.A. van der Poel, and C.T. Foxon, Phys. Rev. B **41** 5283 (1990).

[29] A.V. Efanov, K.S. Zhuravlev, T.S. Shamirzaev, W. Kellner, and H Pascher, Semicond. Sci. Technol. **19** S377 (2004).

[30] M. Combescot, O. Betbeder-Matibet, and R. Combescot, Phys. Rev. Lett. **99** 176403 (2007).

[31] A.T. Hammack, M. Griswold, L.V. Butov, L.E. Smallwood, A.L. Ivanov, and A.C. Gossard, Phys. Rev. Lett. **96** 227402 (2006).

[32] Sen Yang, A.T. Hammack, M.M. Fogler, L.V. Butov, and A.C. Gossard, Phys. Rev. Lett. **97** 187402 (2006).

[33] L. Butov, J. Phys.: Condens. Matter **16** R1577 (2004).

[34] A.V. Larionov, V.B. Timofeev, P.A. Ni, S.V. Dubonos, I. Hvam, and K. Soerensen, JETP Letters **75** 570 (2002)

[35] G.D. Gilliland, D. J. Wolford, G. A. Northrop, M. S. Petrovic, T. F. Kuech and J. A. Bradley, J. Vac. Sci. and Techn. B **10**(4), 1959 (1992).

[36] A.A. Dremin, V.B. Timofeev, A.V. Larionov, J. Hvam and K. Soerensen, JETP Lett. **76** 450 (2002).

[37] J.E. Golub, K. Kash, J.P. Harbison, and L.T. Florez, Phys. Rev. B **41** 8564 (1990).

[38] S.R. Andrews, C.M. Murray, R.A. Davies, and T.M. Kerr, Phys. Rev. B **37** 8198 (1988).

[39] J. Soubusta, R. Grill, P. Hlídek, M. Zvára, L. Smrčka, S. Malzer, W. Geißelbrecht, and G.H. Döhler, Phys. Rev. B **60** 7740 (1999).

[40] P. Harrison, "Quantum Wells, Wires and Dots - Theoretical and Computational Physics of Semiconductor Nanostructures" Second Edition, John Wiley and Sons, Chichester (2005).

[41] P. Harrison, T. Piorek, W.E. Hagston, and T. Stirner, Superlattices and Microstructures **20** 45 (1996).

[42] A. Gärtner, A.W. Holleitner, J.P. Kotthaus, and D. Schuh, Applied Physics Letters **89** 052108 (2006).

[43] A. Gärtner, L. Prechtel, D. Schuh, A.W. Holleitner, and J. P. Kotthaus, Physical Review B **76** 085304 (2007).

[44] A.T. Hammack, N.A. Gippius, S. Yang, G.O. Andreev, L.V. Butov, M. Hanson, and A. C. Gossard, J. Appl. Phys. **99** 066104 (2006).

[45] A.V. Gorbunov, and V.B. Timofeev, JETP Letters **80** 185 (2004).

[46] R. Rapaport, G. Chen, and S.H. Simon, Appl. Phys. Lett. **89** 152118 (2006).

[47] M.H. Szymańska and P.B. Littlewood, Phys. Rev. B **67** 193305 (2003).

[48] A.G. Winbow, A.T. Hammack, L.V. Butov, and A.C. Gossard, Nano Lett.**7** 1350 (2007).

[49] J. Feldmann, G. Peter, E. O. Göbel, P. Dawson, K. Moore, C. Foxon, and R. J. Elliott, Phys. Rev. Lett. **59** 2337 (1987).

[50] P.K. Basu *Theory of optical processes in semiconductors*, Chapter 12. (Clarendon Press, Oxford 1997).

[51] M. Combescot, and C. Tanguy, Europhys. Lett. **55** 390 (2001).

[52] K. Litvinenko, D. Birkedal, V. G. Lyssenko, and J. M. Hvam, Phys. Rev. B **59** 10255 (1999).

[53] S. Pilati, J. Boronat, J. Casulleras, and S. Giorgini, Phys. Rev. A **71** 023605 (2005).

[54] D.S. Fisher, P.C. Hohenberg, Phys. Rev. B **37** 4936 (1988).

[55] Yu.E. Lozovik, and O. Berman, JETP **84** 1027 (1997).

[56] D.W. Snoke, Solid State Communications, **146** 73 (2008).

[57] D.W. Snoke, and J.D. Crawford, Phys. Rev. E **52** 5796 (1995).

[58] K. El-Sayed, T. Wicht, H. Haug, and L. Bányai, Z. Phys. B. **86** 345 (1992).

[59] David W. Snoke, *Solid State Physics: Essential Concepts* (Addison Wesley, 2008).

[60] M.E. Portnoi, and I. Galbraith, Phys. Rev. B **60** 5570 (1999).

[61] N. Ben Brahim Aouani, L. Mandhour, R. Bennaceur, S. Jaziri, T. Amand, and X. Marie, Solid State Comm. **108** 199 (1998).

[62] Hui Zhao, Benedicte Dal Don, Gregor Schwartz, and Heinz Kalt, Phys. Rev. Lett. **94** 137402 (2005).

[63] Hui Zhao, Sebastian Moehl, and Heinz Kalt, Appl. Phys. Lett. **81** 2794 (2002).

[64] Hui Zhao, Sebastian Moehl, Sven Wachter, and Heinz Kalt, Appl. Phys. Lett. **80** 1391 (2002).

[65] B. Dal Don, Hui Zhao, G. Schwartz, and H. Kalt, Phys. Stat. Sol. (b) **241** 579 (2004).

[66] J. Hegarty, L. Goldner, and M.D. Sturge, Phys. Rev. B **30** 7346 (1984).

[67] J. Hegarty, and M.D. Sturge, J. Opt. Soc. Am. B **2** 1143 (1985).

[68] D. Oberhauser, K.H. Pantke, J.M. Hvam, G, Weimann and C. Klingshirn, Phys. Rev. B **47** 6827 (1993).

[69] H. Hillmer, A. Forchel, S. Hansmann, M. Morohashi, E. Lopez, H.P. Meier, and K. Ploog, Phys. Rev. B **39** 10901 (1989).

[70] W. Heller, A. Filoramo, Ph. Roussignol and U. Bockelmann, Solid-State Electronics **40** 725-728 (1996).

[71] G. Bacher, H. Schweizer, J. Kovac, H. Nickel, W. Schlapp, and R. Lösch, Appl. Phys. Lett. **61** 702 (1992).

[72] H. Sakaki, T. Noda, K. Hirakawa, M. Tanaka and T. Matsusue, Appl. Phys. Lett. **51** 1934 (1987).

[73] L.M. Smith, J.S. Preston, J.P. Wolfe, D.R. Wake, J. Klem, T. Henderson and H. Morkoć, Phys. Rev. B **39** 1862 (1989).

[74] P.K. Basu, and Partha Ray, Phys. Rev. B **44** 1844 (1991).

[75] P.K. Basu *Theory of optical processes in semiconductors – Bulk and microdtructures* Clarendon Press, Oxford (1997).

[76] P.K. Basu, Phys. Rev. B **44** 8798 (1991).

[77] P.K. Basu, Appl. Phys. Lett. **56** 1110 (1990).

[78] P.K. Basu, and Partha Ray, Phys. Rev. B **45** 1907 (1992).

[79] T. Takagahara, Phys. Rev. B **31** 6552 (1985).

[80] U. Penner, H. Rücker, and I. N. Yassievich, Semicond. Sci. Technol. **13** 709 (1998).

[81] T. Ando, A.B. Fowler, and F. Stern, Reviews of Modern Physics **54** 437 (1984).

[82] H. Hillmer, A. Forchel, R. Sauer, and C.W. Tu, Phys. Rev. B **42** 3220 (1990).

[83] H. Hillmer, A. Forchel, C.W. Tu, and R. Sauer, Semicond. Sci. Technol. **7** B235 (1992).

[84] H.N. Spector, J. Lee, and P. Melman, Phys. Rev. B **34** 2554 (1986).

[85] J. Lee, E.S. Koteles, and M. O. Vassell, Phys. Rev. B **33** 5512 (1986).

[86] A.L. Ivanov, Europhys. Lett. **59**(4) 586 (2002).

[87] D.W. Snoke, Y. Liu, Z. Vörös, L. Pfeiffer, and K. West, Solid State Communications **134** 37 (2005).

[88] L. Pfeiffer, private communication.

[89] Sen Yang, A.V. Mintsev, A.T. Hammack, L.V. Butov, and A.C. Gossard, Phys. Rev. B **75** 033311 (2007).

[90] G. Chen, R. Rapaport, L.N. Pffeifer, K. West, P.M. Platzman, S. Simon, Z. Vörös, and D. Snoke, Phys. Rev. B **74** 045309 (2006).

[91] T. Huber, A. Zrenner, W. Wegscheider, and M. Bichler, Phys. Stat. Sol. (a) **166** R5 (1998).

[92] P.C.M. Christianen, F. Piazza, J.G.S. Lok, J.C. Maan, and W. van der Vleuten, Physica B **249-251** 624 (1998).

[93] V. Negoita, D.W. Snoke, and K. Eberl, Phys. Rev. B **60**(4) 2661 (1999).

[94] V. Negoita, D.W. Snoke, and K. Eberl, Appl. Phys. Lett. **75** 2059 (1999).

[95] A.T. Hammack, M. Griswold, L.V. Butov, L.E. Smallwood, A.L. Ivanov, and A.C. Gossard, Phys. Rev. Lett. **96** 227402 (2006).

[96] X. Zhu, P.B. Littlewood, M.S. Hybertson, and T.M. Rice, Phys. Rev. Lett. **74** 1633 (1995).

[97] G.E. Bir, and G.L. Pikus, Soviet Phys. – Solid State **1** 1502 (1960).

[98] Gennadii Levikovich Bir, and Grigorii Ezekielevich Pikus, "Symmetry and Strain-Induced Effects in Semiconductors" John Wiley & Sons(New York) (1974).

[99] R. Balili, B. Nelsen, and D.W. Snoke, private communication.

[100] Peter Y. Yu, and Manual Cardona, "Fundamentals of Semiconductors" (Springer Verlag Berlin 1996).

[101] G. Rau, P.C. Klipstein, V.N. Nicopoulos, N.F. Johnson, and W.R. Tribe, Phys. Stat. Sol. (b) **198** 343 (1996).

[102] G. Platero, and M. Altarelli, Phys. Rev. B **36** 6591 (1987).

[103] D.W. Snoke, private communication.

[104] J.P. Kotthaus, Phys. Stat. Sol. (b) **243** 3754 (2006).

[105] A. Schmeller, W. Hansen, J. P. Kotthaus, G. Tänkle, and G. Weimann, Appl. Phys. Lett. **64** 330 (1994).

[106] C. Rocke, S. Zimmermann, A. Wixforth, J. P. Kotthaus, G. Böhm, and G. Weimann, Phys. Rev. Lett. **78** 4099 (1997).

[107] J. Rudolph, R. Hey, and P.V. Santos, Phys. Rev. Lett. **99** 047602 (2007).

[108] Tetsuomi Sogawa, Hideki Gotoh, Yoshiro Hirayama, Paulo V. Santos, and Klaus H. Ploog, Appl. Phys. Lett. **91** 141917 (2007).

[109] J. Szczytko, L. Kappei, F. Morier-Genoud, T. Guillet, M. T. Portella-Oberli, and B. Deveaud, Phys. Stat. Sol. (c) **1** No. 3, 493 (2004).

[110] D.W. Snoke, J.P. Wolfe, and A. Mysyrowicz, Phys. Rev. Lett. **59** 827 (1987).

[111] D.W. Snoke, D. Braun, and M. Cardona, Phys. Rev. B **44** 2991 (1991).

[112] D. Snoke, S. Denev, Y. Liu, L. Pfeiffer and K. West, Nature **418**, 754 (2002).

[113] D. Snoke, S. Denev, Y. Liu, L. Pfeiffer and K. West, Solid State Comm. **127**, 187 (2003).

[114] R. Rapaport, Gang Chen, D. Snoke, S.H. Simon, L. Pfeiffer, K. West, Y. Liu and S. Denev, Phys. Rev. Lett. **92**, 117405 (2004).

[115] L.V. Butov, A.C. Gossard, and D.S. Chemla, Nature **418** 751 (2002); L.V. Butov, L.S. Levitov, A.V. Mintsev, B.D. Simons, A.C. Gossard, and D.S. Chemla, Phys. Rev. Lett. **92** 117404 (2004).

[116] S. Yang, A.V. Mintsev, A.T. Hammack, L.V. Butov, and A.C. Gossard, Phys. Rev. B **75** 033311 (2007).

[117] L.S. Levitov, B.D. Simons, and L.V. Butov, Phys. Rev. Lett. **94** 176404 (2005).

[118] J.T. Warren, K.E. O'Hara and J.P. Wolfe, Phys. Rev. B **61** 8215 (2000).

[119] S. Denev, and D. W. Snoke, Phys. Rev. B **65** 085211 (2002).

[120] D.W. Snoke, and V. Negoita, Phys. Rev. B **61** 2904 (2000).

[121] G.L. Pollack, Reviews of Modern Physics **41** 48 (1969).

[122] D.W. Snoke, and J.P. Wolfe, Phys. Rev. B **39** 4030 (1989).

[123] Z. Vörös, R. Balili, D.W Snoke, L. Pfeiffer, and K. West, PRL **94** 226401 (2005).

[124] Z. Vörös, V. Hartwell, D.W. Snoke, L. Pfeiffer, and K. West, J. Phys.: Condensed Matter **19** 295216 (2007).

[125] A.V. Gorbunov, A.V. Larionov, and V. B. Timofeev, JETP Lett. **86** 46 (2007).

[126] A.V. Gorbunov, and V.B. Timofeev, Phys. Stat. Sol. (c) **2** 871 (2005).

[127] D.A.B. Miller, D.S. Chemla, T.C. Damen, A.C. Gossard, W. Weigmann, T.H. Wood, and C.A. Burrus, Phys. Rev. B **32** 1043 (1985).

[128] S. Zimmermann, A.O. Govorov, W. Hansen, J.P. Kotthaus, M. Bichler, and W. Wegscheider, Phys. Rev. B **56** 13414 (1997).

[129] S. Zimmermann, G. Schedelbeck, A.O. Govorov, A. Wixforth, J.P. Kotthaus, M. Bichler, W. Wegscheider, and G. Abstreiter, Appl. Phys. Lett. **73** 154 (1998).

[130] R. Rapaport, G. Chen, S. Simon, Mitrofanov, L.N. Pffeifer, ans P.M. Platzman, Phys. Rev. B **72** 075428 (2005).

[131] R. Rapaport and G. Chen, Journal of Physics: Condensed Matter **19** 295207 (2007).

[132] Z. Zhao, I.F. Silvera, and M. Reynolds, Journal of Low Temperature Physics **89** 703 (2004).

[133] G.R. Hayes, and B. Deveaud, Phys. Stat. Sol. (a) **190** 637 (2002).

[134] J. Szczytko, L. Kappei, F. Morier-Genoud, T. Guillet, M. T. Portella-Oberli, and B. Deveaud, Phys. Stat. Sol. (c) **1** 1 (2004).

[135] A. Esser, E. Runge, R. Zimmermann, and W. Langbein, Phys. Rev. B **62** 8232 (2000).

[136] P.M. Young, P.M. Hui, and H. Ehrenreich, Phys. Rev. B **44** 12969 (1991).

[137] D.M. Huang, J.-Y. Chyi and H. Morkoć, Phys. Rev. B **42** 5147 (1990).

[138] Hui Zhao, Sven Wachter, and Heinz Kalt, Phys. Rev. B **66** 085337 (2002).

[139] M.V. Marquezini, J. Tignon, T. Hasche, and D.S. Chemla, Appl. Phys. Lett. **73** 2313 (1998).

[140] S. Ben-Tabou de-Leon, B. Laikhtmann, Phys. Rev. B **63** 125306 (2001).

[141] B. Laikhtmann, Journal of Physics: Condensed Matter **19** 295214 (2007).

[142] R. Zimmermann, and Ch. Schindler, Solid State Comm. **144** 395 (2007).

[143] C. Schindler, and R. Zimmermann, arXiv:0802.3337 (2008).

[144] S. Chatterjee, C. Ell, S. Mosor, G. Khitrova, H.M. Gibbs, W. Hoyer, M. Kira, S.W. Koch, J. P. Prineas, and H. Stolz, Phys. Rev. Lett. **92** 067402 (2004).

[145] A.V. Gopal, R. Kumar, A. S. Vengurlekar, A. Bosacchi, S. Franchi, and L.N. Pfeiffer, J. Appl. Phys. **87** 1858 (2000).

[146] S. Rudin, and T.L. Reinecke, Phys. Rev. B **65** 121311(R) (2002).

[147] C. Piermarocchi, F. Tassone, V. Savona, A. Quattropani, P. Schwendimann, Phys. Rev. B **53** 15834 (1996).

[148] C. Ciuti, V. Savona, C. Piermarocchi, and A. Quattropani, Phys. Rev. B **58** 7926 (1998).

[149] G.D. Mahan, "Many-Particle Physics", Chapter 3. (Plenum, 2nd ed., 1990).

[150] L. Pitaevskii, and S. Stringari, *Bose-Einstein Condensation* Oxford University Press, USA 2003).

[151] R. Zimmermann, private communication.

[152] A.L. Ivanov, J. Phys.: Cond. Mat. **16**, S3629 (2004).

[153] Thorlabs Inc., http://www.thorlabs.com/, FB820-10, center wavelength 820 nm, bandwidth 10 nm FWHM.

[154] *Diffraction grating handbook*, 6th edition, Newport Corporation 2005

[155] L.F. Lastras-Martínez, D. Rönnow, P.V. Santos, M. Cardona, and K. Eberl, Phys. Rev. B **64** 245303 (2001).

[156] P. Etchegoin, A. Fainstein, A.A. Sirenko, B. Koopmans, B. Richards, P.V. Santos, M. Cardona, K. Totenmeyer, and K. Eberl, Phys. Rev. B **53** 13662 (1996).

[157] Kai Chang, and F. M. Peeters, Phys. Rev. B **63** 153307 (2001).

[158] M. Orlita, R. Grill, M. Zvára, G.H. Döhler, S. Malzer, M. Byszewski, and J. Soubusta, Phys. Rev. B **70** 075309 (2004).

[159] J.G. Tischler, D. Gammon, and A.S. Bracker, Phys. Stat. Sol. (b) **230** 315 (2002).

[160] A.V. Balatsky, Y.N. Joglekar, and P.B. Littlewood, Phys. Rev. Lett. **93** 266801 (2004).